

# The Nature of the Compton-thick X-ray Reprocessor in NGC 4945

Tahir Yaqoob<sup>1</sup>

<sup>1</sup>*Department of Physics and Astronomy, Johns Hopkins University, 3400 N. Charles St., Baltimore, MD 21218.*

Accepted for publication in MNRAS 18 April, 2012

## ABSTRACT

We present an exhaustive methodology for fitting Compton-thick X-ray reprocessor models to obscured active galactic nuclei (AGNs) and for interpreting the results. We focus on the MYTORUS model but also include some analysis from other models. The models are applied specifically to *Suzaku*, *BeppoSAX*, and *Swift* BAT spectra of the Seyfert 2 galaxy NGC 4945 but the basic methodology is applicable to other AGNs, including Compton-thin sources. The models overcome a major restriction of disk-reflection models, namely the assumption of an infinite column density. Finite column-density models produce a rich variety of spectral shapes and characteristics that cannot be produced by disk-reflection models, even for Compton-thin AGN with column densities in the range  $\sim 10^{23}$ – $10^{24}$  cm<sup>−2</sup>. In the Compton-thick regime we show that even though NGC 4945 is one of the brightest AGNs above 10 keV, there are significant spectral degeneracies that correspond to very different physical scenarios. The models that fit the data span nearly a factor of 3 in column density ( $\sim 2$  to  $6 \times 10^{24}$  cm<sup>−2</sup>) and two orders of magnitude in the intrinsic 2–195 keV luminosity. Models in which the continuum above 10 keV is dominated by the direct (unscattered) continuum give the highest intrinsic luminosities and column densities. Models in which the Compton-scattered continuum dominates the spectrum above 10 keV give the lowest intrinsic luminosities and column densities. Utilizing variability information from other studies of NGC 4945, namely the fact that the Fe K $\alpha$  emission line does not vary whilst the continuum above 10 keV varies significantly, we can select the solutions in which the direct continuum dominates above 10 keV. The data require that the Compton-scattered continuum and Fe K $\alpha$  line emission come predominantly from the illuminated surfaces of the X-ray reprocessor, implying a clumpy medium with a global covering factor that is small enough that the Compton-scattered continuum does not dominate the spectrum above 10 keV. The line of sight may be obscured by matter in the same distribution but a separate ring-like structure observed edge-on is not ruled out. The Fe K $\alpha$  line-emitting region must be the same one recently reported to be spatially-resolved by *Chandra*, so it must be extended on a scale of  $\sim 30$  pc or so. As found in previous studies of NGC 4945, the implied intrinsic bolometric luminosity is close to, or greater than, the Eddington luminosity. However, a scenario that is also consistent with the data and the models is that NGC 4945 is a strongly beamed AGN embedded in a shell of Compton-thick (but clumpy) matter, with a covering factor that needs less fine-tuning than the case of an isotropic intrinsic X-ray continuum. The intensity of the intrinsic X-ray continuum would be strongly aligned along or close to the line of sight, so that the true intrinsic luminosity could easily be an order of magnitude less than that deduced for an isotropic X-ray source. Beaming also appears to be consistent with recent radio and Fermi results for NGC 4945. Such beamed Compton-thick AGNs would be preferentially selected in hard X-ray surveys over unbeamed Compton-thick AGNs.

arXiv:1204.4196v2 [astro-ph.HE] 21 May 2012

**Key words:** galaxies: active - galaxies: individual (NGC 4945, 3C 273) - radiation mechanism: general - scattering - X-rays: general

## 1 INTRODUCTION

Obscured active galactic nuclei (AGNs) are of broad astrophysical interest because it is thought that a significant fraction of the power from accretion onto black holes is shrouded by a veil of circumnuclear matter (e.g., Fabian 1999), and such a population of obscured AGNs may play a significant role in contributing to the Cosmic X-ray Background (e.g., Gilli, Comastri, & Hasinger 2007, and references therein). Moreover, the connection between obscuration in AGNs and starburst activity is an area that still requires elucidation. Modeling the properties of the obscuring structure is also critical for understanding the unification of type 1 and type 2 AGN. Compton-thick obscured AGN, in which the circumnuclear matter has a Compton-scattering optical depth of  $\sim 1$  or greater (at energies of  $\sim 10$  keV) have been particularly difficult to study in the X-ray band. This is not only because of the relative weakness of the sources compared to unobscured AGNs, but also because the reprocessing of the incident X-rays in the obscuring medium affects such a large range in energy that the intrinsic, direct continuum may not be observed anywhere in the observational bandpass of a given instrument or set of instruments. The reprocessed X-ray spectrum is characterized by significant continuum curvature that peaks between  $\sim 10$ – $50$  keV, and often a strong fluorescent Fe K $\alpha$  emission line. However, the detailed shape of the X-ray spectrum depends on many factors, including the geometry and orientation of the reprocessor, and the shape of the incident continuum itself.

NGC 4945 is a nearby ( $z = 0.001878$ ) Seyfert 2 galaxy that has been known for some time to be obscured by Compton-thick matter (see Done, Madejski, and Smith 1996) and has been observed by every X-ray astronomy satellite since *Ginga*. The source is one of the brightest AGNs above  $\sim 10$  keV, yet is an order of magnitude weaker below 10 keV, a property that is characteristic of obscuration by material with a column density in the line of sight of the order of  $10^{24}$  cm $^{-2}$  but less than  $10^{25}$  cm $^{-2}$ . *BeppoSAX* was first able to obtain a broadband X-ray spectrum extending up to  $\sim 100$  keV with good sensitivity (Guainazzi et al. 2000; Dadina 2007). A recent *RXTE* study that included NGC 4945 observations spanning a period of about a decade shows a consistent 2–10 keV flux level over that period of time, which is also consistent with flux levels in this energy band before the *RXTE* observations (Rivers, Markowitz, and Rothschild 2011). However, above 10 keV, NGC 4945 is much brighter and highly variable, and it is one of the brightest AGNs in the 14–195 keV *Swift* BAT all-sky survey (e.g., see Winter et al. 2008, 2009; Tueller et al. 2009, 2010). NGC 4945 is also one of only two Seyfert 2 galaxies that is detected in the GeV band with Fermi, the other being NGC 1068 (Lenain et al. 2011).

In 2006, *Suzaku* provided the best broadband spectrum in the  $\sim 1$  –  $150$  keV band, in terms of the combination of high sensitivity above 10 keV and good spectral resolution in the critical  $\sim 6$  –  $8$  keV region that contains the Fe K $\alpha$ , Fe K $\beta$ , Ni K $\alpha$  emission lines, and the Fe K absorption edge, features which can potentially provide powerful constraints on models. Itoh et al. (2008) and Fukazawa et al. (2011) presented results of modeling the *Suzaku* data using *ad hoc* models consisting of line-of-sight extinction that does not correctly model the Compton-scattering cross section, an X-ray reflection model based on a point-source illuminating a semi-infinite slab, and discrete Gaussian components for the fluorescent emission lines that were allowed to have arbitrary fluxes. This type of model has been universally applied to the X-ray spectra of both type 1 and type 2 AGN for over 15 years. However, such a model of the Compton-thick obscuring matter is not physical and the X-ray reflection continuum model does not have a column density parameter because it is assumed to be infinite. Therefore, the matter out of the line of sight responsible for the reflection continuum (produced by Compton-scattering and absorption) cannot be related to the column density along the line of sight, and the physics relating the fluorescent line fluxes to the Compton-scattered continuum is forsaken. Moreover, the intrinsic continuum luminosity inferred from these *ad hoc* models is not straightforward to interpret, and as we shall show in the present paper, could be wrong by an order of magnitude or more. A further sacrifice that has to be made when using a disk-reflection model as a substitute for the true Compton-scattered continuum from a toroidal or spherical reprocessor is that one is forced to choose an arbitrary inclination angle for the disk. Yet, the shape of the reflection spectrum is sensitive to geometry and to the orientation of the reprocessor with respect to the observer. Different authors have adopted different values for the inclination angle, so different studies in the literature may not even be directly comparable.

More recently, Marinucci et al. (2012) have presented results from 5 new *Suzaku* monitoring observations of NGC 4945. They found that the total Fe K $\alpha$  emission-line flux varies by less than 10% whilst the continuum above 10 keV varied by a factor of  $\sim 2$ . Marinucci et al. (2012) also showed using *Chandra* data that a component of the Fe K $\alpha$  line emission is spatially resolved on a scale of at least 30 pc. These findings are important for distinguishing between various degenerate models. However, it is beyond the scope of the present paper to reanalyze the new *Suzaku* observations. Rather, our purpose is to lay out the methodology in detail using the first long *Suzaku* observation of 2006, the *BeppoSAX* observation of 1999, and the *Swift* BAT all-sky survey data. By considering a variety of possible scenarios and the associated issues involved, the methodology will help to model and interpret data from other obscured AGNs, which in general will have a lower signal-to-noise ratio than the NGC 4945 data.

In summary, the currently popular scheme for spectral-fitting analysis of Compton-thick AGN does not extract all of the physical information contained in the data, and what is extracted may not have a straightforward physical meaning (if any). Murphy and Yaqoob (2009, hereafter MY09) described and made available for general use, a toroidal model (called MYTORUS) of the Compton-thick X-ray reprocessor in AGN that addresses some of these limitations. Applying such a model entails many complexities because there may be several different types of degeneracy in the data. In the present paper we give an exhaustive account of the application of the MYTORUS model to noncontemporaneous *Suzaku*, *BeppoSAX*, and *Swift* BAT spectra of NGC 4945. We use the *BeppoSAX* data in addition to the *Suzaku* data because of the broadband coverage and good sensitivity above 10 keV of *BeppoSAX*, even though the spectral resolution is not as good as *Suzaku*. The *Swift* BAT data provide information on long-term variability of the very high-energy continuum, as well as a long-term (58-month) average of the 14–195 keV spectrum that serves as a useful baseline. We also apply the toroidal and spherical models that were made available after MYTORUS by Brightman and Nandra (2011; hereafter BN11), although these models are more restrictive than the MYTORUS model because they do not allow for time delays between the different model components. Such a generalized detailed investigation is necessary to fully interpret the NGC 4945 data, and to establish a methodology for the application and interpretation of Compton-thick X-ray reprocessor models to other AGN. NGC 4945 is an excellent candidate for a prototype Compton-thick AGN because it is so bright, the column density is not too high so that the Compton-hump is well-sampled in sensitivity by *Suzaku*, and the spectrum in the  $\sim 1$ –10 keV band is not contaminated by numerous emission lines from very hot gas as it is in NGC 1068. This means that the data in the bandpass that includes the Fe K $\alpha$  line and Fe K edge are relatively “clean” (although there is an emission line due to Fe xxv). When the modeling is applied to other AGN, such a detailed analysis will not be necessary in most cases, and our detailed description of the methodology for NGC 4945 is designed to save time by enabling the researcher to establish which procedures are not necessary for a given source and data set.

The paper is organized as follows. In §2 we describe the basic data, and reduction procedures where relevant, from *Suzaku*, *BeppoSAX*, and the *Swift* BAT. In §3 we summarize what is already known about the general form of the X-ray spectrum of NGC 4945. In §4 we describe the overall strategy of the analysis that we will present, including detailed procedures for setting up the various forms of the Compton-thick reprocessing models, and for spectral fitting. In the following three sections (§5 to §7), we give the results from fitting three classes of Compton-thick reprocessor models that correspond to very distinct physical scenarios. In §8 we bring together all the results from applying the different models and discuss the implied intrinsic luminosities and Eddington ratios of the different spectral fits, as well as the physical implications of each type of solution. In §9 we summarize our findings. In the appendix we present results of spectral fitting to some *Suzaku* 3C 273 data in order to establish some important calibration information pertinent to fitting the *Suzaku* NGC 4945 data.

## 2 OBSERVATIONS AND DATA REDUCTION

### 2.1 *Suzaku* Data

The joint Japan/US X-ray astronomy satellite, *Suzaku* (Mitsuda et al. 2007), was launched on 10 July, 2005. The present study focuses on an observation campaign on NGC 4945 that was carried out early in the life of *Suzaku*. The campaign consisted of three observations of NGC 4945 performed in 2005, August, and one in 2006, January 15. The first two observations (in 2005, August) had relatively short exposure times ( $\sim 14$  ks and 177 s), and given the historical amplitude and spectral variability of NGC 4945 (e.g. Fukazawa et al. 2011; Itoh et al. 2008, and references therein), in the present paper we only report results from the third observation, which had an exposure time of nearly 100 ks.

*Suzaku* carries four X-ray Imaging Spectrometers (XIS – Koyama et al. 2007) and a collimated Hard X-ray Detector (HXD – Takahashi et al. 2007). Each XIS consists of four CCD detectors at the focal plane of its own thin-foil X-ray telescope (XRT – Serlemitsos et al. 2007), and has a field-of-view (FOV) of  $17.8' \times 17.8'$ . One of the XIS detectors (XIS1) is back-side illuminated (BI) and the other three (XIS0, XIS2, and XIS3) are front-side illuminated (FI). The bandpass of the FI detectors is  $\sim 0.4 - 12$  keV and  $\sim 0.2 - 12$  keV for the BI detector. The useful bandpass depends on the signal-to-noise ratio of the source since the effective area is significantly diminished at the extreme ends of the operational bandpasses. Although the BI CCD has higher effective area at low energies, the background level across the entire bandpass is higher compared to the FI CCDs. Although we used the standard response matrix generator for modeling the XIS data, we measured the widths of the Mn K $\alpha$  lines from the on-board  $^{55}\text{Fe}$  calibration sources (two per XIS) using the actual NGC 4945 observations in order to independently check the spectral resolution degradation corrections in the response generator. Details are given below.

The HXD consists of two non-imaging instruments (the PIN and GSO – see Takahashi et al. 2007) with a combined bandpass of  $\sim 10 - 600$  keV. Both of the HXD instruments are background-limited, more so the GSO, which has a smaller effective area than the PIN. For AGNs, the source count rate is typically much less than the background. In order to obtain reliable background-subtracted spectra, the background spectrum must be modeled as a function of energy and time.

**Table 1.** Exposure Times and Count Rates for the Suzaku Spectra

Detector	Exposure (ks)	Energy Range (keV)	Rate <sup>a</sup> (ct/s)	Percentage of <sup>b</sup> On-Source Rate
XIS	95.1	0.7–1.83, 1.93–9.82	$0.1609 \pm 0.0007$	85.8%
PIN	80.1	11.6–47.7	$0.268 \pm 0.030$	34.7%
GSO	80.1	80–165	$0.086 \pm 0.010$	2.0%

<sup>a</sup> Background-subtracted count rate in the energy bands specified. <sup>b</sup> The background-subtracted source count rate as a percentage of the total on-source count rate, in the utilized energy intervals.

The background models for the HXD/PIN and HXD/GSO have an advertised systematic uncertainty of 1.3%<sup>1</sup> and 2%<sup>2</sup> respectively. However, the signal is background-dominated, and the source count rate may be a small fraction of the background count rate, so the net systematic error in the background-subtracted spectra could be significant. The problem is worse for the GSO than it is for the PIN. The observation of NGC 4945 was optimized for the HXD in terms of positioning the source at the aimpoint for the HXD (the so-called “HXD-nominal pointing”) which gives a somewhat lower count-rate in the XIS than the “XIS-nominal” pointing, but gives  $\sim 10\%$  higher HXD effective area.

The calibration of the relative cross-normalizations of the three instruments involves many factors, and these are discussed in detail in the appendix, where we derive the instrument cross-normalization factors from a *Suzaku* observation of 3C 273 as a guide for the analysis of the NGC 4945 data. In the appendix we also give details of the data reduction and screening procedures that we used for both the 3C 273 and NGC 4945 data, as well as details of the background subtraction and spectral responses for all instruments. The principal data selection and screening criteria for the XIS were the selection of only *ASCA* grades 0, 2, 3, 4, and 6, the removal of flickering pixels with the FTOOL `cleansis`, and exclusion of data taken during satellite passages through the South Atlantic Anomaly (SAA), as well as for time intervals less than 256 s after passages through the SAA, using the T\_SAA.HXD house-keeping parameter. Data were also rejected for Earth elevation angles (ELV) less than 5°, Earth day-time elevation angles (DYE\_ELV) less than 20°, and values of the magnetic cut-off rigidity (COR) less than 6 GeV/c<sup>2</sup>. Residual uncertainties in the XIS energy scale are on the order of 0.2% or less (or  $\sim 13$  eV at 6.4 keV – see Koyama et al. 2007). We confirmed this from an analysis of the onboard calibration line data taken during the NGC 4945 observations (see below for details).

The cleaning and data selection resulted in net exposure times that are reported in Table 1. NGC 4945 is known to have many nonnuclear X-ray sources (e.g. Schurch, Warwick, & Roberts 2002), but most cannot be resolved by the XIS. However, most of the nonnuclear sources are very soft and relatively weak. We excluded the data below 0.7 keV not only to avoid contamination from the nonnuclear sources, but also because we found that the count rate from the background below 0.7 keV is comparable to the source, giving a background-subtracted spectrum that has unacceptably large systematic errors. We did exclude two nonnuclear sources that are resolved in the XIS, by using circular masking regions, and one of these sources was a new transient discovered in the *Suzaku* data that has been discussed in detail by Isobe et al. (2008).

We extracted XIS spectra of NGC 4945 by using a circular extraction region with a radius of 3.5', excluding any masked area containing the contaminating sources. The size of the extraction region is a trade off. If it is too small, the XRT response function is less accurate and there are less source counts than a larger region would provide. A region that is too large on the other hand, has a higher background. The selected region size is a good compromise for the NGC 4945 data. Background XIS spectra were made from off-source areas of the detector, after removing a circular region with a radius of 4.5' centered on the source, the calibration sources (using rectangular masks), and the two prominent nonnuclear sources. There may still be residual contamination from unresolved nonnuclear sources above 0.7 keV and we shall bear this in mind when interpreting the spectral-fitting results. The XIS spectra from all four detectors (1–4) were combined into a single spectrum for spectral fitting. The background subtraction method for the HXD/PIN and HXD/GSO followed standard procedures, summarized in the appendix. The spectral response matrices used for each instrument are also described in the appendix. The energy bandpass used for the spectrum from each instrument was determined by the reliability of the background subtraction. Excluding lower and upper energy ranges that gave negative counts in the background-subtracted spectra result in the final energy ranges shown in Table 1. In addition, the 1.83–1.93 keV region in the XIS spectrum was excluded due to a known line-like residual calibration feature (e.g. see Yaqoob et al. 2007). The energy ranges, count rates, and the relative importance of the background in the relevant energy ranges are shown in Table 1.

Although the X-ray spectrum of NGC 4945 varies in amplitude and shape during the *Suzaku* observation, we will utilize

<sup>1</sup> <http://heasarc.gsfc.nasa.gov/docs/suzaku/analysis/pinbgd.html><sup>2</sup> <http://heasarc.gsfc.nasa.gov/docs/suzaku/analysis/gsobgd.html>

only the time-averaged spectrum over the entire observation in order to obtain the highest signal-to-noise ratio to model the nominal average spectrum. Spectral variability will be kept in mind when interpreting the results. Itoh et al. (2008) discussed in detail the nature of the variability in NGC 4945 during the *Suzaku* observation, finding that the source is variable on timescales as short as  $\sim 20$  ks.

Binning of the spectra based upon a minimum number of counts per energy bin (or a threshold signal-to-noise ratio per bin) was avoided because such a procedure distorts the spectrum, especially in regions that contain emission or absorption features. Results of spectral fitting to such spectra can be incorrect. Instead, the XIS and PIN spectra were examined, and uniform energy bin sizes were selected for energy ranges that resulted in all individual bins contained more than 20 counts. Thus, the  $\chi^2$  statistic could be used for spectral fitting. For the GSO, the special energy bin boundaries that matched the boundaries used for the available background files were adopted, and these were binned by a factor of 2, as described in the appendix.

We measured the centroid energies of the Mn  $K\alpha$  lines from the calibration sources, using spectra from the individual XIS detectors, as well as a spectrum combined from all four XIS detectors and both calibration sources. The expected energies of the Mn  $K\alpha_1$  and Mn  $K\alpha_2$  lines are 5.89875 keV and 5.88765 keV respectively (Bearden 1967). Since the  $K\alpha_1 : K\alpha_2$  branching ratio is 2:1, the expected centroid energy is then 5.89505 keV. If the spectral response functions in the XIS response matrices were perfect we should find that the calibration lines are unresolved. Using a single Gaussian with the centroid energy, intrinsic width, and overall normalization allowed to be free parameters, we found that the offset of the centroid energy (relative to the theoretical value) and the spectral resolution was different for the different XIS detectors. Since the final NGC 4945 analysis was performed using data combined from all XIS detectors, we used the calibration spectra averaged over all XIS detectors and all calibration sources to obtain a measurement of the line centroid offset and instrumental broadening at 5.9 keV. We obtained an offset for the centroid of  $+12.2^{+1.0}_{-0.9}$  eV (i.e. a best-fitting energy of 5.9073 keV), and a Gaussian width of  $\sigma = 14.1^{+3.4}_{-4.3}$  eV. The statistical errors quoted are 90% confidence for 3 interesting parameters. We will use these measurements to help model the Fe  $K\alpha$  line emission in NGC 4945. Although the energy scale and spectral resolution depend somewhat on the spatial position of the source on the XIS detectors, the data do not warrant a more sophisticated treatment.

## 2.2 BeppoSAX Data

NGC 4945 was observed by *BeppoSAX* in 1999, July 1. The *BeppoSAX* mission carried on board three imaging medium energy concentrator spectrometer units (MECS, Boella et al. 1997), and a phoswich detector system (PDS, Frontera et al. 1997). The MECS operated in the energy band  $\sim 1.7 - 10$  keV, and the PDS operated in the energy band  $\sim 15 - 220$  keV. There was also a low energy concentrator spectrometer (LECS, Parmar et al. 1997) and a high energy gas scintillation proportional counter (HPGSPC, Manzo et al. 1997) on board, but we did not utilize these in the present study. The LECS had a spectral resolution that is too low for the present study, and the HPGSPC had insufficient signal-to-noise ratio for AGN in general.

Spectra and response matrices for the MECS and PDS data were downloaded from HEASARC. The data, including background spectra, are already cleaned and prepared for spectral fitting by the pipeline processing. For the PDS, the background spectrum that was made using the so-called “Variable Rise Time” method was used<sup>3</sup>, appropriate for weak sources. At the time of the NGC 4945 observation, one of the MECS detectors was already nonoperational and the combined spectrum from MECS2 and MECS3 was utilized in the spectral fitting. The exposure times for the MECS and PDS spectra were 46.8 ks and 43.8 ks respectively. We found that the background subtraction for the MECS below 2 keV and above 9.5 keV was poor so we only utilized the energy range 2–9.5 keV. For the PDS it was found that background-subtraction systematics restricted the useful energy range of the spectrum to 16.5–100 keV. The net background-subtracted count rates in the utilized energy intervals were  $0.0478 \pm 0.0074$  ct/s and  $2.249 \pm 0.023$  ct/s respectively. The MECS and PDS spectra were binned uniformly, the bin widths being 185 eV and 2.25 keV respectively. For both spectra, each energy bin had at least 20 counts, validating the use of the  $\chi^2$  statistic for spectral fitting.

The cross-normalization of the PDS and MECS spectra was set at 0.85:1 for PDS:MECS, consistent with measurements for 3C 273 in the “BeppoSAX Cookbook”<sup>4</sup>, after correction for the “Variable Rise Time” method of background subtraction.

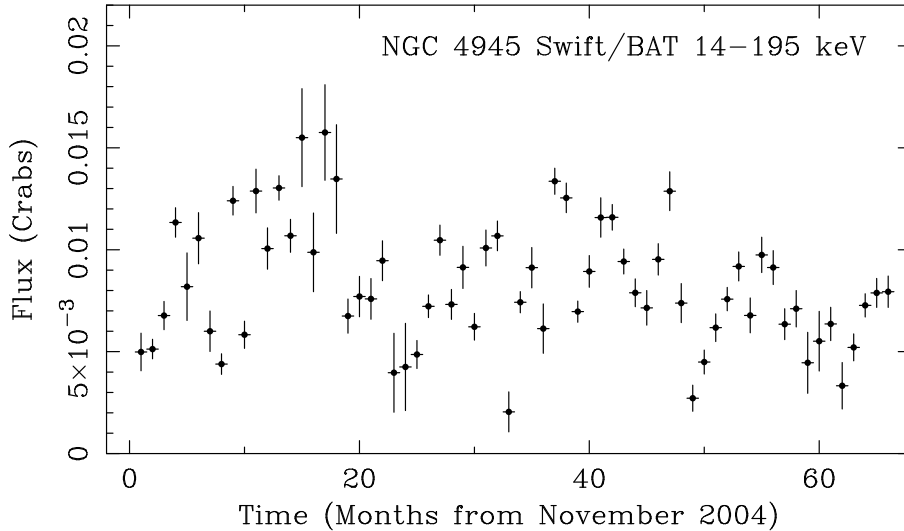
## 2.3 Swift BAT Data

The *Burst Alert telescope* (BAT, Barthelmy et al. 2005) aboard the *Swift* satellite (Geherls et al. 2004) has been conducting an all-sky hard X-ray survey in the 14–195 keV band since 2004, November (e.g. see Tueller et al. 2010; Burlon et al. 2011). NGC 4945 is one of the brightest AGN that is detected in the *Swift* BAT all-sky hard X-ray survey. The 58-month catalog lists the 14–195 keV flux of NGC 4945 as  $300.97 \times 10^{-12}$  ergs cm<sup>-2</sup> s<sup>-1</sup> <sup>5</sup>. The 58-month BAT spectrum for NGC 4945

<sup>3</sup> <http://heasarc.gsfc.nasa.gov/docs/sax/abc/saxabc/saxabc.html>

<sup>4</sup> <http://heasarc.gsfc.nasa.gov/docs/sax/abc/saxabc/saxabc.html>

<sup>5</sup> <http://swift.gsfc.nasa.gov/docs/swift/results/bs58mon/>



**Figure 1.** The NGC 4945 *Swift* BAT 66-month lightcurve in the 14–195 keV band. Each time bin corresponds to a one month time interval, the first bin corresponding to 2004, November. The flux is given in “Crab” units.

and the associated response matrix were downloaded from the archive<sup>6</sup>. The standard 8-channel spectrum from the BAT is time-averaged over a period of 58 months and was already prepared for spectral analysis. The net count rate of the spectrum is  $3.131 \pm 0.053$  ct/s. Also available as a standard product is a 66-month, 14–195 keV lightcurve that has time bins that have a duration of 1 month (since November 2004), and flux units relative to the Crab flux. This lightcurve is shown in Fig. 1 and it can be seen that the 14–195 keV flux is highly variable on timescales of months to years, showing a dynamic range of about a factor of 8 between the highest and lowest flux states. The straight average of the flux (in the Crabweighted units shown in the lightcurve) is  $8.24 \times 10^{-3}$ . The *Suzaku* spectrum corresponds to about 0.013 in these units (obtained by renormalizing the *Suzaku* spectrum to the *Swift* BAT data). This puts the *Suzaku* observation near the top of the range in Fig. 1.

### 3 GENERAL FORM OF THE X-RAY SPECTRUM OF NGC 4945

The general form of the broadband X-ray spectrum of NGC 4945 is now well established (e.g. Itoh et al. 2008 and references therein). The spectrum below  $\sim 10$  keV is heavily suppressed relative to that in the  $\sim 10$ –30 keV band, due to heavy obscuration. Below  $\sim 10$  keV the spectrum is dominated by scattered emission of the intrinsic X-ray continuum in an extended optically-thin medium (e.g., Turner et al. 1997; Marinucci et al. 2012, and references therein). Below  $\sim 1$  keV there is evidence of an additional soft excess that is due to thermal emission from extended circumnuclear matter (at least some of this has been directly spatially resolved by *Chandra*, as described by Marinucci et al. 2012). Such a spectrum is typical of obscured AGN, although the amount of suppression below 10 keV (compared to the flux above 10 keV) varies from source to source. The intrinsic X-ray continuum in NGC 4945 has to be inferred indirectly (and therefore is model-dependent) because of the complexity and breadth of the various X-ray spectral features. In our analysis we will adopt two forms for the intrinsic continuum, the first being a simple power law (with a photon index of  $\Gamma$ ), and a termination energy,  $E_T$ . The second continuum form is that of a Comptonized Wien spectrum, characterized by the temperature and optical depth of the Comptonizing plasma ( $kT$  and  $\tau$  respectively). The exact form of the initial spectrum (in this case a Wien spectrum) is unimportant for values of the Compton- $y$  parameter that result in a Comptonized spectrum that is roughly a power law with a high-energy rollover (i.e. observationally relevant to NGC 4945). This model of the intrinsic continuum is described in Titarchuk (1994), in which it is explained that the Wien spectrum was adopted because it lends itself to certain computational advantages. In XSPEC the model is known as COMPTT. The temperature of the Wien spectrum was fixed at 0.01 keV, below the lower end of the bandpass for any of the data sets that we used, and this choice does not affect the values  $kT$  and  $\tau$  used to fit the data. Again, this is because for a Compton- $y$  parameter greater than unity, the Comptonized spectrum is not sensitive to the exact form of the initial spectrum.

A fraction of the direct continuum is scattered into the line of sight by optically-thin matter, extended on the same or larger size scale as the putative torus, and we refer to this fraction as  $f_s$ . In the optically-thin limit, the Thomson depth,  $\tau_{\text{es}}$ , of the scattering region is simply equal to  $f_s$  for a fully covering spherical distribution of material. More realistically,

<sup>6</sup> [http://swift.gsfc.nasa.gov/docs/swift/results/bs58mon/SWIFT\\_J1305.4-4928](http://swift.gsfc.nasa.gov/docs/swift/results/bs58mon/SWIFT_J1305.4-4928)

$f_s = [\Omega/4\pi]\tau_{\text{es}}$ , where  $[\Omega/4\pi]$  is the solid angle as a fraction of  $4\pi$  subtended by the scattering zone at the X-ray source. Only that part of the scattering zone visible to the observer should be included in this solid angle. We assume that the optically-thin scattered continuum has an identical spectral shape to the intrinsic continuum, although the former is allowed to have its own uniform, Compton-thin absorption (column density  $N_{\text{H1}}$ ). Part, or all of this column density may be due to absorption in the host galaxy. In reality the above two assumptions are oversimplistic, but given the complexity of the overall baseline model, a more detailed treatment of the optically-thin scattered continuum is not warranted. We add to these continuum components an optically-thin thermal continuum emission component using the APEC model with abundances fixed at the solar values, but with the normalization and temperature of the thermal component ( $kT_{\text{apec}}$  and  $A_{\text{apec}}$  respectively) allowed to float in fits. This optically-thin emission component is of course *not* absorbed by the large, Compton-thick column density (or at least, we observe only the portion that is unobscured by it). However, we do include a lower, uniform column density as a free parameter to allow for the possibility of absorption by material in addition to the primary X-ray reprocessing structure (we will refer to it as  $N_{\text{H2}}$ ). The column densities  $N_{\text{H1}}$  and  $N_{\text{H2}}$  are *not* tied together (even though they cover a similar physical region) as this allows for the most general situation. Preliminary spectral fitting showed that both  $N_{\text{H1}}$  and  $N_{\text{H2}}$  are less than  $\sim 10^{22} \text{ cm}^{-2}$  (i.e., Compton-thin) and in fact similar in value to each other. Since these column densities are so small (Thomson depth  $\ll 0.01$ ) it is not necessary to model Compton scattering or fluorescent line emission from these absorption components.

In §4 we describe in detail how the Compton-thick absorption, scattering and fluorescent Fe K $\alpha$  and Fe K $\alpha$  line emission in NGC 4945 are modeled. The Ni K $\alpha$  line emission is weak in the NGC 4945 data and is not yet included in the MYTORUS model but it is included in some of the other Compton-thick reprocessor models that we used. In the former case, the Ni K $\alpha$  is modeled as a separate unresolved Gaussian component (characterized by a centroid energy and line flux denoted by  $E_{\text{NiK}\alpha}$  and  $I_{\text{NiK}\alpha}$  respectively). The *Suzaku* data also show line emission centered around 6.7 keV, which we ascribe to Fe XXV, and this is also modeled by a separate Gaussian component. It very likely originates in the ionized extended zone and does not originate in the Compton-thick X-ray reprocessor which produces the Fe K $\alpha$  line centered at 6.4 keV in neutral matter. The centroid energy, intrinsic Gaussian width, and flux of the line centered at  $\sim 6.7$  keV are denoted by  $E_{\text{FeXXV}}$ ,  $\sigma_{\text{FeXXV}}$ , and  $I_{\text{FeXXV}}$  respectively. We note that individual lines of the Fe XXV triplet cannot be resolved by *Suzaku* and the emission that is observed may even have some contribution from lower ionization states so the line width should not be interpreted as necessarily due entirely to velocity broadening.

All spectral fits to the *BeppoSAX* data will have fewer free model parameters than the models fitted to the *Suzaku* data because the *BeppoSAX* MECS spectrum only extends down to 2 keV. Our approach is to freeze the normalization and temperature of the soft X-ray, optically-thin, thermal continuum at values obtained from the *Suzaku* fits. The same is done for the column density associated with the optically-thin thermal emission ( $N_{\text{H2}}$ ). In addition, since the spectral resolution of the MECS is greater than 600 eV at the energies of the Gaussian emission-line components (i.e., in the 6–8 keV range), the centroid energies of the lines were fixed at 6.700 keV and 7.472 keV, corresponding to the theoretical energies of the Fe xxv(r) and Ni K $\alpha$  lines respectively. Moreover, the intrinsic width of the Fe xxv(r) line was fixed at a best-fitting value obtained from the *Suzaku* data, and the intrinsic widths of the Fe K $\alpha$  and Ni K $\alpha$  lines were fixed at 100 km s $^{-1}$  FWHM because these lines in the *Suzaku* data were unresolved. Whereas the *Suzaku* fits have two relative normalization parameters (which we refer to as  $C_{\text{PIN:XIS}}$  and  $C_{\text{GSO:XIS}}$ ), the *BeppoSAX* data only have one (which we refer to as  $C_{\text{PDS:MECS}}$ ). The value of  $C_{\text{PIN:XIS}}$  was fixed at 1.12 (see appendix),  $C_{\text{GSO:XIS}}$  was allowed to float unless stated otherwise, and  $C_{\text{PDS:MECS}}$  was fixed at 0.85 (see §2.2).

Models for the *Swift* BAT data of course always have fewer model components than those for the *Suzaku* and *BeppoSAX* data because the soft X-ray emission component, the optically-thin scattered continuum, the associated column densities, and the fluorescent emission lines can be omitted.

## 4 ANALYSIS STRATEGY

There are a number of critical steps in the analysis scheme that we will pursue, and in this section we outline the key motivators and drivers at each stage of the complex analysis. These steps in the analysis will be described in more detail in later sections when necessary.

### 4.1 Constraints from Variability

The large-amplitude, short and long-timescale continuum variability above 10 keV, as demonstrated by the *Swift* BAT (Fig. 1) and other data (Itoh et al. 2008; Marinucci et al. 2012, and references therein), imposes a constraint on the size of the Compton-thick region responsible for producing the narrow Fe K $\alpha$  emission and the associated Compton-scattered continuum. Since the flux of the Fe K $\alpha$  line in NGC 4945 does not respond to the variable continuum above 10 keV, it is a robust inference that the continuum above 10 keV cannot be dominated by the Compton-scattered component of the continuum since that

latter component has to originate in the same region as the Fe K $\alpha$  line. Therefore, the continuum above 10 keV must be dominated by the direct (unscattered) continuum transmitted through the Compton-thick medium in the line of sight (we refer to this component in general as the zeroth-order continuum). However, since we will be describing a methodology that should be applicable to AGNs in general, we will also consider cases in which the high-energy continuum above 10 keV is dominated instead by the Compton-scattered continuum. For example, as we shall see, an AGN shrouded in a fully-covering Compton-thick spherical distribution of matter will have a high-energy continuum that is dominated by the Compton-scattered continuum (this is reversed if the source is Compton-thin). For most AGNs there may not be sufficient data (in quantity and/or quality) to determine the variability properties of the high-energy continuum and Fe K $\alpha$  line, so both cases (zeroth-order continuum dominating and not dominating above 10 keV) would need to be considered if they may provide degenerate spectral solutions. However, we note that if an AGN is Compton-thin in the line of sight, with a column density in the range  $\sim 10^{23}$  to  $10^{24}$  cm $^{-2}$ , there will be much less ambiguity because the zeroth-order continuum will impose strong and characteristic features on the spectrum in terms of the detailed shape of the Fe K edge and the continuum below it. The EW of the Fe K $\alpha$  line with respect to the total continuum then narrows down the parameter space even further. Even spectra of weak AGNs in this regime of intermediate Compton depth may yield less ambiguity in the model solutions than much brighter AGNs that are Compton thick. (Sources with column densities less than  $\sim 10^{23}$  cm $^{-2}$  are of course far less complex, since they are dominated by the zeroth-order continuum at all energies.)

#### 4.1.1 Separability of the Zeroth-Order Continuum and the Compton-scattered Continuum

In our analysis we will explore and derive results for several scenarios, including those that are ruled out by the variability properties of NGC 4945. The purpose here is to illustrate how the different scenarios can give degenerate spectral solutions even for the high signal-to-noise ratio of the NGC 4945 data. For weaker AGNs, and those that lack vital variability information, being aware of the spectral degeneracies and correctly interpreting them will be important. We point out that in order to adequately model NGC 4945, and any other source for which time variability of the Compton-thick scattered continuum needs to be considered, ideally we need a Compton-thick reprocessor model in which the zeroth-order continuum and the Compton-scattered continuum are separable (i.e. they must be allowed to have independent normalizations for the purpose of spectral fitting). In the Compton-thick spectral-fitting models of BN11 the two continuum components are not separable. The only model that is currently publicly available that has the required capabilities to handle the possibility of different timescales of variability of the Compton-scattered and zeroth-order continuum components is the MYTORUS model (see MY09). Nevertheless, we will still make use of the BN11 models.

## 4.2 Constraints from the Intrinsic Fe K $\alpha$ Line Width

In principle, we can estimate the light-crossing time across any spatially unresolved X-ray reprocessor that might be present, using measurements of the Fe K $\alpha$  intrinsic line width. If the FWHM velocity of the line is  $V_{\text{FWHM}}$ , using a virial estimate of the velocity dispersion of  $\sqrt{3}V_{\text{FWHM}}/2$  (following Netzer 1990), and a simple Keplerian assumption, gives a light-travel time from the X-ray source to the reprocessor of  $t = (r/c) \sim 67M_6[3/V_{1000}]^2$  ks, where  $V_{1000}$  is the measured FWHM in units of 1000 km s $^{-1}$ , and  $M_6$  is the central black-hole mass in units of  $10^6 M_\odot$ . The *Chandra* high-energy grating (HEG) measured an intrinsic width of the narrow Fe K $\alpha$  line in NGC 4945 of  $\sim 2780$  km s $^{-1}$  FWHM, with a two-parameter, 99% confidence range of  $\sim 1700$  to  $\sim 5200$  km s $^{-1}$  FWHM (Shu, Yaqoob, & Wang 2011). The HEG has the best spectral resolution in the Fe K band currently available. Using  $M_6 = 1.4$  (Greenhill et al. 1997), we see that for a nominal value of  $V_{1000}$  of 3, the light-crossing timescale is  $\sim 100$  ks, and for a value of 5 (around the upper limit for  $V_{1000}$ ), the timescale is  $\sim 33$  ks. The fastest timescale for high-energy continuum variability in NGC 4945 reported so far is  $\sim 20$  ks for a flux doubling (Itoh et al. 2008). However, it is likely that the line broadening is due to the component of the Fe K $\alpha$  line that is spatially extended, because grating spectrometers cannot distinguish between spatial and true spectral broadening. Nevertheless, we refer to the calculation of velocity broadening for the sake of application to AGNs other than NGC 4945, for which the line emission is spatially unresolved. We note in passing that the HEG centroid energy of the Fe K $\alpha$  line in NGC 4945 is extremely well constrained ( $6.389^{+0.007}_{-0.008}$  keV), confirming its origin in neutral Fe or nearly neutral Fe.

We should also bear in mind that the case of NGC 4945 does not rule out the possibility of two physically distinct regions of Compton-thick matter. Although the Fe K $\alpha$  line emission that is spatially resolved and extended, on a scale of 30 pc or greater, could account for the bulk of the total Fe K $\alpha$  line emission (Marinucci et al. 2012), it is possible that there could be a smaller Compton-thick region that obscures the line of sight but has a sufficiently small covering factor that it does not make a significant contribution to the Fe K $\alpha$  line.



### 4.3 Intrinsic Luminosities

It is important to understand that, in addition to finding solutions that fit the various X-ray spectra of NGC 4945 (and other AGNs), we must keep a check on the implied intrinsic continuum luminosities because they can differ by an order of magnitude or more for different degenerate scenarios. In fact, we shall see that it is possible for different spectrally degenerate models applied to two observations of a source to predict opposite senses of variability under some circumstances. In other words, one set of models may imply a decreasing intrinsic luminosity going from one observation to the next, whilst a different set of models may imply an increasing intrinsic luminosity going from one observation to the next. Here we simply point out a general characteristic of the various models, namely that the higher the contribution of the zeroth-order continuum relative to the Compton-scattered continuum, the greater the intrinsic luminosity is. This is because Compton scattering shifts more of the intrinsic continuum into the observer's line of sight compared to the case when the observer receives only the zeroth-order continuum. In other words, if there is a Compton-scattered continuum component observed in the spectrum, it can only *decrease* the burden on the intrinsic continuum to produce the observed luminosity for a given column density. To put it another way, the intrinsic continuum must lie above the zeroth-order continuum by a very specific amount that depends only on the line-of-sight column density, *regardless of geometry and regardless of the level of the Compton-scattered continuum*. There are two particular corollaries of this. One is that if the observed spectrum can be well-fitted by *only* the zeroth-order continuum (e.g., if the reprocessor has a negligible global covering factor), such a fit yields the maximum possible intrinsic continuum luminosity for a given line-of-sight column density. The second corollary is that for a given line-of-sight column density, a distribution of matter with full covering (such as a spherically-symmetric distribution) will give the *minimum* possible intrinsic luminosity. In the Compton-thin limit, these minimum and maximum luminosities will of course be equal to each other because in that limit there is only the zeroth-order continuum regardless of covering factor. As the Compton depth of the matter distribution approaches unity ( $N_H \sim 1.2 \times 10^{24} \text{ cm}^{-2}$ ), the Compton-scattered continuum from a fully-covered source dominates over the zeroth-order continuum in the observed spectrum. As we will see, the two extremes give implied intrinsic luminosities that can differ by an order of magnitude or more. In all of the tables in which we will give the results of spectral fitting, we will give observed fluxes and luminosities in various energy bands. However, the intrinsic luminosities and their ratios with respect to the Eddington luminosity will not be discussed until all of the spectral fitting results have been presented. Discussion of the intrinsic luminosities and their implications will be presented in §8.

### 4.4 Procedure for NGC 4945

Our analysis procedure for NGC 4945 is then as follows.

We begin with the simplest and extreme scenario, namely that in which the spectrum of NGC 4945 above 10 keV consists *only* of the zeroth-order continuum.

- (i) We examine all of the three data sets above 10 keV only (i.e. utilizing only HXD data for *Suzaku*, only PDS data for *BeppoSAX*, and the *Swift* BAT data). The model above 10 keV is very simple because no emission lines or soft X-ray emission components need to be included.
- (ii) These spectral fits are described in §5, and we will find that, in addition to a simple power law, we need to consider intrinsic spectra that rollover in the instrument bandpasses. For this we use a thermally Comptonized intrinsic continuum (details in §3).

Obviously, the Compton-scattered continuum cannot be zero since there has to be a specific flux of this continuum that is associated with the fluorescent Fe K $\alpha$  and Fe K $\beta$  emission lines. However, these extremal fits will be useful for four reasons:

- (i) One is that the fits can guide spectral fitting with more complex models across the full instrumental bandpasses.
- (ii) Another reason is that our results can be used to assess the limitations of deriving key physical parameters (such as column density and intrinsic luminosity) when a particular source *only* has *Swift* BAT data available. Even though the *Suzaku* and *BeppoSAX* observations are not contemporaneous with the *Swift* BAT data, the latter contain information about long-term variability spanning a period of over 5 years, and about the average spectrum over a similarly long time period.
- (iii) A third reason is that the zeroth-order continuum fits will provide an indicator of the maximum possible intrinsic continuum luminosities.
- (iv) A fourth reason is that this is the *only* model in which an arbitrary intrinsic continuum can be used, with any of the intrinsic continuum parameters allowed to be free (without having to generate grids of tables at finite parameter-value intervals).

We then proceed to obtain full solutions for the *Suzaku* data and *BeppoSAX* data, including the Fe K $\alpha$  emission line and other model components in the fits.

- (i) Spectral fitting is then divided into two classes of models, one in which the Compton-thick reprocessor has the zeroth-order

and Compton-scattered continuum components “coupled” to each other, and one in which they are “decoupled.”

- (ii) Only the MYTORUS model allows decoupling, and when used in this mode, one interpretation is that the model mimics a patchy (or clumpy) X-ray reprocessor in which the “holes” allow unobscured observation of some of the reflection and fluorescence from the far-side, inner surface of the structure. In this mode, the geometry is not necessarily strictly toroidal, and the global covering factor is unspecified because the spectrum is dominated by matter observed through the “holes” and by matter in the line of sight. Another scenario is that a subset of the decoupled models describes two distinct X-ray reprocessing regions, one that obscures the central X-ray source with less than full global covering, and another more extended reflection region, such as that which has been spatially resolved in NGC 4945 (Marinucci et al. 2012).
- (iii) The decoupled mode of the MYTORUS model is in fact closest to the procedure that has been universally used in the literature for AGNs in general for over 15 years: a disk-reflection continuum modeled with PEXRAV or PEXMON (or equivalent), combined with decoupled line-of-sight extinction modeled with CABS or just ZPHABS (absorption only). However, disk-reflection models assume an infinite column density for the material responsible for producing the Compton-scattered continuum so they cannot produce spectral features in the data that are characteristic of scattering in a finite column-density medium. Combined with the fact that the geometry of disk-reflection models may be inappropriate, the MYTORUS model, even in the decoupled mode, yields column densities and intrinsic continuum luminosities that have more straightforward physical interpretations. Also, the line-of-sight extinction in the MYTORUS model employs a fully relativistic Compton-scattering cross section.
- (iv) The detailed setup and parameters of the coupled and decoupled modes of the MYTORUS model are given in §4.5. The results of fitting the coupled MYTORUS model are given in §6, and those obtained from fitting the decoupled MYTORUS model are given in §7. A particular feature of the decoupled model is that it allows a Compton-thick structure observed edge-on to produce a large fluorescent Fe K $\alpha$  line EW whilst still allowing the zeroth-order continuum to dominate above 10 keV.
- (v) We will also utilize the toroidal and fully-covering spherical models of BN11. Since the zeroth-order and Compton-scattered continua cannot be decoupled in these models, their application is described along with the other coupled models in §6.

#### 4.5 The MYTORUS Model

The toroidal Compton-thick X-ray reprocessor model, MYTORUS, has been described in detail in MY09, and Yaqoob & Murphy (2011a). The geometry consists of a torus with a circular cross section, whose diameter is characterized by the equatorial column density,  $N_H$ . The model is currently restricted to a configuration in which the global covering factor of the reprocessor is 0.5, corresponding to a solid angle subtended by the structure at the central X-ray source of  $2\pi$ . However, spectral fits with the zeroth-order continuum only (see §5) correspond to the limit of a negligible covering factor, and fits with the BN11 fully-covering spherical model (see §6) correspond to the other extremal limit in the covering factor. We will also utilize the toroidal model of BN11, which does allow the covering factor to vary between 0.1 and 0.9, but, like the BN11 spherical model, this model does not allow separation of the zeroth-order and Compton-scattered continua.

The practical implementation of the MYTORUS model allows free relative normalizations between different components of the model in order to accommodate differences in the actual geometry (compared to the specific model assumptions used in the original calculations), and time delays between direct, scattered, and fluorescent line photons<sup>7</sup>. The zeroth-order component of the model is essentially an energy-dependent multiplicative factor that is independent of the geometry and independent of the intrinsic continuum. The multiplicative factor is then implemented with a single XSPEC table for all applications of the model (it is `mytorus_Ezero_v00.fits`). The Compton-scattered continuum is implemented as an XSPEC additive table model, utilizing different tables for a power-law input continuum and a Comptonized thermal (COMPTT) input continuum (see Titarchuk 1994). For the former, tables with a termination energy of 200 keV were used, and for the latter, each table has a unique, fixed value of the Comptonizing plasma temperature. Tables with different temperatures were utilized, and details will be given in the appropriate places in the descriptions of the data analysis procedures. The Fe K $\alpha$  and Fe K $\beta$  line emission is implemented with another XSPEC additive table model that is selected from line tables made with a range of energy offsets for best-fitting the peak energies of the emission lines. Preliminary fitting showed that an offset of +20 eV is optimal for the NGC 4945 *Suzaku* data (this offset covers both instrumental energy offsets, as well as any intrinsic offset due to very mild ionization). Different sets of emission-line tables are used for the power-law and Comptonized thermal intrinsic continua (i.e. each Compton-scattered continuum table has a corresponding emission-line table for a given offset energy). Again, details of the actual tables used will be given at the appropriate places in the data analysis descriptions. The Fe K $\alpha$  and Fe K $\beta$  lines are broadened by two Gaussian convolution model components (GSMOOTH in XSPEC). One of these accounts for the residual instrumental broadening that is not in the response matrix, and is normalized to the broadening of the calibration source data (see §2.1), with a  $\sqrt{E}$  dependence of the Gaussian width, and the other is the actual velocity broadening (Gaussian width proportional to line energy).

<sup>7</sup> See <http://mytorus.com/manual/> for details

#### 4.5.1 Default (Coupled) Model

In this mode of use (regardless of the form of the intrinsic continuum), the angle made by the axis of the torus with the observer’s line of sight ( $\theta_{\text{obs}}$ ) is coupled to the column density that is intercepted by the zeroth-order continuum. In other words, the effective geometry of the X-ray reprocessor is *precisely* that assumed in the original Monte Carlo calculations (MY09). We denote the relative normalization between the scattered continuum and the direct, or zeroth-order continuum, by  $A_S$ , which has a value of 1.0 for the assumed geometry with the assumption that either the intrinsic X-ray continuum flux is constant, or, for a variable intrinsic X-ray continuum, that the X-ray reprocessor is compact enough for the Compton-scattered flux to respond to the intrinsic continuum on timescales much less than the integration time for the spectrum. It is important to note that  $A_S$  is *not* simply related to the covering factor of the X-ray reprocessor because the detailed shape of the Compton-scattered continuum varies with covering factor. Analogously to  $A_S$ , the parameter  $A_L$  is the relative normalization of the Fe K $\alpha$  line emission, with a value of 1.0 having a similar meaning to that for  $A_S = 1.0$ . In our analysis we will set  $A_L = A_S$  unless otherwise stated.

For the sake of reproducibility, we give below the exact model expression that we used in XSPEC (for the case of an intrinsic power-law continuum). The numbered model components and model parameters are described in Table 2. This example is for a power-law intrinsic continuum with a termination energy,  $E_T$ , of 200 keV, and an offset of +20 eV for the emission-line tables. Substitution of the scattered continuum and emission-line tables with corresponding tables for a different intrinsic continuum is straightforward (for example, see §4.5.2). In the case of the COMPTT model substituting for the power-law continuum, the photon index,  $\Gamma$ , is replaced by the Comptonizing plasma optical depth ( $\tau$ ) for a given table selected for the Comptonizing plasma temperature,  $kT$  (and the normalization,  $A_{\text{PL}}$ , replaced by  $A_{\text{comptt}}$ ). The parameters  $C_{\text{PIN:XIS}}$ ,  $C_{\text{GSO:XIS}}$ , and  $C_{\text{PDS:MECS}}$  are instrumental cross-normalizations (clearly, one or more of these will be absent in the model if data from the corresponding instruments are not utilized). The value of  $C_{\text{PIN:XIS}}$  was fixed at 1.12 (see appendix),  $C_{\text{GSO:XIS}}$  was allowed to float unless stated otherwise, and  $C_{\text{PDS:MECS}}$  was fixed at 0.85 (see §2.2). Hereafter, Compton-scattered continuum components in the MYTORUS model will be referred to generically by the label MYTS and any energy-dependent multiplicative factor that is used to obtain the zeroth-order continuum will be referred to generically by the label MYTZ.

$$\begin{aligned} \text{model} = & \text{constant} < 1 > * \text{phabs} < 2 > ( \\ & \text{zpowerlw} < 3 > * \text{etable}\{\text{mytorus\_Ezero\_v00.fits}\} < 4 > + \\ & \text{constant} < 5 > * \text{atable}\{\text{mytorus\_scatteredH200\_v00.fits}\} < 6 > + \\ & \text{constant} < 7 > * \text{gsmooth} < 8 > (\text{gsmooth} < 9 > (\text{atable}\{\text{myt1\_V000010pEp020H200\_v00.fits}\} < 10 >)) + \\ & \text{zgauss} < 11 > + \text{zgauss} < 12 >) + \\ & \text{constant} < 13 > * \text{zphabs} < 14 > * \text{zpowerlw} < 15 > + \text{zphabs} < 16 > * \text{apec} < 17 >) \end{aligned}$$

#### 4.5.2 Decoupled Model

A problem with all Monte-Carlo simulations of the Compton-scattered continuum from a toroidal structure observed edge-on is that the spectrum is extremely sensitive to the geometry of the “edges” of the structure. This is because the column density presented to incident continuum photons is small at the edges, and the Compton-scattered flux from these regions can easily dominate the entire spectrum if the equatorial part of the reprocessor is Compton-thick. This is not just a problem with the MYTORUS model but it is a general problem with similar models observed edge-on (e.g., the toroidal models of Ghisellini, Haardt, & Matt 1994, Ikeda, Awaki, & Terashima 2009, and BN11). In reality, the geometry of the toroidal structure, particularly at the edges, may not be well represented by the exact model geometry that is used. For example, a structure that is cylindrical should produce an edge-on Compton-scattered spectrum that is much weaker than that produced by the particular toroidal geometry of the MYTORUS model. Another problem is that the finite size of the inclination-angle bins means that even when the inclination angle is  $90^\circ$  in the model, there is always some “leakage” contribution from photons with angles less than  $90^\circ$ . We can mitigate these problems in the MYTORUS model by decoupling the zeroth-order continuum from the inclination angle ( $\theta_{\text{obs}}$ ), fixing this angle at  $90^\circ$ , and allowing the relative normalization of the Compton-scattered continuum to be free, and much less than 1.0 if necessary. In this context, we refer to the relative normalization as  $A_{S90}$  (it was just  $A_S$  in the coupled model). Since the zeroth-order continuum is independent of geometry (being purely a line-of-sight quantity), the inclination angle associated with this component becomes a dummy parameter and it is fixed at  $90^\circ$  so that the zeroth-order column density is literally equal to the value of  $N_H$  for this model component. (In the coupled mode, the equatorial  $N_H$  is not equal to the line-of-sight column density for general values of  $\theta_{\text{obs}}$ .) The column density associated with the zeroth-order continuum and the Compton-scattered continuum remain coupled to a single value in our implementation for NGC 4945, although they could be decoupled if we wanted to mimic a more complex structure for the reprocessor.

Yet another issue with a Compton-thick structure observed edge-on is that the zeroth-order and Compton-scattered

**Table 2.** Parameters for the Baseline Coupled MYTORUS Model with a Power-law Intrinsic Continuum

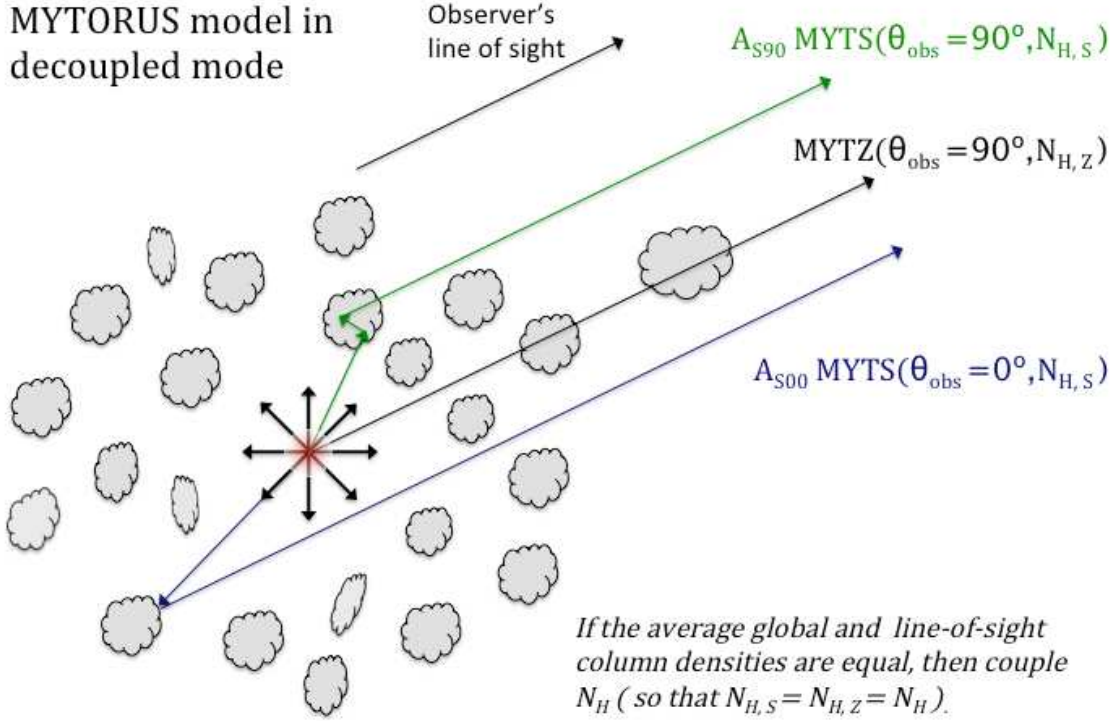
Par. <sup>a</sup>	Comp. <sup>b</sup>	Symbol	Units	Status	Description
1	1	$C_{\text{PIN:XIS}}, C_{\text{PDS:MECS}}$	...	fixed	PIN:XIS or PDS:MECS instrumental cross-normalization ratio.
2	1	$C_{\text{GSO:XIS}}$	...	free	GSO:XIS instrumental cross-normalization ratio.
3	2	$N_{\text{H,Gal}}$	$10^{21} \text{ cm}^{-2}$	fixed (1.57)	Galactic column density.
4	3,6,10,15	$A_{\text{PL}}$	$\text{ph. cm}^2 \text{ s}^{-1} \text{ keV}^{-1}$	free	Intrinsic power-law normalization at 1 keV.
5	3,6,10,15	$\Gamma$		free	Photon index of the power-law continuum.
6	4,6,10	$N_{\text{H}}$	$10^{24} \text{ cm}^{-2}$	free	Equatorial column density of the torus.
7	4,6,10	$\theta_{\text{obs}}$	degrees	free	Inclination angle of the torus.
8	5	$A_{\text{S}}$	...	free	Scaling factor for the scattered continuum from the torus.
9	7	$A_{\text{L}}$	...	$= A_{\text{S}}$	Scaling factor for the fluorescent line emission from the torus.
10	8	$\sigma_{\text{det}}$	eV	fixed <sup>c</sup> (14)	Line width accounting for XIS resolution degradation.
11	9	$\text{FWHM}[\text{Fe K}\alpha, \text{Fe K}\beta]$	$\text{km s}^{-1}$	fixed <sup>d</sup> (100)	Intrinsic width of the Fe K $\alpha$ and Fe K $\beta$ emission lines.
12	11	$E_{\text{Fe XXV}}$	keV	free <sup>d</sup>	Gaussian centroid energy of the line emission at $\sim 6.7$ keV.
13	11	$\text{FWHM}[\text{Fe XXV}]$	$\text{km s}^{-1}$	free <sup>d</sup>	Intrinsic width of the line emission at $\sim 6.7$ keV.
14	11	$I_{\text{Fe XXV}}$	$\text{ph. cm}^2 \text{ s}^{-1}$	free	Flux of line emission at $\sim 6.7$ keV.
15	12	$E_{\text{Ni K}\alpha}$	keV	free <sup>d</sup>	Gaussian centroid energy of the Ni K $\alpha$ line.
16	10	$\text{FWHM}[\text{Ni K}\alpha]$	$\text{km s}^{-1}$	fixed <sup>d</sup> (100)	Intrinsic width of the Ni K $\alpha$ line.
17	12	$I_{\text{Ni K}\alpha}$	$\text{ph. cm}^2 \text{ s}^{-1}$	free	Flux of the Ni K $\alpha$ line emission.
18	13	$f_{\text{s}}$	...	free	Scattering fraction due to optically-thin matter.
19	14	$N_{\text{H1}}$	$10^{21} \text{ cm}^{-2}$	free	Absorber covering optically-thin scattering zone.
20	16	$N_{\text{H2}}$	$10^{21} \text{ cm}^{-2}$	free	Absorber covering extended thermal emission zone.
21	17	$A_{\text{apec}}$	$\text{ph. cm}^2 \text{ s}^{-1} \text{ keV}^{-1}$	free	Normalization of the APEC model.
22	17	$kT_{\text{apec}}$	keV	free	Temperature of the APEC model.

<sup>a</sup> Parameter number. <sup>b</sup> Model component(s) that the parameter appears in (corresponding to the model component numbers in the model expression shown in §4.5.1). <sup>c</sup> Determined from fitting calibration source data (see §2.1). <sup>d</sup> The Gaussian emission-line centroid energies, and the intrinsic width of the Fe XXV line were initially allowed to float but they were then frozen at their best-fitting values in order to obtain robust statistical errors on the other parameters of interest. A single intrinsic width is associated with the Fe K $\alpha$  and Fe K $\beta$  lines, and this width, along with that of the Ni K $\alpha$  line was fixed at 100  $\text{km s}^{-1}$  FWHM since the lines were found to be unresolved. Upper limits were derived by allowing the two line widths to float in turn (see §6 and §7).

continua could be so weak that even a small amount of patchiness or clumpiness could give rise to an observed spectrum that is actually dominated by a small amount of reflection of the intrinsic continuum by the far side of the structure. In other words, even if a few percent of the reflection from the inner far side of the reprocessor is unobscured by material on the near side of the structure, the observed spectrum may be dominated by the far-side reflection, at least below  $\sim 10$  keV, at energies relevant for the Fe K $\alpha$  and Fe K $\beta$  line emission. We can mimic this far-side reflection spectrum with the face-on reflection spectrum in MYTORUS (and in fact the shape of the reflection spectrum from the inner faces of the torus is similar for all lines of sight that do not intercept the torus). In practice, to implement this, we simply add another Compton-scattered continuum table to the XSPEC model, but this time we fix the value of the inclination angle at  $0^\circ$  for that component only. This component has its own normalization, which we call  $A_{\text{S00}}$ . Thus, we have two Compton-scattered continua and each can be varied independently relative to the zeroth-order continuum with the parameters  $A_{\text{S00}}$  and  $A_{\text{S90}}$ . Each component has its own Fe K $\alpha$  and Fe K $\beta$  emission-line table, each of which has all of its parameters tied to the corresponding continuum model parameters.

The generalized geometrical setup that is approximated by the decoupled model is illustrated in Fig. 2. In addition to decoupling of the inclination angle, there is a provision for the line-of-sight column density ( $N_{\text{H,Z}}$ ) to be decoupled from the global average column density ( $N_{\text{H,S}}$ ), and this is particularly useful for modeling sources in which there is spectral variability due to matter moving in and out of the line sight. Only a single line-of-sight component needs to be utilized for a given observation, corresponding to the total line-of-sight column density. Individual clumps that move in and out of the line of sight are assumed to be too small to make a measurable difference to the Compton-scattered continuum and fluorescent line emission (if this is not the case, the differences would manifest themselves in the existing MYTS components).

Note that neither  $A_{\text{S00}}$  nor  $A_{\text{S90}}$  should be interpreted as covering factors. In a scenario in which the high-energy spectrum is dominated by the zeroth-order continuum, the global covering factor cannot be constrained even in principle. This is because any Compton-scattered and fluorescent line flux that is observed in the patchy reprocessor scenario would be dominated by back-side reflection from the inner far side of the X-ray reprocessor, through the unobscured patches. The amount of “leakage” due to these patches is not related to the bulk global covering factor. In fact, the parameter  $A_{\text{S00}}$  in this case would be more



**Table 3.** Parameters for the Baseline Model with MYTORUS Used in Decoupled Mode with a thermal Comptonized Intrinsic Continuum

Par. <sup>a</sup>	Comp. <sup>b</sup>	Symbol	Units	Status	Description
1	1	$C_{\text{PIN:XIS}}, C_{\text{PDS:MECS}}$	...	fixed	PIN:XIS or PDS:MECS cross-normalization ratio.
2	1	$C_{\text{GSO:XIS}}$	...	free	GSO:XIS instrumental cross-normalization ratio.
3	2	$N_{\text{H,Gal}}$	$10^{21} \text{ cm}^{-2}$	fixed	Galactic column density, fixed at 1.57.
4	3,6,8,12,14,19	$A_{\text{comptt}}$	$\text{ph. cm}^2 \text{ s}^{-1} \text{ keV}^{-1}$	free	Normalization of the intrinsic continuum (COMPTT).
5	3,6,8,12,14,19	$kT$	keV	fixed	Temperature of the Comptonizing plasma.
6	3,6,8,12,14,19	$\tau$		free	Optical depth of the Comptonizing plasma.
7	4,6,8,12,14	$N_{\text{H}}$	$10^{24} \text{ cm}^{-2}$	free	Column density of all reprocessor components.
8	5	$A_{\text{S00}}$	...	free	Scaling factor for a face-on scattered continuum.
9	7	$A_{\text{S90}}$	...	free	Scaling factor for an edge-on scattered continuum.
10	9	$\sigma_{\text{det}}$	eV	fixed <sup>c</sup> (eV)	Line width accounting for XIS resolution degradation.
11	10	$\text{FWHM}[\text{Fe K}\alpha, \text{Fe K}\beta]$	$\text{km s}^{-1}$	fixed <sup>d</sup> (100)	Intrinsic width of the Fe K $\alpha$ and Fe K $\beta$ lines.
12	11	$A_{\text{L00}}$	...	$= A_{\text{S00}}$	Scaling factor for fluorescent line emission.
12	13	$A_{\text{L90}}$	...	$= A_{\text{S90}}$	Scaling factor for fluorescent line emission.
14	15	$E_{\text{Fe XXV}}$	keV	free <sup>d</sup>	Gaussian centroid energy of the line emission at $\sim 6.7$ keV.
15	15	$\text{FWHM}[\text{Fe XXV}]$	$\text{km s}^{-1}$	free <sup>d</sup>	Intrinsic width of the line emission at $\sim 6.7$ keV.
16	15	$I_{\text{Fe XXV}}$	$\text{ph. cm}^2 \text{ s}^{-1}$	free	Flux of line emission at $\sim 6.7$ keV.
17	16	$E_{\text{Ni K}\alpha}$	keV	free <sup>d</sup>	Gaussian centroid energy of the Ni K $\alpha$ line.
18	16	$\text{FWHM}[\text{Ni K}\alpha]$	$\text{km s}^{-1}$	fixed <sup>d</sup>	Intrinsic width of the Ni K $\alpha$ line.
19	16	$I_{\text{Ni K}\alpha}$	$\text{ph. cm}^2 \text{ s}^{-1}$	free	Flux of the Ni K $\alpha$ line emission.
20	17	$f_s$	...	free	Scattering fraction due to optically-thin matter.
21	18	$N_{\text{H1}}$	$10^{21} \text{ cm}^{-2}$	free	Absorber covering optically-thin scattering zone.
22	20	$N_{\text{H2}}$	$10^{21} \text{ cm}^{-2}$	free	Absorber covering extended thermal emission zone.
23	21	$A_{\text{apec}}$	$\text{ph. cm}^2 \text{ s}^{-1} \text{ keV}^{-1}$	free	Normalization of the APEC model.
24	21	$kT_{\text{apec}}$	keV	free	Temperature of the APEC model.

<sup>a</sup> Parameter number. <sup>b</sup> Model component(s) that the parameter appears in (corresponding to the model component numbers in the model expression shown in §4.5.2). <sup>c</sup> Determined from fitting calibration source data (see §2.1). <sup>d</sup> The Gaussian emission-line centroid energies, and the intrinsic width of the Fe XXV line were initially allowed to float but they were then frozen at their best-fitting values in order to obtain robust statistical errors on the other parameters of interest. A single intrinsic width is associated with the Fe K $\alpha$  and Fe K $\beta$  lines, and this width, along with that of the Ni K $\alpha$  line was fixed at  $100 \text{ km s}^{-1}$  FWHM since the lines were found to be unresolved. Upper limits were derived by allowing the two line widths to float in turn (see §6 and §7).

Although the decoupled MYTORUS model involves some *ad hoc* parameterization in order to account for the unknown details of the exact geometry of the X-ray reprocessor and its unknown clumpiness, the procedure is different to the current practice of using the inappropriate geometry of disk reflection (in which the disk has an infinite column density), plus zeroth-order continuum extinction that has incorrect physics, along with Fe K $\alpha$  line emission that cannot be related to a physical reprocessor. The line-of-sight column density and intrinsic luminosity derived from the latter model may not have simple physical interpretations. Moreover, the proper use of a finite column density for the material responsible for the Compton-scattered continuum produces a rich variety of spectral shapes that cannot be produced by standard disk-reflection spectra. Residuals in spectral fits using the disk-reflection models might therefore be misinterpreted and erroneously identified with a different origin.

#### 4.6 Other Models of the Compton-thick X-ray Reprocessor

We will also refer to spectral fits using the toroidal and spherical X-ray reprocessor models of BN11, implemented using the XSPEC tables `torus1006.fits` and `sphere0708.fits` respectively (see BN11 for details). The model parameter setup for the BN11 toroidal model is essentially similar to that of the MYTORUS model in Table 2, with two exceptions. One is that there are no parameters corresponding to  $A_S$  and  $A_L$ , because neither the Compton-scattered continuum nor the fluorescent line spectrum can be varied with respect to the zeroth-order continuum. The second difference is that there is an extra parameter in the BN11 torus model that corresponds to the half-opening angle of the toroidal structure, which therefore controls the global covering factor (which can be varied between 0.1 and 0.9). For the BN11 spherical model, the parameter setup is again similar to that for the BN11 toroidal model, except that the covering factor is effectively fixed at 1.0, and there is no inclination angle parameter because of the spherical symmetry. Two extra parameters allow element abundances to be free. The spherical model is currently the only Compton-thick reprocessor model available that allows element abundances to be

free parameters. We call the two parameters  $X_{\text{Fe}}$  and  $X_{\text{M}}$ , where the former is the Fe abundance relative to the adopted solar value, and the latter is a single abundance multiplier for C, O, Ne, Mg, Si, S, Ar, Ca, Cr, and Ni relative to their respective solar values. The solar abundances adopted in the BN11 spherical model are the same as those used in the MYTORUS model (Anders & Grevesse 1989). The column density in the spherical model,  $N_{\text{H}}$ , is the radial column density. A technical issue with the both of the BN11 models is that the energies of the fluorescent emission lines cannot be varied. This is problematic because the signal-to-noise ratio of the NGC 4945 *Suzaku* data is so high that instrumental calibration errors and/or mild ionization cannot be ignored. The spectral fitting is highly sensitive to offsets as small as 10 eV. To accommodate the inflexibility of the BN11 models, we first allowed the redshift parameter to float and let the Fe K $\alpha$  line drive the spectral fits to the optimal redshift. The redshift was then frozen permanently at the best-fitting value before proceeding with the full spectral-fitting analysis.

#### 4.7 Spectral Fitting

We used XSPEC (Arnaud 1996) v12.6<sup>8</sup> for spectral fitting (Arnaud 1996). Galactic absorption with a column density of  $1.57 \times 10^{21} \text{ cm}^{-2}$  (Heiles & Cleary 1979) was included in all of the models described hereafter and its inclusion will be implicitly assumed. For all absorption components including the Galactic one, we used photoelectric cross sections given by Verner et al. (1996). Element abundances from Anders & Grevesse (1989) were used throughout. All astrophysical model parameter values will be given in the rest frame of NGC 4945, unless otherwise stated. Due to the large number of spectral fits and the large variety of combinations of model components and parameters, for the sake of brevity, certain quantities and details pertaining to particular spectral fits will be given in the tables of results and not repeated again in the text, unless it is necessary. Specifically, we are referring to the number of free parameters in a fit, the number of interesting parameters, the number of degrees of freedom, the null hypothesis probability, and the  $\Delta\chi^2$  criteria for the derivation of statistical errors. In most cases we give 68% confidence multiparameter errors, since these  $1\sigma$  errors can be used in future statistical analyses of samples of AGN. However, in some cases, certain parameters have to be frozen for the sake of stability of a spectral fit, and in that case those parameters are allowed to be free, one parameter at a time, in order to derive statistical errors. For these, one-parameter, 90% confidence errors are given. Further details will be given on a case-by-case basis.

For each spectral fit we will give the observed fluxes,  $F_{\text{obs}}$ , and the observed (rest-frame) luminosities,  $L_{\text{obs}}$ , in various energy bands, in the tables of spectral-fitting results. These quantities are not corrected for absorption or Compton scattering in either the line-of-sight material, or in the circumnuclear material. These fluxes and luminosities will not be discussed until all of the spectral fits have been presented. At that point, in §8, we will present and discuss the calculated intrinsic continuum luminosities for all of the spectral fits, as well as the ratio of the luminosities to the Eddington luminosity,  $L_{\text{Edd}}$ . For a black-hole mass of  $1.4 \times 10^6 M_{\odot}$ ,  $L_{\text{Edd}} = 1.77 \times 10^{44} \text{ erg s}^{-1}$ . We use a standard cosmology of  $H_0 = 70 \text{ km s}^{-1} \text{ Mpc}^{-1}$ ,  $\Lambda = 0.73$ ,  $q_0 = 0$  throughout the paper.

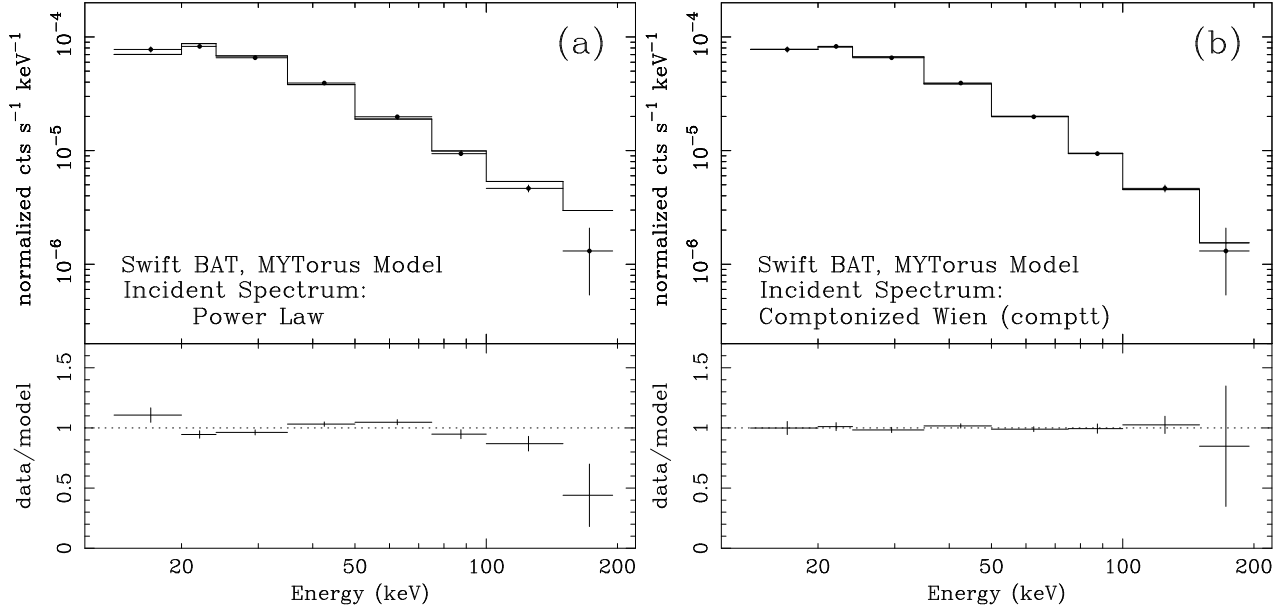
### 5 SPECTRAL FITS WITH ONLY A ZERO-ORDER CONTINUUM

In this section we investigate spectral solutions in which the spectra above 10 keV are fitted *only* with the zeroth-order continuum. The Compton-scattered continuum cannot of course be zero because the model Fe K $\alpha$  emission-line flux cannot be zero. However, if we are looking for solutions in which the Compton-scattered continuum is negligible compared to the zeroth-order continuum, we can work with the approximation of *no* Compton-scattered continuum and *no* fluorescent line emission when we are fitting data above 10 keV. We can even omit the optically-thin scattered continuum and we can certainly omit the soft X-ray thermal emission components (and any absorption only associated with those components). We can then use the results from these simplified fits as a guide for setting up the correct, full-bandpass model that *will* include the Compton-scattered continuum and fluorescent line emission. Moreover, since the zeroth-order continuum is obtained from the intrinsic X-ray continuum simply by multiplying by an energy-dependent factor, we can use an arbitrary incident continuum model with all of its key parameters allowed to float (as opposed to having to generate tables that only allow a restricted number of free parameters).

#### 5.1 Zeroth-order Continuum Fits to the Swift BAT Data

We begin by first reporting the results of fitting the 58-month *Swift* BAT spectrum using a power-law incident continuum. There were only three free parameters,  $A_{\text{PL}}$ ,  $\Gamma$ , and  $N_{\text{H}}$  (see §4.5) and 8 spectral channels in the spectrum (i.e., 5 degrees of freedom). It can be seen from Fig. 3(a) that the fit is very poor (the *reduced*  $\chi^2$  value is 5.65), and the data/model residuals in Fig. 3(a) show significant deviations across the entire 14–195 keV band, but in particular show a high-energy rollover

<sup>8</sup> <http://heasarc.gsfc.nasa.gov/docs/xanadu/xspec/>



**Figure 3.** Spectra and data/model ratios for the *Swift* BAT 58-month data for NGC 4945 where the model consists of only the zeroth-order component of the MYTORUS model. Shown in (a) are the results for an intrinsic power-law continuum (the photon index and column density were free parameters). Shown in (b) are the results for a thermally Comptonized incident spectrum (the plasma temperature and column density were free parameters). The power-law incident continuum gives a poor fit. See Table 4 and §5 for details.

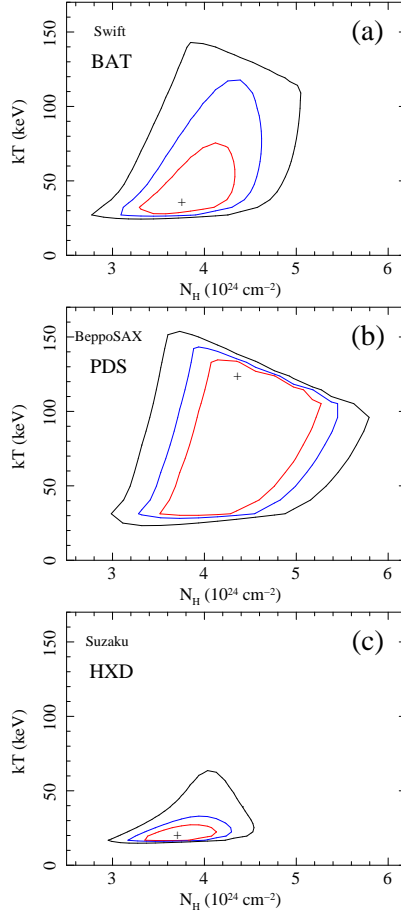
**Table 4.** NGC 4945 *Swift* BAT Spectral-Fitting Results.

Parameter	zeroth-order only	MYTORUS (coupled)	MYTORUS (coupled)	BN11 (torus)	BN11 (sphere)
Intrinsic Continuum	COMPTT	POWER LAW	COMPTT	POWER LAW	POWER LAW
Free Parameters	4	4	4	4	3
Interesting Parameters	3	3	3	3	2
$\chi^2$	2.05	2.38	0.99	1.90	4.60
Degrees of Freedom	4	4	4	4	5
Reduced $\chi^2$	0.51	0.596	0.250	0.474	0.920
Null probability	0.727	0.666	0.910	0.755	0.467
$\Delta\chi^2$ criterion (68% confidence)	3.50	3.50	3.50	3.50	2.28
$\Gamma$	...	$1.83^{+0.15}_{-0.22}$	...	$1.59^{+0.27}_{-0.03}$	$1.75^{+0.02}_{-0.03}$
$\tau$	$0.94^{+0.55}_{-0.76}$	...	$0.99^{+0.18}_{-0.20}$	...	...
$kT$	$36^{+62}_{-10}$	...	$51^{+16}_{-17}$	...	...
$N_H$ ( $10^{24} \text{ cm}^{-2}$ )	$3.78^{+0.71}_{-0.63}$	$> 3.37$	$3.13^{+0.77}_{-0.58}$	$> 2.95$	$2.74^{+0.27}_{-0.25}$
$\theta_{\text{torus}}$ (degrees) <sup>a</sup>	...	60(f)	60(f)	$59.7^{+0.3}_{-3.8}$	...
$\theta_{\text{obs}}$ (degrees) <sup>b</sup>	...	78( $> 60$ )	90(f)	87.1 (f)	...
$F_{\text{obs}}[10-100 \text{ keV}]$ ( $10^{-11} \text{ erg cm}^{-2} \text{ s}^{-1}$ )	16.8	18.2	17.8	18.4	18.2
$F_{\text{obs}}[14-195 \text{ keV}]$ ( $10^{-11} \text{ erg cm}^{-2} \text{ s}^{-1}$ )	24.6	25.1	25.0	24.8	25.6
$L_{\text{obs}}[10-100 \text{ keV}]$ ( $10^{42} \text{ erg s}^{-1}$ )	1.30	1.41	1.38	1.42	1.41
$L_{\text{obs}}[14-195 \text{ keV}]$ ( $10^{42} \text{ erg s}^{-1}$ )	1.91	1.94	1.94	1.92	1.98

Results for the *Swift* BAT data for NGC 4945 from spectral-fitting with Compton-thick reprocessor models. Details can be found in §5 for the fit with only the zeroth-order continuum, and for the remaining fits in §6. The BN11 torus and spherical fits refer to the models of Brightman & Nandra (2011). All fluxes and luminosities are in the observed frame, uncorrected for absorption or Compton scattering.

<sup>a</sup> Torus opening half-angle (the maximum allowed for the BN11 model is 87.1 degrees). <sup>b</sup> Inclination angle of the observer with respect to the azimuthal symmetry axis of the torus.



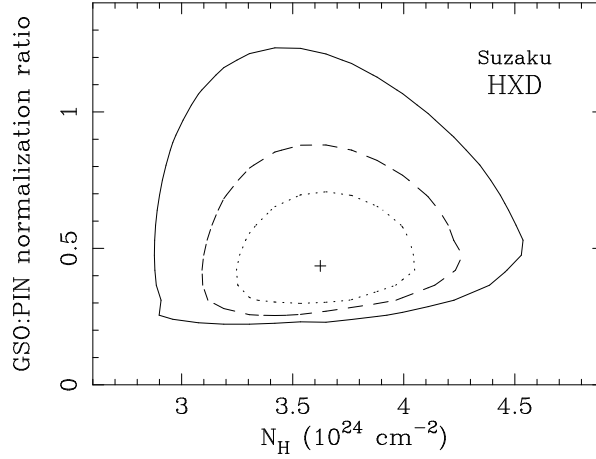


**Figure 4.** Confidence contours of the intrinsic continuum Comptonizing plasma temperature ( $kT$ ) versus column density of the X-ray reprocessor. The contours were obtained from spectral fits to NGC 4945 data where the model consisted only of the zeroth-order continuum for a thermally Comptonized spectrum incident on a Compton-thick X-ray reprocessor. For these fits only data above 10 keV were utilized because in that regime the Compton-scattered continuum in NGC 4945 may be negligible in some physical scenarios, such as a ring-like Compton-thick patchy X-ray reprocessor observed edge-on. The three sets of contours shown in (a), (b), and (c) correspond to spectral fits to data from the *Swift* BAT, *BeppoSAX* PDS, and *Suzaku* HXD (PIN and GSO) respectively. The red, blue, and black lines correspond to two-parameter, 68%, 90%, and 99% confidence levels respectively. See §5 for details.

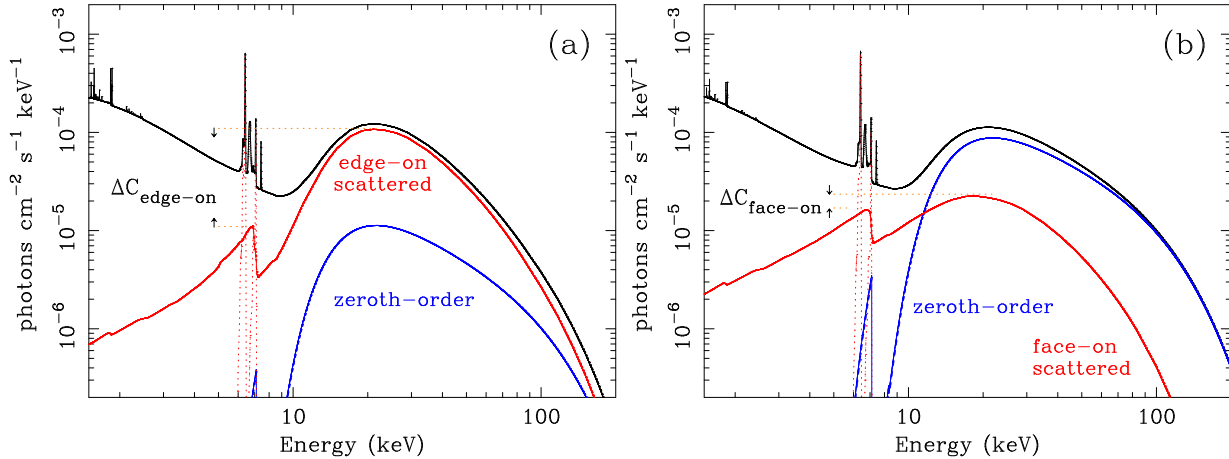
compared to a power-law. The probability of obtaining the measured  $\chi^2$  value or higher is  $3.2 \times 10^{-5}$ , meaning that the model can be formally rejected at greater than the  $4.1\sigma$  level. We conclude that if the high-energy X-ray spectrum in NGC 4945 is to be dominated by the zeroth-order continuum, the intrinsic X-ray continuum cannot be a simple power law, and the spectrum has to start rolling over below  $\sim 100$  keV. Therefore, we replaced the power-law continuum with the Comptonized thermal continuum model, COMPTT (as described in §4.5.2). The model now had 4 free parameters, namely the overall normalization, plasma optical depth ( $\tau$ ) and temperature ( $kT$ ), and the line-of-sight column density ( $N_H$ ). An excellent fit was obtained, with  $\chi^2 = 2.05$  for 4 degrees of freedom, as can be seen in Fig. 3(b), which shows the data, model, and data/model ratio. We obtained best-fitting parameters  $\tau = 0.94^{+0.55}_{-0.76}$ ,  $kT = 36^{+62}_{-10}$  keV, and  $N_H = 3.78^{+0.71}_{-0.63} 10^{24} \text{ cm}^{-2}$  (see Table 4). The best-fitting parameters are also given in Table 4, where they can be compared with parameters from other models that were fitted to the *Swift* BAT (to be described below). In Fig. 4(a) we show the two-parameter, 68%, 90%, and 99% confidence contours of  $kT$  versus  $N_H$ . We see that the 99% confidence lower limit on  $kT$  is flat (at  $\sim 20$  keV) over most of the allowed range of  $N_H$ , and the 99%, two-parameter upper limit on  $kT$  is  $\sim 140$  keV.

## 5.2 Zeroth-order Continuum Fits to the Suzaku and BeppoSAX Data

We repeated the exercise, this time fitting high-energy data from *BeppoSAX* and *Suzaku*, with the same simple model that includes only the zeroth-order continuum (for an intrinsic continuum modeled by COMPTT). Confidence contours of  $kT$  versus  $N_H$  are shown in Fig. 4(b) and Fig. 4(c) for the *BeppoSAX* and *Suzaku* data respectively. Since we were explicitly examining the high-energy spectra, we used only the PDS data for *BeppoSAX* (see §2.2) and only the PIN and GSO data for *Suzaku* (see §2.1). All of the data sets gave a consistent, albeit large, range in  $kT$  and  $N_H$ . The *Suzaku* data gave the tightest constraints



**Figure 5.** Confidence contours obtained from spectral fits to the NGC 4945 PIN and GSO data using a thermally Comptonized spectrum incident on a Compton-thick reprocessor. Only the zeroth-order continuum component of the MYTORUS model was utilized, modeling physical scenarios in which the Compton-scattered continuum is negligible above 10 keV. The relative normalization factor for the PIN and GSO was a free parameter in the fits, and the contours show the value of this parameter versus the line-of-sight column density,  $N_H$ , of the reprocessor (the Comptonizing plasma temperature,  $kT$  was also a free parameter). The dotted, dashed, and solid lines correspond to two-parameter, 68%, 90%, and 99% confidence levels respectively. It can be seen that  $N_H$  is uncorrelated with the GSO:PIN normalization ratio. See §5 for details.



**Figure 6.** A demonstration of why an edge-on Compton-scattered spectrum forces a solution in which the magnitude of the zeroth-order continuum is substantially diminished compared to the Compton-scattered continuum. Shown in (a) is a MYTORUS model fit to the *Suzaku* data of NGC 4945 with a decoupled, edge-on scattered continuum. In this case, the contrast,  $\Delta C_{\text{edge-on}}$ , between the peak of the “Compton hump” and the scattered continuum in the Fe K band, is so large that in order to fit the Fe K $\alpha$  line, the magnitude of the scattered continuum is forced to be much larger than the zeroth-order continuum. In (b) the edge-on scattered continuum is replaced by a decoupled face-on scattered continuum, and in this case the contrast,  $\Delta C_{\text{face-on}}$ , is much less than  $\Delta C_{\text{edge-on}}$ , and the Fe K $\alpha$  line flux is much larger, so a solution in which the zeroth-order continuum dominates is possible. Note that the black curves show the total spectra including all of the model components shown in Table 3, but not all of the individual components are shown separately for the sake of clarity. See §5 for details.

on  $kT$  and  $N_H$ , with best-fitting values of 22 keV and  $3.7 \times 10^{24} \text{ cm}^{-2}$  respectively. We do not give the exact parameters and statistical errors derived from the *BeppoSAX* and *Suzaku* fits because these parameters will change when they are derived from full model fits that will include the Compton-scattered continua and fluorescent lines (and the data below 10 keV). Since the MYTORUS Compton-scattered continuum tables have to be calculated for fixed values of  $kT$ , we will use the contours in Fig. 4 as a guide for the full-band spectral fits (see §7). We note that for the *Suzaku* confidence contours in Fig. 4, the GSO to XIS cross-normalization ratio was a free parameter in the spectral fit. Fig. 5 shows two-parameter, 68%, 90%, and 99% confidence contours for this cross-normalization versus  $N_H$ , and we see that the ratio is uncorrelated with the derived column density. The range in the ratio is fairly large, but nevertheless consistent with the results for 3C 273 given in the appendix.

### 5.3 A Requirement of the Compton-scattered Continuum If the High-energy Spectrum is Dominated By the Zeroth-order Continuum

We now demonstrate that if we are looking for Compton-thick solutions in which the high-energy spectrum is dominated by the zeroth-order continuum, then the Compton-scattered continuum and Fe K $\alpha$  line emission must be dominated by photons originating from back-illumination and then reaching the observer along paths that do not intercept the Compton-thick structure. In other words, the structure must be clumpy, allowing a reflection continuum to reach the observer either from the far inner side of a toroidal structure, or from an extended and dispersed distribution of matter (as in NGC 4945). The reason for this constraint is that the Fe K $\alpha$  line emission and Compton-scattered continuum below 10 keV, relative to the Compton-hump peak flux in the  $\sim 10 - 30$  keV range, is much larger for unobstructed reflection than it is from reflection from matter intercepting the line of sight (e.g., see Yaqoob et al. 2010). If the reprocessor were not patchy, then raising the Fe K $\alpha$  line flux high enough to account for the observed spectral data also raises the Compton-scattered flux so high that the Compton hump necessarily swamps the zeroth-order continuum. This is illustrated in Fig. 6, which shows model spectra in which the MYTORUS Compton-scattered continuum and fluorescent lines are decoupled from the zeroth-order continuum (see §4.5.2), comparing the two cases in which the reflection features are observed edge-on (Fig. 6(a)) and face-on (Fig. 6(b)). Both of these extreme cases fit the full-band (three-instrument) *Suzaku* data, but Fig. 6 shows that only the face-on case allows the zeroth-order continuum to dominate above 10 keV. The intrinsic continuum in Fig. 6 was the COMPTT model with  $kT = 22$  keV. We do not give the remaining model parameters here because detailed fits with variations on this decoupled MYTORUS model will be given below, in §7. The purpose of Fig. 6 is only to illustrate the need for a clumpy X-ray reprocessor if the hard X-ray continuum variability in NGC 4945 is to be produced by the zeroth-order continuum. In practice there is likely to be some contribution from both the far-side unobscured reflection, and the near-side emission from the obscuring material, but the former component must dominate over the latter component. Even when this condition is met, the Compton-scattered continuum spectrum cannot be too high, otherwise it would again dominate over the zeroth-order continuum and we are not looking for those solutions here (which will be discussed in §6).

## 6 SPECTRAL FITS WITH COUPLED REPROCESSOR MODELS

In this section we present the results of fitting the *Suzaku*, *BeppoSAX*, and *Swift* BAT spectra with coupled models of the Compton-thick X-ray reprocessor (see §4). We fitted three sets of models, using MYTORUS, the BN11 torus, and the BN11 sphere, for the Compton-thick reprocessor. We tried using both a simple power-law and Comptonized thermal intrinsic continuum in the case of the MYTORUS models. The BN11 models do not allow any other intrinsic continuum aside from a power law.

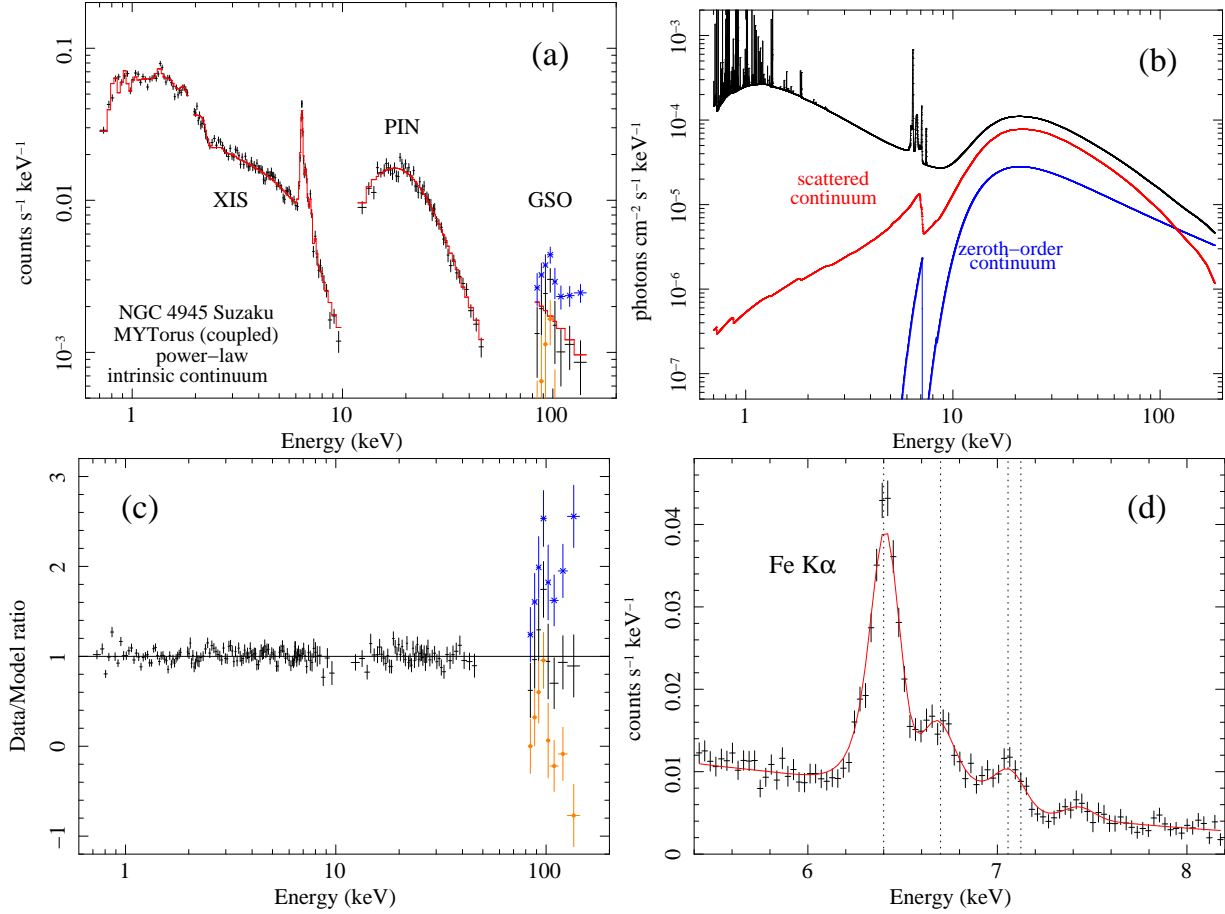
### 6.1 BN11 toroidal model

We found that we could not obtain an acceptable fit with the BN11 toroidal model to either the *Suzaku* data or the *BeppoSAX* data, even with all parameters of the model allowed to float, including the toroidal opening angle. (The other free parameters are the same as those of the MYTORUS model.) The best values of the reduced  $\chi^2$  that could be obtained were 1.82 and 4.40 for the *Suzaku* and *BeppoSAX* data respectively. For the *Suzaku* fit, the probability for obtaining such a bad fit or worse, due to statistical fluctuations alone, is  $3.5 \times 10^{-19}$ . For the *BeppoSAX* data, the null hypothesis probability is 10 orders of magnitude worse. One reason for the poor fits is that the geometry of the toroidal BN11 model is rather peculiar in that all rays from the intrinsic X-ray continuum are presented with the same zeroth-order column density, whereas in the MYTORUS model, rays incident at the equator are presented with a larger column density than those incident away from the equator. This results in very different emergent spectra from the BN11 model compared to the MYTORUS model. The shape of the  $\sim 10 - 50$  keV spectral hump in the BN11 model severely mismatches the data, and the Fe K $\alpha$  line fluxes associated with the reprocessed continuum cannot match the data.

The *Swift* BAT data, having a lower statistical quality than the other data sets, did yield an acceptable fit, but the orientation of the torus had to be fixed at the highest inclination allowed by the model, and only a lower limit could be obtained on  $N_H$ . The results for this fit are shown in Table 4.

### 6.2 *Suzaku* Fits with the Coupled MYTORUS Model

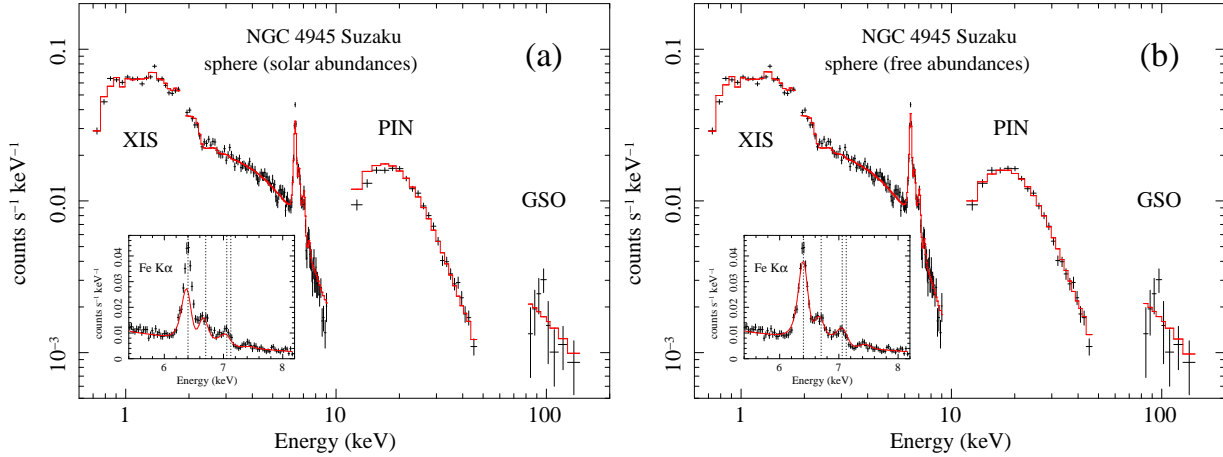
For the MYTORUS model, good fits were obtained for the *Suzaku* data with both intrinsic continuum models, and the results are shown in Table 5. The difference in  $\chi^2$  between the two fits is not significant, bearing in mind the complexity of the models and systematic errors that we do not account for. Note that the parameter  $A_S$  is free in both fits and the best-fitting values center around unity, which corresponds to the default, steady-state configuration of MYTORUS. The orientation of the torus is essentially edge-on for both intrinsic continua. We will discuss the column density after discussing the remaining fits.



**Figure 7.** Results of spectral fitting to the NGC 4945 *Suzaku* data with the default MYTORUS X-ray reprocessor model (see §6 for details). In the default configuration, the zeroth-order continuum is linked to the scattered continuum (and fluorescent lines) by virtue of the specific geometry adopted for the MYTORUS model. In this configuration, the best fit gives a Compton-scattered continuum that dominates over the zeroth-order continuum below  $\sim 100$  keV. In this scenario, the X-ray reprocessor must be compact enough for the Compton-scattered continuum to respond to intrinsic continuum variability. (a) The counts spectra overlaid with the folded best-fitting model. The three data groups from left to right correspond to data from the XIS, HXD/PIN, and the HXD/GSO. The data from XIS0, 1, 2, and 3 are combined into a single spectrum. For clarity, for some energy ranges, the data shown in the plot are binned more coarsely than the binning used for the actual spectral fitting. For the GSO, the effect of a systematic error in the background model of  $-2\%$  and  $+2\%$  is shown in blue and brown respectively (see text). (b) The total best-fitting model photon spectrum (black), with the contribution from the Compton-scattered continuum and the zeroth-order continuum shown in red and blue, respectively. Other constituent components are not shown for clarity (but are included in the total spectrum). (c) The ratios of the data to the best-fitting model. Again, two additional ratios are shown for the GSO, corresponding to the background-subtraction systematic errors used in (a). (d) A close-up zoom of the Fe K region in panel (a). From left to right, the dotted lines correspond to the energies of Fe I  $K\alpha$ , Fe XXV, Fe I  $K\beta$ , and the neutral Fe K edge. The bump above the Fe K edge is the Ni  $K\alpha$  line.

The fit to the *Suzaku* data with the power-law intrinsic continuum is shown in Fig. 7. The folded model and counts spectra are shown in Fig. 7(a), the best-fitting photon spectrum is shown in Fig. 7(b), and the data/model ratios are shown in Fig. 7(c). It can be seen that an excellent fit is obtained over the whole bandpass. In this fit, the continuum above 10 keV is dominated by the Compton-scattered continuum, not the zeroth-order continuum. In order to assess the importance of the GSO background-subtraction systematics, we applied systematic offsets to the background spectrum of  $-2\%$  and  $+2\%$  (the extreme values for the advertised systematic errors in the GSO background model). The results are shown in Fig. 7, panels (a) and (c), from which it can be seen that the negative offset can result in an error in the background-subtracted spectrum of up to  $\sim 150\%$ , and the positive offset can result in negative counts in the background-subtracted spectrum. The GSO:XIS fitted normalization parameter very likely includes some compensation for any background-subtraction systematic errors.

The folded model and counts spectrum zoomed in on the Fe K region is shown in Fig. 7(d), and it can be seen that the detailed fit is excellent. All four emission lines (Fe  $K\alpha$ , Fe XXV, Fe  $K\beta$ , and Ni  $K\alpha$ ), and the Fe K edge are very well modeled. The line emission at  $\sim 6.7$  keV must originate in a region that is distinct from the one that produces the Fe  $K\alpha$ , Fe  $K\beta$ , and Ni  $K\alpha$  lines because these latter three lines, and the Fe K edge are modeled with neutral matter. It also appears that no



**Figure 8.** Spectral fits to the *Suzaku* data for NGC 4945, showing the BN11 spherical model overlaid on the counts spectra for (a) solar abundances, and (b) the relative abundance parameters for Fe ( $X_{\text{Fe}}$ ) and the other metals ( $X_{\text{M}}$ ) free (see §6.4). In each case a zoomed view is shown of the spectral region containing the Fe  $K\alpha$ , Fe  $K\beta$ , Ni  $K\alpha$  lines, and the Fe K absorption edge. The fit with solar abundances illustrates how the column density required to fit the  $\sim 10 - 50$  keV spectral peak underpredicts the Fe  $K\alpha$  emission line. This fit was performed by omitting the 6–8 keV data and finding the best fit, and then including the 6–8 keV data for the plot (after inserting the required Fe XXV emission line at  $\sim 6.7$  keV). Allowing the abundances to float then enables a good fit to both the Fe  $K\alpha$  line and the Compton hump, as shown in Fig. 8(b). See §6.4 and Table 5 for details.

Fe XXVI line emission is required: including an additional unresolved Gaussian emission-line component at 6.966 keV gives a two-parameter, 90% confidence upper limit on the EW of 34 eV.

### 6.3 *BeppoSAX* and *Swift* BAT Fits with the Coupled MYTORUS Model

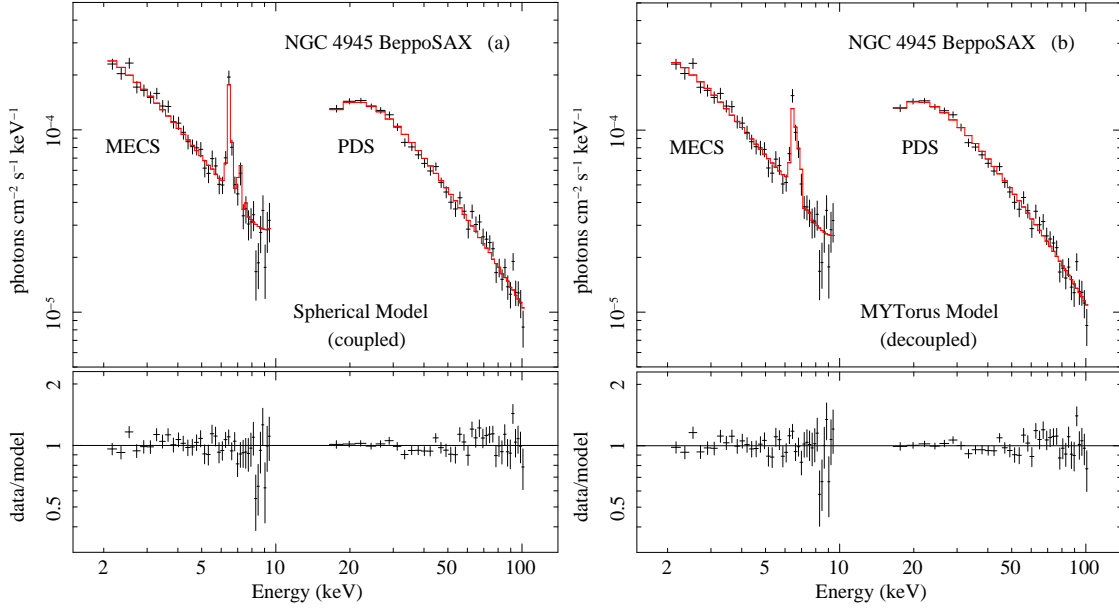
Next, we describe the fits to the *BeppoSAX* data. In this case, we were not able to obtain an acceptable fit with a power-law intrinsic continuum and MYTORUS. The best value of the reduced  $\chi^2$  that we obtained was 1.91, with a null probability of  $8.5 \times 10^{-6}$ . However, when we used the Comptonized thermal model for the intrinsic continuum we did obtain an acceptable fit (see Table 5) but with one very important concession. That is, the parameter  $A_S$  is required to be an order-of-magnitude smaller than unity ( $A_S = 0.101^{+0.149}_{-0.068}$ ,  $A_L \equiv A_S$ ), which means that the Compton-scattered continuum is heavily suppressed (but the fluorescent line spectrum is still high enough to fit the Fe  $K\alpha$  line).

Spectral-fitting results to the *Swift* BAT spectrum with the MYTORUS model, using both intrinsic continuum models, are shown in Table 4, and acceptable fits were obtained in both cases. The parameter  $A_S$  was fixed at 1.0 in both cases.

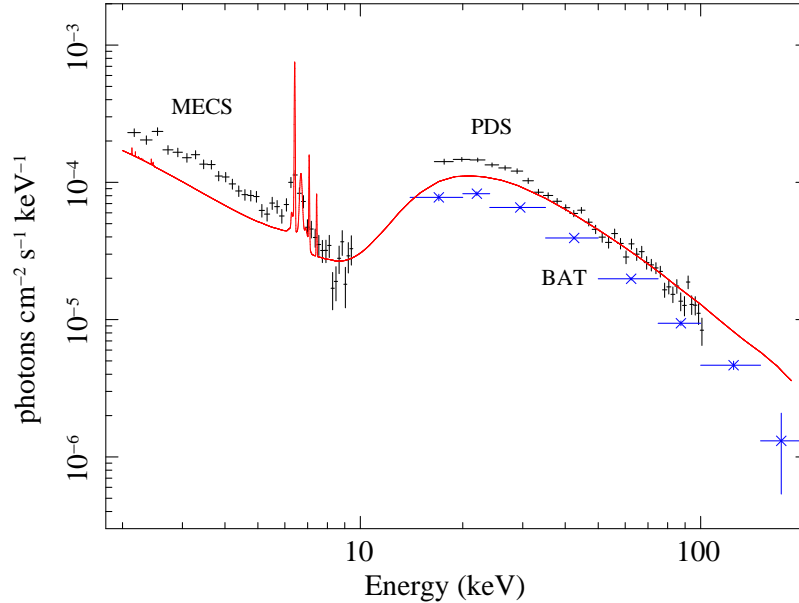
### 6.4 Spectral Fits with a Spherical Model

Finally, we fitted the BN11 spherical model to all the data sets (see §4.6 for details of this spherical model). We could not obtain an acceptable fit to the *Suzaku* with solar abundances. The best-fitting reduced  $\chi^2$  value was 1.51, with a null hypothesis probability of  $1.7 \times 10^{-9}$ . The poor fit is illustrated in Fig. 8(a), which shows that the shape of the Compton hump is not correctly reproduced and the Fe  $K\alpha$  line flux is not well-fitted. Essentially, the column density that is required to correctly fit the Compton hump, severely underpredicts the Fe  $K\alpha$  line flux, and this is shown in the zoomed-in panel in Fig. 8(a). However, when we allowed the relative Fe abundance,  $X_{\text{Fe}}$ , to float, the best-fitting  $\chi^2$  value dropped by 83.0 for the addition of a single free parameter, and a good fit was obtained. On the other hand, a reduction in  $\chi^2$  of less than 4 was obtained by allowing the relative abundance of the other elements ( $X_{\text{M}}$ ) to float (see §4.6 for details of the meaning of the abundance parameters). The data and model, including a zoomed view of the Fe K spectral region, are shown in Fig. 8(b), and the best-fitting parameters and statistical errors are shown in Table 5. It can be seen that the required enhancement of the Fe abundance relative to solar is very modest ( $X_{\text{Fe}} = 1.44^{+0.25}_{-0.22}$ ), yet the difference in the goodness of fit is substantial. It is also important to realize that varying the Fe abundance in a Compton-thick medium has effects well beyond the Fe K spectral region because of the high absorption optical depth over a broad energy range, and the indirect effect on Compton scattering. The best-fitting relative abundance of the other elements,  $X_{\text{M}} = 0.94^{+0.11}_{-0.07}$ , was consistent with unity. The best-fitting  $\chi^2$  value of 447.2 for 354 degrees of freedom indicates a marginally worse fit than the coupled MYTORUS model, and this is due to a small underprediction of the Fe  $K\alpha$  line flux, as can be seen in Fig. 8(b). However, less than full covering of the X-ray reprocessor (or equivalently, some patchiness) would alleviate the problem.

We have shown the spherical model solutions mainly in the interest of application to AGN other than NGC 4945. In the



**Figure 9.** Spectral fits to the *BeppoSAX* data for NGC 4945, showing two models overlaid on the unfolded spectra (top panels), and the data/model ratios (bottom panels). (a) A fit with the spherical model of Brightman and Nandra (2011). The model parameters are shown in Table 5 (see §6 for details). (b) A fit with the decoupled MYTORUS model (mimicking a patchy reprocessor). The incident, intrinsic continuum for the model fit for this fit has a thermally Comptonized spectrum with the plasma temperature,  $kT$ , fixed at 80 keV. The model parameters are shown in Table 3 (see §7 for details). For clarity, the data in some energy ranges is binned more coarsely than the binning used for the actual spectral fitting. Note that the unfolded spectra are for illustration purposes only and are by their nature model-dependent so should be interpreted with caution (the fitting is performed on the counts spectra not the unfolded spectra).



**Figure 10.** The best-fitting coupled MYTORUS model (red curve) with a power-law intrinsic continuum that was fitted to the NGC 4945 *Suzaku* data (taken in 2006, January), overlaid on the noncontemporaneous *BeppoSAX* data (black), and on the *Swift* BAT data (blue). The *BeppoSAX* data were taken in 1999, July, and the *Swift* BAT data are averaged over 58 months. The best-fitting *Suzaku* model is the same as the one shown in Fig. 7(b) and the model parameters are shown in Table 5 (see §6 for details). No corrections have been made for the different cross-normalizations of the different instruments for this plot. Also, the *BeppoSAX* and *Swift* BAT photon spectra were only crudely constructed by unfolding using only a simple power-law continuum with absorption, so they should be interpreted with caution. The purpose of the plot is only to show the approximate relative magnitudes of the different spectra in the Fe K band ( $\sim 6 - 8$  keV), and around the Compton hump (between  $\sim 10 - 50$  keV).

case of NGC 4945, in principle, the deficit in the Fe K $\alpha$  line flux in the solar-abundance model could be made up by the Fe K $\alpha$  line emission from the extended region spatially resolved by *Chandra* (and indeed this component should be included). However, none of the spherical model solutions are applicable to NGC 4945 because the continuum above 10 keV is dominated by the Compton-scattered continuum, overwhelming the zeroth-order continuum, and this is inconsistent with the variability of the high-energy continuum and the lack of simultaneous variability of the Fe K $\alpha$  line flux (as reported in Marinucci et al. 2012). Note that when applying the spherical model to other sources, it should be remembered that it is not quite self-consistent because it is *required* that the X-ray reprocessor is patchy or has less than full covering, otherwise there would be no optically-thin scattered continuum, so that the X-ray continuum below  $\sim 10$  keV would be more suppressed than it actually is, and it would be decreasing in magnitude with decreasing energy.

We also obtained an acceptable fit with the spherical model to the *BeppoSAX* data, again with the relative Fe abundance allowed to float, but we had to fix the relative abundance of the other heavy elements at their solar values in order to obtain a stable spectral fit. The results are given in Table 5, and the data, model, and data/model ratios are shown in Fig. 9(b). The best-fitting relative Fe abundance is  $1.03^{+0.52}_{-0.37}$ , and this is statistically consistent with the corresponding result obtained from the *Suzaku* data. The MYTORUS solution to the *BeppoSAX* data is physically very different to the spherical model solution. The former is dominated by the zeroth-order continuum, whereas the latter is dominated by the Compton-scattered continuum. However, the two solutions cannot be distinguished statistically (the  $F$ -test shows that the probability of obtaining the slightly higher  $\chi^2$  value, or higher, for the spherical model than the MYTORUS model is about 38%).

The BN11 spherical model gave an acceptable fit to the *Swift* BAT spectrum, and the results for solar abundances are shown in Table 4 (the abundance parameters could not be constrained).

## 6.5 Overview of the Parameters for the Coupled Models

In summary, we can say that for coupled models of the X-ray reprocessor, the *Suzaku* data for NGC 4945 prefer a spectrum in which the Compton-scattered continuum dominates over the zeroth-order continuum, and these data prefer a medium that has a substantial global covering factor (a few tenths to nearly full covering, or full covering with some patchiness). However, models in which the Compton-scattered continuum dominates are inconsistent with the continuum above 10 keV in NGC 4945 varying independently of the Fe K $\alpha$  line (Marinucci et al. 2012). On the other hand, two very different degenerate solutions can describe the *BeppoSAX* data. One solution has the spectrum dominated by the zeroth-order continuum, consistent with a ring-like geometry in which the X-ray reprocessor has a small covering factor. The other solution instead has the Compton-scattered continuum dominate the spectrum over the zeroth-order continuum, achieved by the full covering of the spherical model. It is true to say that both the *BeppoSAX* and *Suzaku* data are consistent with a nearly fully-covering (or patchy) spherical model, in which case no changes in covering factor are required going from the *BeppoSAX* observation to the *Suzaku* observation, but such a scenario can be ruled out for NGC 4945 because of the variability constraints discussed earlier. In the interest of modeling other AGNs, this scenario would require a global decrease of the column density by  $\sim 50\%$  between observations (see Table 5), and an Fe abundance up to  $\sim 50\%$  higher than solar (for both observations). We shall also see in §8 that the spherical model has an intrinsic luminosity that is more than an order of magnitude less than the zeroth-order-dominated spectrum. We defer to §8 for further discussion (after presenting the decoupled model fits). In the remainder of this section, we summarize some of the other results in Table 4 (for the *Swift* BAT data) and Table 5 (for *Suzaku* and *BeppoSAX*). Statistical errors for all of the parameters can be found in Table 4 and Table 5 but are not always quoted in the text. To aid the comparison between the *Suzaku*, *BeppoSAX*, and *Swift* BAT spectra, we have overlaid the best-fitting MYTORUS model for the *Suzaku* spectra (with an intrinsic power-law continuum) on the *BeppoSAX* and *Swift* BAT photon spectra in Fig. 10.

### 6.5.1 Continua

The temperature of the optically-thin thermal emission component is  $kT_{\text{apex}} = 0.260^{+0.046}_{-0.035}$  keV for both *Suzaku* fits with the MYTORUS model (Table 5), so it is not sensitive to the different models for the intrinsic continuum. The same temperature is obtained with the spherical model, albeit with slightly different statistical errors. The intrinsic luminosity of the optically-thin thermal component is  $2.9 \times 10^{40}$  erg s $^{-1}$  and this is not sensitive to the differences in any of the three coupled models fitted to the *Suzaku* data. The same is true for the column density associated with the region producing the thermal emission ( $N_{\text{H}2}$ ), and is  $3.8 \times 10^{21}$  cm $^{-2}$ . This optically-thin thermal emission continuum component is below the bandpass of both the *BeppoSAX* and *Swift* BAT data so its parameters cannot be constrained by those data. In the case of the *BeppoSAX* fits, the parameters of this continuum component, along with  $N_{\text{H}2}$ , were fixed at the values obtained from the *Suzaku* fits. (For the *Swift* BAT fits, this continuum component was omitted altogether.)

In the case of the power-law model for the intrinsic continuum applied to the *Suzaku* data with the MYTORUS model, the photon index is  $\sim 1.6$ . The power-law continuum is much flatter with the spherical reprocessor model ( $\Gamma < 1.5$ ), but it is steeper when the spherical model is applied to the *BeppoSAX* data ( $\Gamma \sim 1.8$ ). For the Comptonized thermal continuum we tried fits with MYTORUS tables for a range of values of  $kT$  that were consistent with the 99% confidence contours shown in

**Table 5.** NGC 4945 Spectral-Fitting Results with the Coupled Reprocessor Models

Parameter	<i>Suzaku</i>	<i>Suzaku</i>	<i>Suzaku</i>	<i>BeppoSAX</i>	<i>BeppoSAX</i>
Model	MYTORUS	MYTORUS	B11 sphere	MYTORUS	BN11 sphere
Intrinsic Continuum	POWER LAW	COMPTT	POWER LAW	COMPTT	POWER LAW
Free Parameters	13	14	13	8	7
Interesting Parameters	11	12	11	7	6
$\chi^2$ / degrees of freedom	440.6/354	435.1/353	447.2/354	85.8/70	92.5/70
Reduced $\chi^2$	1.24	1.23	1.26	1.23	1.32
Null Probability	$1.3 \times 10^{-3}$	$1.9 \times 10^{-3}$	$5.6 \times 10^{-4}$	0.095	0.037
$\Delta\chi^2$ criterion (68% confidence)	12.6	13.70	12.6	8.15	7.01
GSO:XIS normalization ratio	$0.446^{+0.084}_{-0.084}$	$0.567^{+0.110}_{-0.107}$	$0.404^{+0.076}_{-0.076}$	...	...
$\Gamma$ or $\tau$	$1.596^{+0.044}_{-0.035}$	$1.20^{+0.09}_{-0.12}$	$1.489^{+0.037}_{-0.031}$	$0.31^{+0.09}_{-0.10}$	$1.789^{+0.149}_{-0.026}$
$kT$ (keV)	...	$50^{+4}_{-4}$	...	80(f)	...
$N_H$ ( $10^{24}$ cm $^{-2}$ )	$3.48^{+0.22}_{-0.17}$	$3.62^{+0.26}_{-0.23}$	$2.17^{+0.18}_{-0.15}$	$4.55^{+1.38}_{-0.80}$	$3.05^{+0.48}_{-0.41}$
$\theta_{\text{obs}}$ (degrees)	$85.4^{+0.8}_{-0.6}$	$85.7^{+0.6}_{-0.7}$	...	$89.3^{+0.7}_{-3.6}$	...
$A_S$	$1.00^{+0.10}_{-0.26}$	$1.00^{+0.15}_{-0.17}$	...	$0.101^{+0.149}_{-0.068}$	...
$A_L$	$= A_S$	$= A_S$	...	$= A_S$	...
$X_{\text{Fe}}$	1.0(f)	1.0(f)	$1.44^{+0.25}_{-0.22}$	1.0(f)	$1.03^{+0.52}_{-0.37}$
$X_M$	1.0(f)	1.0(f)	$0.94^{+0.11}_{-0.07}$	1.0(f)	1.0(f)
FWHM [Fe K $\alpha$ , Fe K $\beta$ ] (km s $^{-1}$ )	< 1215(f)	< 1215(f)	< 1215(f)	100(f)	100(f)
$I_{\text{Fe K}\alpha}$ ( $10^{-5}$ photons cm $^{-2}$ s $^{-1}$ )	3.17	3.18	...	1.83	...
EW <sub>Fe K<math>\alpha</math></sub> (eV)	730	749	...	367	...
$E_{\text{Fe XXV}}$ (keV)	$6.686^{+0.014}_{-0.016}$	$6.686^{+0.014}_{-0.016}$	$6.680^{+0.015}_{-0.012}$	6.700(f)	6.700(f)
FWHM [Fe XXV] (km s $^{-1}$ )	$4950^{+2735}_{-2535}$	$4950^{+2735}_{-2535}$	< 6025(f)	4950(f)	4950(f)
$I_{\text{Fe XXV}}$ ( $10^{-5}$ photons cm $^{-2}$ s $^{-1}$ )	$0.98^{+0.26}_{-0.29}$	$0.98^{+0.26}_{-0.30}$	$0.88^{+0.20}_{-0.26}$	$1.7^{+1.3}_{-1.3}$	< 2.2
EW <sub>Fe XXV</sub> (eV)	$200^{+53}_{-51}$	$245^{+65}_{-65}$	$215^{+49}_{-64}$	$240^{+120}_{-180}$	< 249
$E_{\text{Ni K}\alpha}$ (keV)	$7.434^{+0.066}_{-0.041}$	$7.434^{+0.066}_{-0.041}$	$7.450^{+0.048}_{-0.073}$	7.472(f)	7.472(f)
FWHM [Ni K $\alpha$ ] (km s $^{-1}$ )	< 7410(f)	< 7410(f)	< 8600(f)	...	...
$I_{\text{Ni K}\alpha}$ ( $10^{-5}$ photons cm $^{-2}$ s $^{-1}$ )	< 0.45	< 0.45	< 0.41	< 0.88	< 0.46
EW <sub>Ni K<math>\alpha</math></sub> (eV)	< 150	< 150	< 140	< 252	< 115
$10^3 f_s$ (optically-thin scattered fraction)	$7.9^{+1.1}_{-0.5}$	$7.3^{+1.7}_{-0.7}$	$38.5^{+3.2}_{-2.2}$	$0.61^{+0.99}_{-0.47}$	$20.5^{+1.4}_{-5.8}$
$N_{H1}$ ( $10^{21}$ cm $^{-2}$ )	$2.8^{+0.7}_{-0.9}$	$2.6^{+0.8}_{-0.9}$	$2.3^{+0.7}_{-1.2}$	$13.0^{+8.5}_{-6.6}$	$7.6^{+4.2}_{-4.2}$
$A_{\text{apec}}$ ( $10^{-3}$ phot. cm $^{-2}$ s $^{-1}$ keV $^{-1}$ )	$1.8^{+0.6}_{-0.6}$	$1.7^{+0.6}_{-0.6}$	$1.8^{+0.6}_{-0.6}$	1.7(f)	1.7(f)
$kT_{\text{apec}}$ (keV)	$0.260^{+0.046}_{-0.035}$	$0.260^{+0.046}_{-0.035}$	$0.260^{+0.048}_{-0.038}$	0.260(f)	0.260(f)
$N_{H2}$ ( $10^{21}$ cm $^{-2}$ )	$3.8^{+1.1}_{-0.3}$	$3.8^{+1.0}_{-0.3}$	$3.8^{+1.0}_{-0.2}$	3.8(f)	3.8(f)
$L_{\text{APEC}}$ [Intrinsic] ( $10^{40}$ erg s $^{-1}$ )	2.9	2.9	2.9	...	...
$F_{\text{obs}}[0.7-2 \text{ keV}]$ ( $10^{-11}$ erg cm $^{-2}$ s $^{-1}$ )	0.08	0.08	0.08	...	...
$F_{\text{obs}}[2-10 \text{ keV}]$ ( $10^{-11}$ erg cm $^{-2}$ s $^{-1}$ )	0.39	0.39	0.39	0.48	0.49
$F_{\text{obs}}[10-100 \text{ keV}]$ ( $10^{-11}$ erg cm $^{-2}$ s $^{-1}$ )	30.0	27.6	31.1	34.7	34.5
$F_{\text{obs}}[14-195 \text{ keV}]$ ( $10^{-11}$ erg cm $^{-2}$ s $^{-1}$ )	45.8	38.7	49.3	47.5	46.7
$L_{\text{obs}}[0.7-2 \text{ keV}]$ ( $10^{42}$ erg s $^{-1}$ )	0.0058	0.0058	0.0058	...	...
$L_{\text{obs}}[2-10 \text{ keV}]$ ( $10^{42}$ erg s $^{-1}$ )	0.030	0.030	0.030	0.037	0.038
$L_{\text{obs}}[10-100 \text{ keV}]$ ( $10^{42}$ erg s $^{-1}$ )	2.3	2.1	2.4	2.7	2.7
$L_{\text{obs}}[14-195 \text{ keV}]$ ( $10^{42}$ erg s $^{-1}$ )	3.5	3.0	3.8	3.7	3.6

Spectral-fitting results obtained from fitting the NGC 4945 *Suzaku* and *BeppoSAX* data with various coupled models of the Compton-thick X-ray reprocessor, as described in §6. A parameter value that is followed by “(f)” indicates that the parameter was fixed during the fitting but the statistical errors were obtained by allowing the fixed parameter to be free only for obtaining the statistical errors. The FWHM values of the Fe K $\alpha$ , Fe K $\beta$ , and Ni K $\alpha$  lines were fixed at 100 km s $^{-1}$  during the fitting. The  $\Delta\chi^2$  criterion used for these fixed parameters, and for the GIS:XIS normalization ratio, was 2.706, corresponding to 90% confidence for interesting parameter. The statistical errors for the remaining free parameters used a  $\Delta\chi^2$  criterion shown in the appropriate column of the table. No statistical errors are given for the Fe K $\alpha$  line flux and EW because these emission-line parameters are determined completely by the other parameters of the MYTORUS model (but see §6 for an estimate of the statistical errors). The continuum fluxes ( $F_{\text{obs}}$ ) and luminosities ( $L_{\text{obs}}$ ) are all observed values and uncorrected for absorption and Compton scattering.



Fig. 4, and found that  $kT = 50$  keV gave the best fit for the *Suzaku* data. The parameter  $kT$  was then allowed to be free, although strictly speaking it is only correct to do this for the zeroth-order continuum. However, the statistical error obtained in this way is sufficiently small ( $kT = 50 \pm 4$  keV), that the procedure is justified in the present application. Interestingly, the *Swift* BAT spectrum, which is averaged over 58 months, gave a consistent value of  $kT = 51^{+16}_{-17}$  keV for the MYTORUS coupled model fit (Table 4). However, the statistical errors are larger so should be regarded as only approximate. For the *BeppoSAX* data we found that fits with  $kT$  in the range 50–100 keV yielded insignificant differences in the best-fitting values of  $\chi^2$ . In order to get stable fits,  $kT$  had to be frozen, so we performed fits for  $kT$  fixed at 50, 80, 100 keV. For the sake of brevity, the full set of parameters and statistical errors are given in Table 5 only for the fit with  $kT = 80$  keV, but parameter values and luminosities for the broader range of  $kT$  will be given where appropriate. The plasma optical depth,  $\tau$ , is  $\sim 1$ –1.2 for the *Suzaku* and *Swift* BAT data, and  $\sim 0.3$  for the *BeppoSAX* data.

The percentage of the intrinsic continuum scattered into the line of sight by optically-thin circumnuclear material is highly model-dependent because the luminosity of the intrinsic continuum is highly model-dependent. However, models with similar intrinsic luminosities will give similar values of  $f_s$  as is the case for the two models shown in Table 5 for the *Suzaku* data ( $\sim 7 - 8 \times 10^{-3}$ ). Both of these models are dominated by the Compton-scattered continuum so they have similar intrinsic continuum luminosities. On, the other hand, for the *BeppoSAX* data we get values of  $f_s$  of  $6.1 \times 10^{-4}$  and  $2 \times 10^{-2}$  for the MYTORUS and spherical models respectively. The spherical model applied to the *Suzaku* data gives the highest value of  $f_s \sim 3.9 \times 10^{-2}$ . The smallest and largest values differ by nearly a factor of 64 because the MYTORUS fit to the *BeppoSAX* data is dominated by the zeroth order continuum, whereas the spherical fit is dominated by the Compton-scattered continuum (see discussion in §6).

The column density associated with the optically-thin scattering region ( $N_{H1}$ ) is  $\sim 2$ – $3 \times 10^{21}$  cm $^{-2}$  for the *Suzaku* fits, and  $\sim 7 - 13 \times 10^{21}$  cm $^{-2}$  for the *BeppoSAX* fits.

### 6.5.2 Column Density of the X-ray Reprocessor

The toroidal equatorial column density for the coupled MYTORUS fit to the *Suzaku* data with a power-law intrinsic continuum is  $N_H = 3.49^{+0.19}_{-0.17} \times 10^{24}$  cm $^{-2}$ . The MYTORUS *Suzaku* fit with a Comptonized thermal intrinsic continuum gave a consistent value of  $N_H$  (see Table 5). On the other hand, the column density for the *BeppoSAX* fit with the coupled MYTORUS model is somewhat higher than the values from the *Suzaku* fits, at  $N_H = 4.55^{+1.38}_{-0.80} \times 10^{24}$  cm $^{-2}$ . What is also important is that the column density obtained from the spherical (BN11) model fitted to the *BeppoSAX* data is significantly less than that from the MYTORUS fit, at  $3.06^{+0.33}_{-0.34} \times 10^{24}$  cm $^{-2}$ . This value is also less than that obtained from the *Suzaku* MYTORUS fits. However, the spherical model fitted to the *Suzaku* data gave the lowest column density out of all the spectral fits ( $N_H = 2.17^{+0.18}_{-0.15} \times 10^{24}$  cm $^{-2}$ ). The reason for the very different values of  $N_H$  for the spherical fits compared to the MYTORUS fit to the *BeppoSAX* spectra is that the latter is dominated by the zeroth-order continuum, but in the spherical model fits the spectrum is dominated by the Compton-scattered continuum.

From Table 4, which shows results from spectral fitting to the 58-month time-averaged *Swift* BAT spectrum, we see that the coupled MYTORUS model fits gave values of  $N_H$  that are statistically consistent with those obtained from the *Suzaku* and *BeppoSAX* fits, since the statistical errors on the *Swift* BAT and *BeppoSAX* values are large. The spherical model fit gave a lower value of  $N_H$  than the MYTORUS fits, as would be expected ( $2.74^{+0.27}_{-0.25} \times 10^{24}$  cm $^{-2}$ ), and this value is statistically consistent with that obtained from the spherical model fitted to the *BeppoSAX* data.

### 6.5.3 Inclination Angle

In all of the spectral fits to the *Suzaku* and *BeppoSAX* data with the coupled MYTORUS model, the orientation of the X-ray reprocessor is very tightly constrained to be edge-on, or nearly edge-on (see Table 5). The inclination angle is not less than  $84^\circ$  in any of the spectral fits to the *Suzaku* and *BeppoSAX* data, even accounting for the statistical errors (which are small). The physical driver behind this is that the observer's view of the inner surface of the reprocessor will give an Fe K $\alpha$  line flux that is too large if the inclination angle is too small, whilst at the same time the column density (which also affects the Fe K $\alpha$  line flux) cannot be too small because the Compton hump must be prominent enough to fit the high-energy ( $> 10$  keV) part of the spectrum. In fact, we can see that for the *BeppoSAX* MYTORUS fit, the inclination angle is driven fully to an edge-on orientation, and the parameter  $A_S$  is driven down to  $\sim 0.1$  in order to keep the Fe K $\alpha$  line flux in check.

### 6.5.4 Fe K $\alpha$ Line Flux and Equivalent Width

The Fe K $\alpha$  line flux is not explicitly an adjustable parameter because the line is produced self-consistently in all of the Compton-thick reprocessor models that we applied. However, by subtracting the continuum-only flux in the 5–7 keV band measured from the best-fitting model (by temporarily setting  $A_L = 0$ ), from the total flux in the same band measured with  $A_S = A_L$ , we can estimate the Fe K $\alpha$  line flux. In this way we obtained  $3.2 \times 10^{-5}$  photons cm $^{-2}$  s $^{-1}$  for both of the MYTORUS

fits to the *Suzaku* data and an EW of 730 eV (see Table 5). Note that the Fe K $\alpha$  line flux and EW include both the zeroth-order and the Compton shoulder components of the Fe K $\alpha$  line. The Fe K $\alpha$  line is not separable from the continuum in the BN11 models so we could not obtain Fe K $\alpha$  line flux measurements for these models.

The statistical errors on the Fe K $\alpha$  line flux cannot be obtained in the usual way. However, in the MYTORUS fits the parameter  $A_L$  can be temporarily “untied” from  $A_S$  in order to crudely estimate the statistical errors on the line flux. By perturbing  $A_L$  either side of the best-fitting value we estimated that the 90% confidence, one-parameter statistical error on the Fe K $\alpha$  line flux is of the order of 5% for the *Suzaku* fits. This is also a reasonable, rough estimate on the statistical error on the EW. An empirical, Gaussian fit to the Fe K $\alpha$  emission line is in agreement with these estimates (e.g., see Itoh et al. 2008).

A similar procedure applied to the *BeppoSAX* MYTORUS spectral fit (see Table 5) yielded  $1.8 \times 10^{-5}$  photons cm $^{-2}$  s $^{-1}$  (EW  $\sim$  370 eV), with an estimated, 90% confidence, one-parameter statistical error of  $\sim$  35%. However, because of the poor spectral resolution of the *BeppoSAX* MECS, there is considerable blending of the 6.4 keV and 6.7 keV lines. We found that empirically fitting the MECS data with a simple power-law and two narrow Gaussian emission lines returned a flux for the 6.4 keV line of  $2.5^{+0.7}_{-0.7} \times 10^{-5}$  photons cm $^{-2}$  s $^{-1}$ , statistically consistent with the Fe K $\alpha$  line flux from the *Suzaku* spectral fits. In the interest of general analysis, we point out that the Fe K $\alpha$  line parameters obtained from the *BeppoSAX* spectral fit in Table 5 are not sensitive to  $kT$ . Specifically, for fits with  $kT$  in the range 50 to 100 keV, the line flux only varied between  $\sim 1.7 \times 10^{-5}$  and  $\sim 1.9 \times 10^{-5}$  photons cm $^{-2}$  s $^{-1}$ .

#### 6.5.5 The Line Emission at 6.7 keV

The line emission in the *Suzaku* data centered at  $\sim$  6.67–6.70 keV (see Table 5) is consistent with an identification of the Fe xxv He-like triplet, but the individual members of the triplet cannot be resolved with the spectral resolution of CCDs. The peak energy of the unresolved He-like triplet depends on the relative fluxes in the forbidden, intercombination, and resonant components of the triplet, at expected energies of 6.637, 6.675, and 6.700 keV<sup>9</sup>. As well as members of the triplet, the line emission profile between the peak energies of the Fe K $\alpha$  and Fe K $\beta$  lines could have a contribution from intermediate ionic species of Fe as well. These factors mean that the intrinsic width of the line shown in Table 5 should not be interpreted as purely a velocity width, since some of the broadening could be due to the presence of several line components. In fact, we found that the overall line complex is unresolved at a confidence level of 90% for two parameters.

The *BeppoSAX* data have a factor of 4 worse spectral resolution than the *Suzaku* data so we had to fix the centroid of the line emission at 6.7 keV, and the intrinsic line width at the value from the *Suzaku* fits. The problem of the blending of the 6.4 keV and 6.7 keV line emission in the *BeppoSAX* MECS data has already been discussed above (§6.5.4).

#### 6.5.6 The Ni K $\alpha$ Line

From Table 5, it can be seen that the Ni K $\alpha$  line energy measured from the *Suzaku* data, namely  $7.434^{+0.066}_{-0.041}$  keV, is consistent with the theoretical value of 7.472 keV (e.g., Bearden 1967). The Ni K $\alpha$  line fluxes in Table 5 have lower limits that are zero, but the 11 and 12-parameter, 68% confidence statistical errors are likely to be too conservative (since the Ni K $\alpha$  line is a relatively isolated, narrow feature). Using instead, a one-parameter, 90% confidence criterion for the statistical errors, we obtained a Ni K $\alpha$  line flux of  $2.0^{+1.2}_{-1.2} \times 10^{-6}$  photons cm $^{-2}$  s $^{-1}$  from the MYTORUS fits. The EW corresponding to these line flux measurements and errors is  $46 \pm 28$  eV, somewhat less than the calculated Monte Carlo value (see Yaqoob & Murphy 2011b), but the difference is less than the uncertainty in the cosmic Ni abundance. We tried letting the intrinsic width of the Ni K $\alpha$  line component float in the *Suzaku* fits but found that the line is unresolved, obtaining only a loose upper limit on the width of  $\sim$  7410 km s $^{-1}$  FWHM for the MYTORUS fits (for 90% confidence, one interesting parameter). Due to the weakness of the Ni K $\alpha$  line and the poor spectral resolution of the *BeppoSAX* data, we did not obtain upper limits on the intrinsic width of the line for the *BeppoSAX* data. Note that the BN11 spherical model already includes Ni K $\alpha$  line emission so the Ni K $\alpha$  line parameters shown in Table 5 for the spherical model fits correspond to additional line emission, which was included to allow for the considerable uncertainty in the Ni cosmic abundance (e.g., see discussion in MY09).

## 7 SPECTRAL FITS WITH DECOUPLED REPROCESSOR MODELS

### 7.1 Decoupled Model Setup

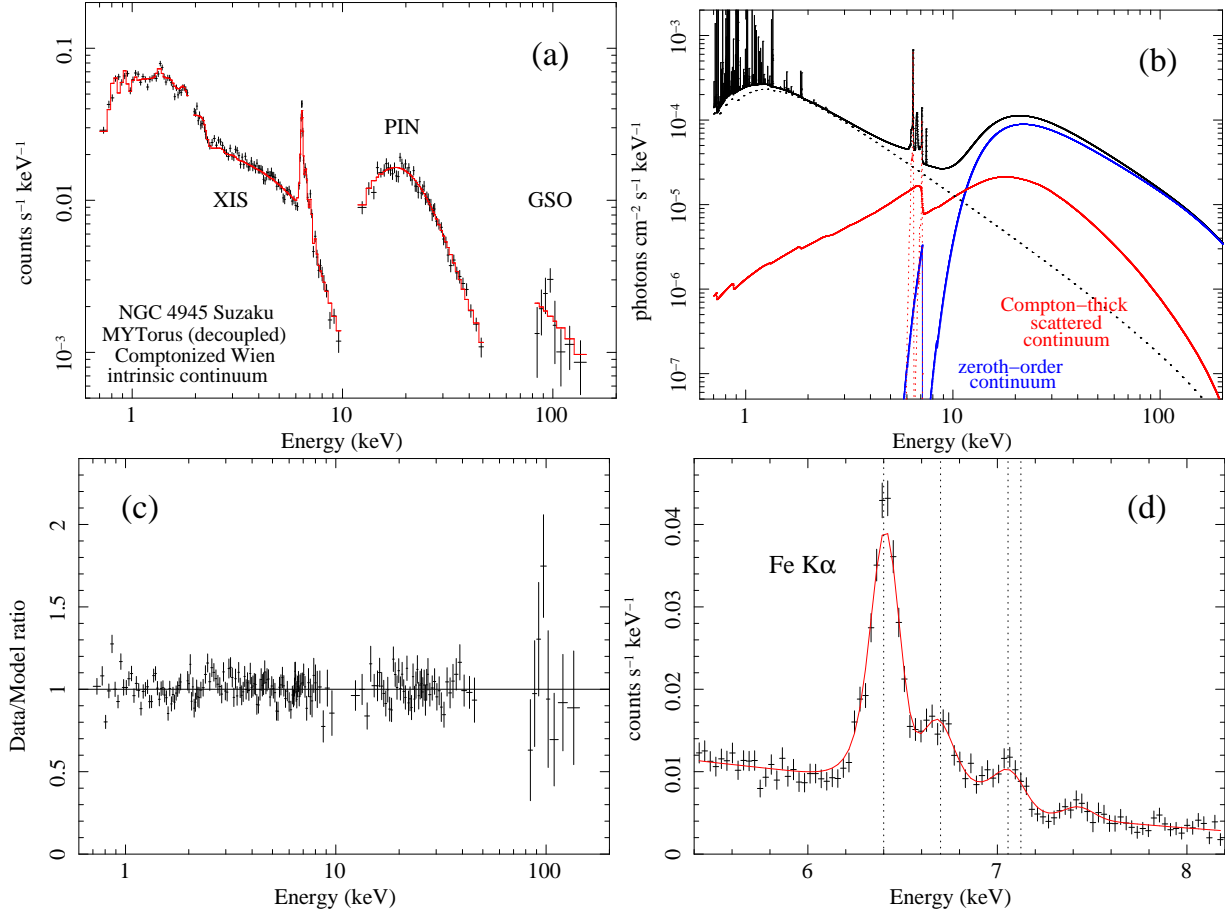
In §4.5.2 we described the motivation for applying a Compton-thick reprocessor model in which the zeroth-order continuum and the Compton-scattered continuum are decoupled. In this section we apply such a “decoupled” MYTORUS model, in

<sup>9</sup> NIST, <http://physics.nist.gov/PhysRefData/>

**Table 6.** NGC 4945 Spectral-Fitting Results with the Decoupled MYTORUS Model

Parameter	<i>Suzaku</i>	<i>Suzaku</i>	<i>Suzaku</i>	<i>Suzaku</i>	<i>BeppoSAX</i>	<i>BeppoSAX</i>
	XIS	XIS	XIS	XIS		
	PIN	PIN	PIN	PIN		
	GSO		GSO			
Free Parameters	12	11	12	11	8	8
Interesting Parameters	10	10	10	10	7	7
$\chi^2$	444.1	433.4	447.1	437.7	85.8	81.4
degrees of freedom	355	348	355	348	70	70
Reduced $\chi^2$	1.25	1.25	1.26	1.26	1.23	1.16
Null probability	$8.9 \times 10^{-4}$	$1.2 \times 10^{-2}$	$6.4 \times 10^{-4}$	$7.5 \times 10^{-4}$	$9.6 \times 10^{-2}$	0.167
$\Delta\chi^2$ criterion (68% confidence)	11.50	11.50	11.50	11.50	8.15	8.15
PIN:XIS normalization	1.12 (f)	1.12 (f)	1.12 (f)	1.12 (f)	...	...
GSO:XIS normalization	$0.73^{+0.15}_{-0.14}$	...	$0.45^{+0.08}_{-0.09}$	...	...	...
$kT$	22 keV	22 keV	50 keV	50 keV	50 keV	100 keV
$\tau$	$2.09^{+0.08}_{-0.09}$	$2.08^{+0.09}_{-0.08}$	$0.95^{+0.04}_{-0.06}$	$0.95^{+0.04}_{-0.06}$	$0.50^{+0.12}_{-0.38}$	$0.15^{+0.05}_{-0.06}$
$N_H$ ( $10^{24}$ cm $^{-2}$ )	$4.00^{+0.10}_{-0.07}$	$4.00^{+0.10}_{-0.07}$	$4.21^{+0.07}_{-0.07}$	$4.21^{+0.07}_{-0.07}$	$4.76^{+1.06}_{-0.80}$	$4.94^{+0.98}_{-0.83}$
$10^2 A_{S90}$ ( $= A_{L90}$ )	$5.2^{+3.8}_{-3.3}$ (f)	$5.2^{+3.9}_{-3.2}$ (f)	< 3.4 (f)	< 3.4 (f)	< 23(f)	< 23(f)
$10^2 A_{S00}$ ( $= A_{L00}$ )	$1.67^{+0.19}_{-0.17}$	$1.67^{+0.18}_{-0.11}$	$1.39^{+0.13}_{-0.12}$	$1.40^{+0.12}_{-0.12}$	$0.21^{+0.28}_{-0.13}$	$0.18^{+0.24}_{-0.11}$
$10^3 f_s$ (optically-thin scattered fraction)	$1.50^{+0.18}_{-0.10}$	$1.50^{+0.18}_{-0.10}$	$0.94^{+0.05}_{-0.05}$	$0.94^{+0.05}_{-0.05}$	$0.29^{+0.43}_{-0.21}$	$0.20^{+0.34}_{-0.13}$
$N_{H1}$ ( $10^{21}$ cm $^{-2}$ )	$3.0^{+0.6}_{-0.8}$	$3.0^{+0.6}_{-0.8}$	$3.1^{+0.7}_{-0.8}$	$3.2^{+0.6}_{-0.9}$	$12.9^{+7.5}_{-6.7}$	$16.2^{+7.7}_{-6.9}$
FWHM [Fe K $\alpha$ , Fe K $\beta$ ] (km s $^{-1}$ )	< 1235 (f)	< 1235 (f)	< 1235 (f)	< 1235 (f)	100(f)	100(f)
$I_{\text{Fe K}\alpha}$ ( $10^{-5}$ photons cm $^{-2}$ s $^{-1}$ )	3.11	3.11	3.09	3.09	1.77	1.95
EW <sub>Fe K<math>\alpha</math></sub> (eV)	708	708	704	704	341	376
$E_{\text{Fe XXV}}$ (keV)	$6.687^{+0.015}_{-0.014}$	$6.687^{+0.015}_{-0.014}$	$6.687^{+0.015}_{-0.014}$	$6.687^{+0.015}_{-0.014}$	6.700(f)	6.700(f)
FWHM [Fe xxv] (km s $^{-1}$ )	$4970^{+2320}_{-3070}$	$4970^{+2320}_{-3070}$	$4970^{+2210}_{-3385}$	$4970^{+2210}_{-3385}$	4970(f)	4970(f)
$I_{\text{Fe XXV}}$ ( $10^{-5}$ photons cm $^{-2}$ s $^{-1}$ )	$0.96^{+0.24}_{-0.24}$	$0.96^{+0.24}_{-0.24}$	$0.94^{+0.24}_{-0.24}$	$0.94^{+0.24}_{-0.24}$	$1.6^{+1.3}_{-1.3}$	$1.5^{+1.4}_{-1.3}$
EW <sub>Fe XXV</sub> (eV)	$219^{+55}_{-55}$	$219^{+55}_{-55}$	$214^{+55}_{-55}$	$214^{+55}_{-55}$	$320^{+260}_{-260}$	$305^{+285}_{-265}$
$E_{\text{Ni K}\alpha}$ (keV)	$7.434^{+0.057}_{-0.042}$	$7.434^{+0.057}_{-0.042}$	$7.434^{+0.057}_{-0.042}$	$7.434^{+0.057}_{-0.042}$	7.472(f)	7.472(f)
FWHM [Ni K $\alpha$ ] (km s $^{-1}$ )	< 7285(f)	< 7305(f)	< 7285(f)	< 7330(f)	100(f)	100(f)
$I_{\text{Ni K}\alpha}$ ( $10^{-5}$ photons cm $^{-2}$ s $^{-1}$ )	< 0.43	< 0.43	< 0.43	< 0.43	< 0.86	< 0.98
EW <sub>Ni K<math>\alpha</math></sub> (eV)	< 146	< 146	< 146	< 146	< 261	< 307
$N_{H2}$ ( $10^{21}$ cm $^{-2}$ )	$3.8^{+0.7}_{-0.3}$	$3.8^{+0.7}_{-0.3}$	$3.8^{+0.5}_{-0.4}$	$3.8^{+0.5}_{-0.4}$	3.8(f)	3.8(f)
$A_{\text{apex}}$ ( $10^{-3}$ phot. cm $^{-2}$ s $^{-1}$ keV $^{-1}$ )	$1.77^{+0.60}_{-0.55}$	$1.77^{+0.60}_{-0.55}$	$1.77^{+0.63}_{-0.59}$	$1.77^{+0.56}_{-0.55}$	1.77(f)	1.77(f)
$kT_{\text{apex}}$ (keV)	$0.260^{+0.046}_{-0.035}$	$0.260^{+0.046}_{-0.035}$	$0.260^{+0.046}_{-0.035}$	$0.260^{+0.046}_{-0.035}$	0.260(f)	0.260(f)
$L_{\text{apex}}$ [Intrinsic] ( $10^{40}$ erg s $^{-1}$ )	2.9	2.9	2.9	2.9	...	...
$F_{\text{obs}}[0.7-2 \text{ keV}]$ ( $10^{-11}$ erg cm $^{-2}$ s $^{-1}$ )	0.075	0.075	0.075	0.075	...	...
$F_{\text{obs}}[2-10 \text{ keV}]$ ( $10^{-11}$ erg cm $^{-2}$ s $^{-1}$ )	0.39	0.39	0.39	0.39	0.48	0.48
$F_{\text{obs}}[10-100 \text{ keV}]$ ( $10^{-11}$ erg cm $^{-2}$ s $^{-1}$ )	26.5	26.5	29.2	29.2	34.7	34.7
$F_{\text{obs}}[14-195 \text{ keV}]$ ( $10^{-11}$ erg cm $^{-2}$ s $^{-1}$ )	31.8	31.8	45.2	45.2	46.2	47.8
$L_{\text{obs}}[0.7-2 \text{ keV}]$ ( $10^{42}$ erg s $^{-1}$ )	0.0057	0.0058	0.0058	0.0058	...	...
$L_{\text{obs}}[2-10 \text{ keV}]$ ( $10^{42}$ erg s $^{-1}$ )	0.030	0.030	0.030	0.030	0.032	0.037
$L_{\text{obs}}[10-100 \text{ keV}]$ ( $10^{42}$ erg s $^{-1}$ )	2.0	2.0	2.3	2.3	2.7	2.7
$L_{\text{obs}}[14-195 \text{ keV}]$ ( $10^{42}$ erg s $^{-1}$ )	2.5	2.5	3.5	3.5	3.6	3.7

Spectral-fitting results obtained from fitting the NGC 4945 *Suzaku* and *BeppoSAX* data with the decoupled MYTORUS model, using a thermally Comptonized incident intrinsic continuum, as described in §4.5.2 and §7. The first two columns for the *Suzaku* fits compare the same model (in which  $kT = 22$  keV) with and without the GSO, as indicated. The second pair of columns for the *Suzaku* fits compare a model with  $kT = 50$  keV, with and without the GSO. The parameters of the model are also summarized in Table 3. A parameter value that is followed by “(f)” indicates that the parameter was fixed during the fitting but the statistical errors were obtained by allowing the fixed parameter to be free only for obtaining the statistical errors. The FWHM values of the Fe K $\alpha$ , Fe K $\beta$ , and Ni K $\alpha$  lines were fixed at 100 km s $^{-1}$  during the fitting. The  $A_{S90}$  parameter was fixed at the best-fitting value, as indicated (zero if only an upper limit is shown). The  $\Delta\chi^2$  criterion used for these fixed parameters, except for  $A_{S90}$ , was 2.706, corresponding to 90% confidence for one interesting parameter. The  $\Delta\chi^2$  criterion used for  $A_{S90}$  was 12.60 for the *Suzaku* fits (corresponding to 68% confidence for 11 interesting parameters), and 9.27 for the *BeppoSAX* fits (corresponding to 68% confidence for 8 interesting parameters). The statistical errors for the remaining free parameters are shown in the appropriate column in the table. No statistical errors are given for the Fe K $\alpha$  line flux and EW because these emission-line parameters are determined completely by the other parameters of the MYTORUS model (but see §6 for estimates). The continuum fluxes ( $F_{\text{obs}}$ ) and luminosities ( $L_{\text{obs}}$ ) are all observed values and uncorrected for absorption or other reprocessing effects.



**Figure 11.** Results of spectral fitting to the NGC 4945 *Suzaku* data with the toroidal X-ray reprocessor model, MYTORUS, with the Compton-scattered and zeroth-order continua decoupled (mimicking a patchy reprocessor). Unlike the coupled model fit shown in Fig. 7, the fit shown here has the zeroth-order continuum dominating over the scattered continuum above  $\sim 10$  keV. The incident, intrinsic continuum for the model fit shown here has a thermally Comptonized spectrum with  $kT = 50$  keV (see Table 3 and §7 for details). (a) The counts spectra overlaid with the folded best-fitting model. The three data groups from left to right correspond to data from the XIS, HXD/PIN, and the HXD/GSO. The data from XIS0, 1, 2, and 3 are combined into a single spectrum. For clarity, the data in some energy ranges is binned more coarsely than the binning used for the actual spectral fitting. (b) The best-fitting model photon spectrum. In addition to the total spectrum (solid, black), some of the individual model components are also shown. The dotted curve is the optically-thin scattered component, the blue curve is the zeroth-order continuum, and the red curve is the Compton-thick scattered component. (c) The ratios of the data to the best-fitting model. (d) A close-up zoom of the Fe K region in panel (a). From left to right, the dotted lines correspond to the energies of Fe I  $K\alpha$ , Fe XXV (r), Fe I  $K\beta$ , and the neutral Fe K edge. The bump above the Fe K edge is the Ni  $K\alpha$  line.

which the Compton-scattered continuum is composed of a face-on and an edge-on component, each of which can be varied independently of the zeroth-order continuum. As explained in §4.5.2 this setup can mimic a clumpy, patchy structure (not necessarily with a toroidal geometry), in which a back-reflected, unobscured reflection spectrum is able to dominate over the “transmitted” reflection spectrum (see Fig. 2). In our analysis of NGC 4945, except when otherwise explicitly stated, coupling between the global and line-of-sight column density was maintained (i.e.,  $N_{H,S} = N_{H,Z} \equiv N_H$ ).

As stated earlier, using the MYTORUS model in a decoupled mode most closely resembles *ad hoc* models that use a disk-reflection component combined with line-of-sight obscuration, so the decoupled fits will indicate how the disk-reflection models relate to the broader set of spectral solutions that we have addressed in the present paper (e.g., see discussion in Yaqoob & Murphy 2011b).

The model was set up as described in §4.5.2, with a Comptonized thermal spectrum for the intrinsic input continuum. Preliminary fitting showed that  $kT$  is poorly constrained, so for each data set, fits with two representative values of  $kT$  were performed since tables with fixed values of  $kT$  had to be used. Using the  $N_H$  versus  $kT$  confidence contours as a guide, we performed fits for  $kT = 22$  keV and 50 keV for the *Suzaku* data, and  $kT = 50$  keV and 100 keV for the *BeppoSAX* data. Some of the parameters in the *BeppoSAX* models were frozen as in the coupled fits (see §6 for details). We did not apply the decoupled MYTORUS model to the *Swift* BAT spectrum because there were too many free model parameters.

## 7.2 Suzaku Results with the Decoupled Model

Since the present paper outlines the first detailed methodology for applying the MYTORUS model, we take this opportunity to assess the effect of including or not including the GSO data in the spectral fitting. We show these results for the decoupled models as opposed to the coupled models because there are more free parameters in the former than the latter. NGC 4945 is amongst the brightest AGNs in the GSO bandpass, but for most AGNs, the GSO data will be unusable due to excessive background-subtraction systematics. We can use the NGC 4945 data to assess the impact on the derived key physical parameters when the spectral fits are performed with XIS and PIN data only, by comparing the results from the full-band, three-instrument fits. Thus, a total of four fits were performed on the *Suzaku* data, and the results are shown in Table 6. For the three-instrument fit with  $kT = 22$  keV, the folded model and counts spectra are shown in Fig. 11(a). The best-fitting photon spectrum is shown in Fig. 11(b), and the data/model ratios are shown in Fig. 11(c). It can be seen that an excellent fit is obtained, in the 1–50 keV range, with larger residuals apparent outside of this energy range. Figure 11(d) shows a zoomed view of the Fe K region. As with the coupled MYTORUS model, a good fit to the Fe K $\alpha$  and Fe K $\beta$  lines is obtained, and the Fe K edge region is also well-modeled. We see from Figure 11(b) that in this model the zeroth-order continuum dominates over the Compton-scattered continuum (above 10 keV), in contrast to the coupled model shown in Figure 7(b), for which the converse is true. The decoupled model with  $kT = 50$  keV is also dominated by the zeroth-order continuum above 10 keV.

Formally, the best-fitting  $\chi^2$  values and the associated null hypothesis probabilities show that the fits should be statistically rejected at greater than 98.8% confidence, but we point out that the residuals are not entirely statistical in origin. There are complex, energy-dependent residuals due to the limitations of instrument calibration and despite that, the overall residuals in the *Suzaku* 1–50 keV band are flat and less than  $\sim 20\%$  for the *Suzaku* data. Below  $\sim 1$  keV, the optically-thin thermal line spectrum is likely to be much more complex than the APEC model we have used, and we have also not accounted for contamination by numerous weak and unresolved X-ray point sources (see Itoh et al. 2008, and references therein).

### 7.2.1 Comparison of the Suzaku Results with and without the GSO Data

If we compare the first pair of columns of results in Table 6 with each other, and do the same for the second pair of columns, we see that omitting the GSO data has a negligible effect on the best-fitting model parameters and their statistical errors. In fact, for most parameters, the results are identical for fits with and without the GSO, and this is true for both values of  $kT$ . This outcome is encouraging because it means that a spectral-fitting analysis of *Suzaku* data of AGN (the majority of which do not have useable GSO data) will not be impacted using the XIS and PIN data only. Nevertheless, for NGC 4945 we refer to the results obtained from the three-instrument fits in the remainder of the paper. We see from Table 6 that the data cannot distinguish between the  $kT = 22$  keV and  $kT = 50$  keV models since the difference between the two best-fitting  $\chi^2$  values is only 3.0, which, considering the complexity of the data and the models, is negligible and insignificant. However, we note that the ratio of the GSO to XIS normalizations is very different for the two solutions (see Table 6). This ratio is  $0.73^{+0.15}_{-0.14}$  and  $0.45^{+0.08}_{-0.09}$  for  $kT = 22$  keV and  $kT = 50$  keV respectively. The higher value of the ratio is more in line with the corresponding ratio obtained for 3C 273 (see appendix), but the solution with the lower value cannot be ruled out because of the background-subtraction systematics. We also see that the differences between the best-fitting  $\chi^2$  values for the coupled *Suzaku* MYTORUS fits in Table 5 and the decoupled *Suzaku* MYTORUS fits is not significant enough to determine whether the coupled or decoupled MYTORUS spectral fits can be ruled out (without additional, independent information such as variability properties).

## 7.3 BeppoSAX Results with the Decoupled Model

The *BeppoSAX* counts spectra, best-fitting folded model, and the data/model residuals for the decoupled MYTORUS spectral fit with  $kT = 50$  keV are shown in Fig. 9(b). The fit is excellent across the entire bandpass, comparable to the fit with the BN11 spherical model and not statistically better or worse. The decoupled MYTORUS fit with  $kT = 100$  keV has a lower best-fitting  $\chi^2$  value, but again, the difference is not statistically significant.

## 7.4 Overall Assessment of the Parameters Derived with Decoupled Models

### 7.4.1 Effect of Comptonizing Plasma Temperature on the Plasma Optical Depth

We examined the effect of the Comptonizing plasma temperature,  $kT$ , on the spectral-fitting results, since this temperature had to be fixed for each fit. The largest effect of using different values of  $kT$  is on the optical depth of the Comptonizing plasma,  $\tau$ , and this is to be expected, because the steepness of the intrinsic X-ray continuum (below the high-energy roll-over) is determined by the Compton- $y$  parameter, which involves the product  $(kT)\tau$ . The optical depth is as high as  $\sim 2$  for the *Suzaku* fit with  $kT = 22$  keV, and as low as 0.15 for the *BeppoSAX* fit with  $kT = 100$  keV.

#### 7.4.2 Column Density

The effect of different values of  $kT$  on the column density of the X-ray reprocessor,  $N_H$ , is small, only of the order of 5%. For the *Suzaku* data, the lower value of  $kT = 22$  keV gives a lower value of  $N_H$  of  $4.00^{+0.10}_{-0.07} \times 10^{24} \text{ cm}^{-2}$ , and the higher value of  $kT = 50$  keV gives a higher value of  $N_H$  of  $4.21^{+0.07}_{-0.07} \times 10^{24} \text{ cm}^{-2}$ .

The values of  $N_H$  obtained from the *BeppoSAX* data are higher (nearly  $5 \times 10^{24} \text{ cm}^{-2}$ ), but the statistical errors are of the order of 20%, so the column densities are statistically consistent with those obtained from the *Suzaku* data.

#### 7.4.3 Decoupled Column Densities

We checked whether the line-of-sight column density is required to be significantly different to the global average column density. This was done by decoupling the column density associated with the zeroth-order continuum ( $N_{H,Z}$ ) from that for the Compton-scattered continuum ( $N_{H,S}$ , associated with  $A_{S00}$  and  $A_{S90}$ ). For both the *Suzaku* and *BeppoSAX* data, the new line-of-sight column densities ( $N_{H,Z}$ ) were statistically consistent with the original values ( $N_H$ ) before the column densities were decoupled. Although the statistical errors are larger, the one-parameter, 90% errors are less than 10%. Moreover, for both the *Suzaku* and *BeppoSAX* data, the global column densities ( $N_{H,S}$ ) were statistically consistent with the corresponding line-of-sight column densities ( $N_{H,Z}$ ). In fact, the column density of the material responsible for the Compton-scattered continuum cannot be much less than  $10^{24} \text{ cm}^{-2}$  because there would be too much curvature in the resulting spectrum below 10 keV. Indeed, we obtained one-parameter lower limits at 90% confidence on  $N_{H,S}$  of  $2.6 \times 10^{24} \text{ cm}^{-2}$  for the *Suzaku* data (for  $kT = 22$  keV), and  $1.06 \times 10^{24} \text{ cm}^{-2}$  for the *BeppoSAX* data (for  $kT = 100$  keV). On the other hand, an upper limit on  $N_{H,S}$  could not be obtained, with both the *Suzaku* and *BeppoSAX* data being consistent with the highest value tested ( $10^{25} \text{ cm}^{-2}$ ).

#### 7.4.4 Compton-Scattered Continua

The parameter  $A_{S90}$ , which measures the relative magnitude of the edge-on Compton-scattering component, was  $5.2^{+3.8}_{-3.3} \times 10^{-2}$  for the *Suzaku* fit with  $kT = 22$  keV, and was consistent with 0.0 for  $kT = 50$  keV, with an upper limit of  $3.4 \times 10^{-2}$ . The *BeppoSAX* data could not constrain  $A_{S90}$ , which was consistent with zero and we obtained an upper limit of 0.23. Note that for fits to both the *Suzaku* and *BeppoSAX* data,  $A_{S90}$  was fixed at its best-fitting value during the error analysis for the other parameters but was allowed to float to estimate its statistical errors. For the relative normalizations of the back-side Compton-scattered continuum component, we obtained  $A_{S00} = 1.67^{+0.19}_{-0.17} \times 10^{-2}$  and  $A_{S00} = 1.39^{+0.13}_{-0.11} \times 10^{-2}$  for the *Suzaku* fits with  $kT = 22$  keV and  $kT = 50$  keV respectively. The difference between the two normalizations is only  $\sim 13\%$ . For the *BeppoSAX* fits,  $A_{S00}$  is a factor of  $\sim 7$  to 8 lower, at  $2.1^{+2.8}_{-1.3} \times 10^{-3}$  and  $1.8^{+2.4}_{-1.1} \times 10^{-3}$  for  $kT = 50$  keV and  $kT = 100$  keV respectively.

Note that  $A_{S90}$  and  $A_{S00}$  cannot be directly compared to each other because they are relative normalizations associated with continua that have very different shapes and magnitudes. For similar values of  $A_{S90}$  and  $A_{S00}$ , the Compton-scattered continuum associated with the former parameter is much weaker than that associated with the latter parameter (e.g., see Fig. 6). We will see in §8 that in all of the decoupled MYTORUS fits, the zeroth-order continuum dominates over the Compton-scattered continuum for both the *Suzaku* and *BeppoSAX* data.

#### 7.4.5 Optically-thin Scattered Continuum

The parameter  $f_s$ , which corresponds to the fraction of the intrinsic continuum scattered by an extended, optically-thin zone is  $1.50^{+0.18}_{-0.10} \times 10^{-3}$  and  $0.94^{+0.05}_{-0.05} \times 10^{-3}$  for the *Suzaku* fits with  $kT = 22$  keV and  $kT = 50$  keV respectively. For the *BeppoSAX* fits with  $kT = 50$  keV and  $kT = 100$  keV, we obtained much lower values of  $f_s$  of  $2.9^{+4.8}_{-2.1} \times 10^{-4}$  and  $2.0^{+3.4}_{-1.3} \times 10^{-4}$  respectively. As explained in §6, the value of  $f_s$  is highly model-dependent because it depends on the intrinsic continuum luminosity, which can differ by over an order of magnitude for different models.

#### 7.4.6 Soft X-ray Emission and Absorption Components

The remaining model parameters, namely the temperature and normalization of the soft X-ray thermal component,  $N_{H1}$ ,  $N_{H2}$ , and all of the emission-line parameters (including the Fe K $\alpha$  line fluxes) do *not* show any discernible dependence on the value of  $kT$  adopted. This is to be expected since all of the parameters mentioned are associated with the spectrum below  $\sim 10$  keV. For the same reason, these parameter values are similar to the corresponding values obtained for the coupled MYTORUS fit (see §6 and Table 5) so we do not discuss them again here.

**Table 7.** NGC 4945 Intrinsic to Observed Luminosity Ratios

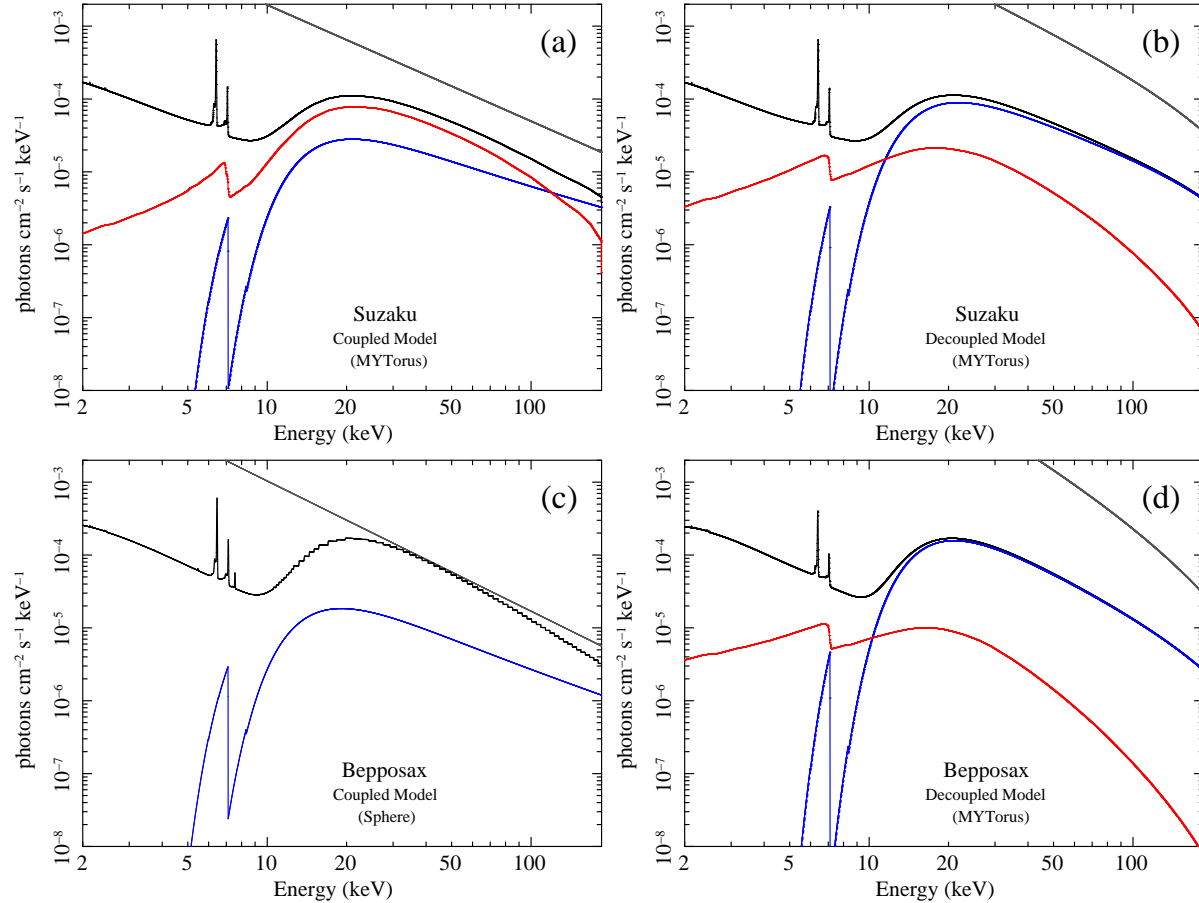
Type	Data	Model	Continuum	$kT$ (keV)	$L_{\text{intr}}/L_{\text{obs}}$ (0.7–2 keV)	$L_{\text{intr}}/L_{\text{obs}}$ (2–10 keV)	$L_{\text{intr}}/L_{\text{obs}}$ (10–100 keV)	$L_{\text{intr}}/L_{\text{obs}}$ (14–195 keV)
Zeroth-order	<i>Swift</i> BAT	MYTORUS	COMPTT	$36^{+62}_{-10}$	...	...	...	13.7
Coupled	<i>Suzaku</i>	MYTORUS	POWERLAW	...	186.2	93.4	4.0	3.7
Coupled	<i>Suzaku</i>	MYTORUS	COMPTT	$50 \pm 4$ keV	195.7	102.1	4.3	3.7
Coupled	<i>Suzaku</i>	SPHERE	POWERLAW	...	36.2	21.2	1.07	1.01
Coupled	<i>BeppoSAX</i>	MYTORUS	COMPTT	50 keV	...	1337.7	24.7	18.1
Coupled	<i>BeppoSAX</i>	MYTORUS	COMPTT	80 keV	...	1588.2	27.0	19.4
Coupled	<i>BeppoSAX</i>	MYTORUS	COMPTT	100 keV	...	1764.3	28.0	19.1
Coupled	<i>BeppoSAX</i>	SPHERE	POWERLAW	...	46.3	1.43	1.35	
Coupled	<i>Swift</i> BAT	MYTORUS	POWERLAW	...				3.8
Coupled	<i>Swift</i> BAT	MYTORUS	COMPTT	$50^{+16}_{-17}$	...	...	...	3.54
Coupled	<i>Swift</i> BAT	SPHERE	POWERLAW	...	...	...	...	1.22
Decoupled	<i>Suzaku</i>	MYTORUS	COMPTT	22 keV	1012.1	469.4	16.3	13.5
Decoupled	<i>Suzaku</i>	MYTORUS	COMPTT	50 keV	1650.0	736.0	22.0	16.0
Decoupled	<i>BeppoSAX</i>	MYTORUS	COMPTT	50 keV	...	3122.2	44.1	30.6
Decoupled	<i>BeppoSAX</i>	MYTORUS	COMPTT	100 keV	...	4534.0	51.9	34.4

The ratios of intrinsic ( $L_{\text{intr}}$ ) to observed ( $L_{\text{obs}}$ ) model luminosities for the spectral fits presented in Table 4, Table 5, and Table 6 (see §8 for details). For the coupled MYTORUS fits to the *BeppoSAX* data, luminosity ratios are given for two values of the intrinsic continuum plasma temperature ( $kT = 50$  and 100 keV) in addition to the fit with  $kT = 80$  keV shown in Table 5.

**Table 8.** NGC 4945 Intrinsic Luminosities and Their Ratios to the Eddington Luminosity

Type	Data	Model	Continuum	$kT$ (keV)	$L_{\text{intr}}$ (2–10 keV) ( $10^{42}$ erg s $^{-1}$ )	$L_{\text{intr}}$ (2–195 keV) ( $10^{42}$ erg s $^{-1}$ )	$L_{\text{intr}}/L_{\text{Edd}}$ (2–195 keV)	$L_{\text{intr}}/L_{\text{Edd}}$ (15–100 keV)
Zeroth-order	<i>Swift</i> BAT	MYTORUS	COMPTT	$36^{+62}_{-10}$	19.8	50.3	0.285	0.123
Coupled	<i>Suzaku</i>	MYTORUS	POWERLAW	...	2.86	16.7	0.0946	0.0459
Coupled	<i>Suzaku</i>	MYTORUS	COMPTT	$50 \pm 4$ keV	3.10	15.2	0.0860	0.0446
Coupled	<i>Suzaku</i>	SPHERE	POWERLAW	...	0.64	4.72	0.0267	0.0130
Coupled	<i>BeppoSAX</i>	MYTORUS	COMPTT	50 keV	50.0	126.8	0.717	0.301
Coupled	<i>BeppoSAX</i>	MYTORUS	COMPTT	80 keV	59.4	144.0	0.814	0.326
Coupled	<i>BeppoSAX</i>	MYTORUS	COMPTT	100 keV	65.6	153.5	0.868	0.337
Coupled	<i>BeppoSAX</i>	SPHERE	POWERLAW	...	1.76	7.1	0.0401	0.0185
Coupled	<i>Swift</i> BAT	MYTORUS	POWERLAW	...	2.95	11.1	0.0628	0.0286
Coupled	<i>Swift</i> BAT	MYTORUS	COMPTT	$50^{+16}_{-17}$	2.53	10.1	0.0572	0.02884
Coupled	<i>Swift</i> BAT	SPHERE	POWERLAW	...	0.78	3.41	0.0193	0.00904
Decoupled	<i>Suzaku</i>	MYTORUS	COMPTT	22 keV	14.3	53.7	0.304	0.162
Decoupled	<i>Suzaku</i>	MYTORUS	COMPTT	50 keV	22.3	87.6	0.495	0.239
Decoupled	<i>BeppoSAX</i>	MYTORUS	COMPTT	50 keV	116.8	250.4	1.416	0.520
Decoupled	<i>BeppoSAX</i>	MYTORUS	COMPTT	100 keV	169.1	329.4	1.863	0.605

Absolute luminosities  $L_{\text{intr}}$ , in the 2–10 keV and 2–195 keV bands, corresponding to the intrinsic to observed luminosity ratios shown in Table 7. For each spectral fit, the ratios of the 2–195 keV and 15–100 keV luminosities to the Eddington luminosity,  $L_{\text{Edd}}$ , are also shown.



**Figure 12.** An illustration of how the intrinsic continuum derived for NGC 4945 (grey curves) compares to the total observed spectrum (black curves), and the relative contributions of the zeroth-order continuum (blue), and the Compton-scattered continuum (red). Shown are two degenerate solutions (for coupled and decoupled models) to the *Suzaku* data in (a) and (b), and to the *BeppoSAX* data in (c) and (d). In these examples, the Compton-scattered continuum dominates over the zeroth-order continuum in the region of the Compton hump for the coupled models, whilst the converse is true for the decoupled models. It can be seen that, since the intrinsic continuum must be a certain amount higher than the zeroth-order continuum for a given column density, the intrinsic continuum is highest when the zeroth-order continuum dominates the observed spectrum. Note that the spherical model for the coupled solutions to the *BeppoSAX* data does not allow separation of the Compton-scattered continuum, so only the zeroth-order continuum contribution is shown, which was calculated using the MYTORUS zeroth-order table for the required column density and intrinsic photon index. The parameters of the coupled models are given in Table 5 (see also §6), and those for the decoupled models are given in Table 6 (see also §7).

## 8 VARIABILITY, INTRINSIC LUMINOSITIES, AND EDDINGTON LUMINOSITY RATIOS

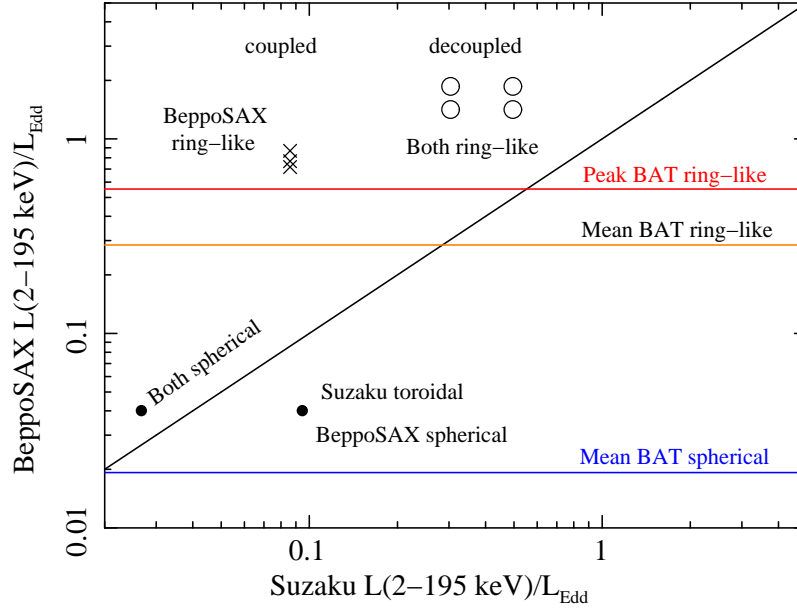
### 8.1 Intrinsic to Observed Luminosity Ratios

In Table 7 we have collected together all of the intrinsic to observed luminosity ratios (in four energy bands) for the various spectral fits described in previous sections. As would be expected, for a given data set, the luminosity ratios for models in which the zeroth-order continuum dominates over the Compton-scattered continuum (above  $\sim 10$  keV) are larger than those for models in which the Compton-scattered continuum dominates (see discussion in §6). The differences in intrinsic luminosity between the two types of model can be substantial. In the 2–10 keV band the luminosity ratios span more than three orders of magnitude for the different models. In the higher energy bands the luminosity ratios are smaller but still can be as great as a factor of 25. Comparing the luminosity ratios for *Suzaku* and *BeppoSAX*, we see that the ratios are larger for the *BeppoSAX* data (the difference between the *Suzaku* and *BeppoSAX* luminosity ratios depends on the energy band and the model, and can be over an order of magnitude).

### 8.2 Absolute Luminosities

Table 8 shows absolute intrinsic luminosities for the various spectral fits in two energy bands, 2–10 keV and 2–195 keV. For the latter, extrapolation of the model over energy gaps in the data was necessary. Fig. 12 helps to visualize how the intrinsic continuum relates to other components of the model for the different classes of solutions for both the *Suzaku* and *BeppoSAX*





**Figure 13.** The ratios of the 2–195 keV intrinsic luminosities to the Eddington luminosity,  $L_{\text{Edd}}$ , for the *BeppoSAX* spectral fits versus the Eddington ratios for the *Suzaku* fits. The solid line corresponds to equality of the *BeppoSAX* and *Suzaku* ratios. Since  $L_{\text{Edd}}$  is constant, the diagram also shows whether various solutions require the intrinsic luminosity during the *Suzaku* observation to be lower or higher than that during the *BeppoSAX* observation. Points below and above the line imply higher and lower luminosities during the *Suzaku* observation respectively. The filled circles correspond to the coupled models in which the Compton-scattered continuum dominates over the zeroth-order continuum (second and fourth columns of results in Table 5). The three crosses correspond to the coupled *BeppoSAX* solutions in which the zeroth-order continuum dominates, for three values of  $kT$  (rows 3 to 5 in Table 3). Open circles correspond to the decoupled model solutions: each solution for *Suzaku* with  $kT = 22$  and 50 keV is plotted against the two solutions for *BeppoSAX* ( $kT = 50$  and 100 keV). These decoupled models also have the zeroth-order continuum dominating at high energies, and such solutions imply a ring-like, geometrically-thin geometry for the X-ray reprocessor. The red horizontal line shows the maximum possible value of  $L_{\text{intr}}/L_{\text{Edd}}$  inferred from the peak value of the 66-month *Swift* BAT lightcurve in Fig. 1, obtained from fitting the *Swift* BAT mean spectrum with a zeroth-order continuum model and renormalizing the intrinsic luminosity to the lightcurve peak. The mean *Swift* BAT Eddington ratio is shown for comparison (brown line), as is the lowest Eddington ratio obtained from fitting the mean spectrum with a spherical model. See Table 8 and §8 for details.

data. In each of the panels in Fig. 12, the grey curves correspond to the intrinsic continua, the red curves to the Compton-scattered continua and the blue curves to the zeroth-order continua. The intrinsic spectrum for the coupled MYTORUS model for the *Suzaku* data in Fig. 12(a) can be directly compared with the intrinsic spectrum for the decoupled MYTORUS model in Fig. 12(b) for the same data. A similar comparison between coupled and decoupled models that were found to be degenerate solutions for the *BeppoSAX* data can be seen in Fig. 12(c) and Fig. 12(d) respectively. For the sake of clarity, we do not show all the possible solutions in Fig. 12, but instead illustrate with examples covering the important different scenarios.

### 8.3 Variability of the Intrinsic Luminosity

For the decoupled models, which are the ones relevant for NGC 4945, the intrinsic continuum luminosity is required to decrease in going from the *BeppoSAX* observation to the *Suzaku* observation. The amount of this decrease depends on the model parameters and the energy band, but it can more than a factor of 2, and even an order of magnitude in the 2–10 keV band. Yet the *observed* luminosities for the *BeppoSAX* and *Suzaku* data are within a factor of 2 of each other (see Table 5, Table 6, and Fig. 10), with the observed luminosity during the *Suzaku* observation being less than, or similar to, the corresponding observed luminosity during the *BeppoSAX* observation.

### 8.4 Ratios of the Intrinsic Luminosity to the Eddington Luminosity

Table 8 also gives intrinsic continuum luminosities ( $L_{\text{intr}}$ ) as a ratio of the Eddington luminosity,  $L_{\text{Edd}}$ , which for the black-hole mass adopted here (see §4), is  $1.77 \times 10^{44}$  erg s $^{-1}$ . The ratios  $L_{\text{intr}}/L_{\text{Edd}}$  (hereafter, equivalently,  $L/L_{\text{Edd}}$ ), are shown in Table 8 for intrinsic luminosities in the 2–195 keV band, which is likely to be within a factor of  $\sim 2$ –4 of the bolometric luminosity (e.g., see Vasudevan et al. 2010). However, the 2–195 keV luminosities involve some extrapolation of the models for different data sets, so we have also computed  $L/L_{\text{Edd}}$  in the 15–100 keV band, since this is covered by the *Suzaku*, *BeppoSAX*, and *Swift* BAT data. The consistency of the behavior of  $L/L_{\text{Edd}}$  in the two energy bands is evident from Table 8. As we might

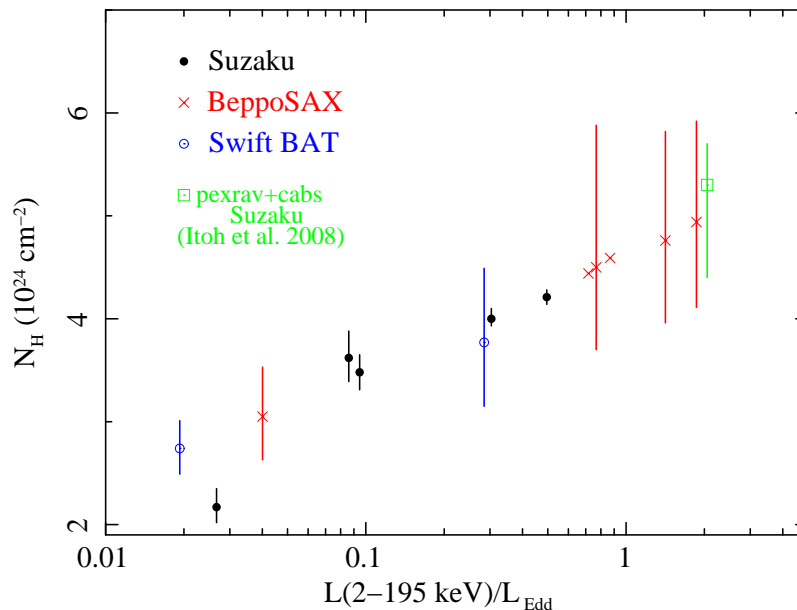
expect, the models in which the zeroth-order continuum dominates have the largest value of  $L/L_{\text{Edd}}$ , and all of these models have a 2–195 keV  $L/L_{\text{Edd}}$  ratio greater than 0.28. For the case of the decoupled *BeppoSAX* models,  $L/L_{\text{Edd}}$  exceeds unity. Since the bolometric value of  $L/L_{\text{Edd}}$  is higher than the corresponding ratio for the 2–195 keV band, all of the decoupled models present a difficulty.

Previous X-ray studies of NGC 4945 also deduced a high value for  $L/L_{\text{Edd}}$  (e.g., Itoh et al. 2008; Fukazawa et al. 2011; Marinucci et al. 2012). This is because the decoupled models we have applied have much in common with disk-reflection models. A value of  $R \sim 3 \times 10^{-3}$ , (the relative “reflection fraction” in the PEXRAV model), was obtained by Itoh et al. (2008), and this is consistent with the high-energy spectrum being dominated by the zeroth-order continuum. From their analysis of the *BeppoSAX* data, Guainazzi et al. (2000) came to similar conclusions from applying the same kind of model (PEXRAV and CABS), namely that there is no evidence for Compton reflection ( $R \ll 1$ ), and that the intrinsic luminosity is a significant fraction of the Eddington luminosity. As expected, our Compton-thick column densities and inferred intrinsic luminosities from the decoupled MYTORUS fits are similar to the corresponding values obtained by Guainazzi et al. (2000). However, as we have pointed out, the method of using PEXRAV and CABS may be biased towards finding the solutions dominated by the zeroth-order continuum and these may not be appropriate for all Compton-thick AGNs. At the other extreme, Table 8 shows that coupled models in which the Compton-scattered continuum dominates give much lower values of  $L/L_{\text{Edd}}$ . Specifically, the spherical model fitted to the *Suzaku*, *BeppoSAX*, and *Swift* BAT data gave values of  $\sim 0.027$ ,  $\sim 0.040$ , and  $\sim 0.019$  respectively for the 2–195 keV  $L/L_{\text{Edd}}$  ratio. However, these solutions are not relevant for NGC 4945 because of the independent variability of the high-energy continuum with respect to the Fe K $\alpha$  line (the spectrum above 10 keV cannot be dominated by the Compton-scattered continuum). Nevertheless, we discuss the solutions for possible relevance to other AGNs. These Compton-thick solutions with a spherical geometry are missed by the standard scheme of modeling Compton-thick AGNs because the Compton-scattered continuum from a fully-covering reprocessor can have a shape that is more like the zeroth-order continuum (but with a different column density) than a disk-reflection continuum. Fitting the X-ray spectrum from a fully-covered Compton-thick source with disk-reflection can lead to the erroneous conclusion that the “reflection fraction” ( $R$ ) is negligible, when in fact the spectrum is *dominated* by the Compton-scattered continuum. However, every AGN should be assessed on a case-by-case basis because the parameter  $R$  in disk-reflection models is in general allowed to float with no constraint. Indeed, BN11 concluded that in their sample of obscured AGNs, the disk-reflection models gave lower intrinsic luminosities than toroidal models.

#### 8.4.1 A Comparison of the Eddington Ratio and Column Density for Different Models

In the case of NGC 4945, there is a further problem with the high values of  $L/L_{\text{Edd}}$  obtained for some of the models. We illustrate this in Fig. 13, which shows the 2–195 keV  $L/L_{\text{Edd}}$  ratios obtained from the *BeppoSAX* data versus the 2–195 keV  $L/L_{\text{Edd}}$  ratios obtained from the *Suzaku* data, for comparable models. The diagonal solid line corresponds to an equal ratio for the two data sets. Points that lie below this line require that the intrinsic luminosity of NGC 4945 during the *BeppoSAX* observation was less than that during the *Suzaku* observation, whereas points that lie above the line indicate a change in luminosity in the opposite sense (i.e., larger luminosities during the *BeppoSAX* observation). The problem arises when we consider the fact that if we fit the time-averaged 58-month *Swift* BAT spectrum with a model that consists of *only* the zeroth-order continuum, then we obtain an absolute upper limit on the intrinsic continuum luminosity (averaged over 58-months). We can then obtain a normalization factor from the *Swift* BAT light curve (Fig. 1) and estimate the maximum intrinsic luminosity that was attained during the 66-month period covered by the light curve (by dividing the highest peak flux by the mean flux). Thus, we can estimate the highest value of the 2–195 keV  $L/L_{\text{Edd}}$  ratio that NGC 4945 attained during the period covered by the *Swift* BAT lightcurve, and this is shown as a red line in Fig. 13. For reference, the value of  $L/L_{\text{Edd}}$  is also shown for the mean level of the *Swift* BAT light curve (brown line), and also for the spherical model fit to the *Swift* BAT spectrum (blue line; see also Table 4). The problem is that *all* of the models in which the zeroth-order continuum dominates require that the intrinsic luminosity during the *BeppoSAX* observation was higher than it ever was during the *Swift* BAT 66-month monitoring. While this is not impossible, it should be remembered that these solutions for the *BeppoSAX* data require super-Eddington luminosities.

We also see from Table 7 and Table 8 that whereas key model parameters such as  $N_{\text{H}}$  were not sensitive to the assumed plasma temperature ( $kT$ ) in the decoupled fits, the inferred intrinsic to observed luminosity ratio in the 2–10 keV band *does* depend on the plasma temperature. The difference is greatest between the  $kT = 22$  keV and  $kT = 50$  keV *Suzaku* fits, the latter yielding a ratio  $\sim 60\%$  larger than the former. For the *BeppoSAX* data, the difference is only  $\sim 20\%$  between the fits with  $kT = 50$  keV and  $kT = 100$  keV. The dependence of the intrinsic to observed luminosity ratios on  $kT$  is less for the higher energy bands, and for all fits and data sets. This is because changes in the shape of the spectrum produce larger flux amplification at low energies if the spectrum pivots at high energies. Considering all of the models and all of the data sets, the possible range in intrinsic luminosity from the NGC 4945 spectral fits alone spans over two orders of magnitude in the 2–10 keV band, and just under two orders of magnitude in the 14–195 keV band. The derived values of  $N_{\text{H}}$  from the various fits span the range  $\sim 2\text{--}6 \times 10^{24} \text{ cm}^{-2}$  (including statistical errors), and are plotted against the corresponding values of the



**Figure 14.** The column density of the Compton-thick X-ray reprocessor obtained from various spectral fits reported in Table 4, Table 5, and Table 6, versus the corresponding ratio of the 2–195 keV intrinsic continuum luminosity to the Eddington luminosity (see Table 8). The diagram shows at glance the range of  $N_{\text{H}}$  (a factor greater than 2) spanned by the spectral fits over the different models that were applied to three data sets (from *Suzaku*, *BeppoSAX*, and *Swift* BAT). The diagram also shows at a glance the corresponding range in the intrinsic Eddington luminosity ratio, which is very large, about 2 orders of magnitude. As might be expected, spectral solutions with higher values of  $N_{\text{H}}$  generally have higher intrinsic broadband luminosities. Note that statistical errors are not shown for two of the *BeppoSAX* points (red crosses) because only best-fitting parameters were obtained for these coupled model fits, which have  $kT = 50$  and 100 keV. The statistical errors are similar to those for the corresponding coupled model fit with  $kT = 80$  keV (see Table 5).

2–195 keV Eddington ratio in Fig. 14. As might be expected,  $N_{\text{H}}$  is greater for greater values of  $L/L_{\text{Edd}}$ . For comparison, we used the parameters of the PEXRAV/CABS model applied by Itoh et al. (2008) to estimate the 2–195 keV  $L/L_{\text{Edd}}$  ratio, and show this in Fig. 14 (green data point). It can be seen that this value of  $L/L_{\text{Edd}}$  is greater than 2 and is higher than any of the values we obtained from any of our models applied to any of the three data sets.

### 8.5 Interpretation of the Allowed Solutions for NGC 4945

In summary, since the fact that the spectrum above 10 keV in NGC 4945 must be dominated by the zeroth-continuum is robust, values of  $L/L_{\text{Edd}}$  close to or greater than unity are unavoidable. The most straightforward geometrical interpretation of our results is that the central X-ray source is obscured by a single clumpy distribution, with the line of sight obscured by material in the same distribution (its components must be larger than the X-ray source). The size of the distribution would have to be on a scale of tens of parsecs if it is to be identified with the spatially-resolved Fe K $\alpha$  line-emitting region reported in Marinucci et al. (2012). The covering factor must be small enough that the Compton-scattered continuum does not dominate over the zeroth-order continuum above 10 keV. Our spectral fitting results indicate that the covering factor is of the order of  $\sim 10\%$  or less. A separate, more compact, ring-like structure in addition to the extended distribution is not ruled out (its covering factor would have to be small enough to make a negligible contribution to the Fe K $\alpha$  line).

So far we have only considered an isotropic X-ray continuum source. However, there is a viable and intriguing alternative possibility that alleviates the need for a central source with such an enormous luminosity radiating near or beyond the Eddington limit. That is, NGC 4945 could harbor a beamed AGN, embedded in a patchy or clumpy Compton-thick shell that could have a large covering factor. The X-ray emission in such a scenario would need to be collimated along the line of sight so that the true ratio of  $L/L_{\text{Edd}}$  could be an order of magnitude less than unity. The Compton-scattered continuum would be swamped by the direct zeroth-order continuum, regardless of the geometry and covering factor of the Compton-thick circumnuclear matter. Beaming is not uncommon in type 1 AGNs and surrounding such a source with a Compton-thick shell would produce an object like NGC 4945. If the true intrinsic luminosity of NGC 4945 is closer to  $10^{43} \text{ erg s}^{-1}$  than  $10^{44} \text{ erg s}^{-1}$ , and if the X-ray emission were *not* beamed along our line of sight, the Compton-thick obscuration would make it difficult to detect the source in hard X-ray surveys. In other words, there could be a large number of beamed Compton-thick AGNs with intrinsic luminosities of the order of  $10^{43} \text{ erg s}^{-1}$  or less that have not been detected because of an unfavorable beaming direction.

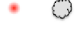
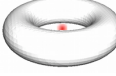

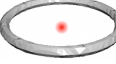

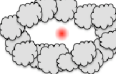

The beaming scenario is consistent with all of the X-ray observational constraints in NGC 4945 and actually provides

a more natural interpretation of the data than an isotropic X-ray source surrounded by a Compton-thick structure that cannot have a covering factor that is too large or too small. If NGC 4945 is a beamed Compton-thick AGN, no fine-tuning of the covering factor is required. Independent evidence of beamed emission has also been found in the radio band by Lenc & Tingay (2009), who reported the discovery of a jet-like structure at 2.3 GHz, with apparent dimensions of  $\sim 5$  pc in length by  $\sim 1.5$  pc in width. The alignment of the putative jet could not be constrained uniquely, but Lenc & Tingay (2009) derived  $\beta \cos \theta > 0.52$ , where  $\beta \equiv (v/c)$  is the speed of the jet material, and  $\theta$  is the angle between the direction of motion and the line of sight. Therefore, alignment of the putative jet emission along the line of sight is not ruled out if  $\beta > 0.52$  ( $\beta$  is unknown). Moreover, the detection of NGC 4945 in the GeV band by Fermi (Lenain et al. 2011) lends further support to the beaming scenario for the intrinsic X-ray continuum.

## 9 SUMMARY

We have presented a detailed methodology for applying the MYTORUS X-ray reprocessor model to X-ray spectra of AGN, and we have presented the results of applying the model to noncontemporaneous *Suzaku*, *BeppoSAX*, and *Swift* BAT data for the Seyfert 2 galaxy NGC 4945. We have also applied the toroidal and spherical models of Brightman and Nandra (2011) to these data. We have given detailed procedures to implement several different geometrical configurations for the X-ray reprocessor, some of which are exact, and some are approximations. Although the different modes of applying the MYTORUS suite of models to emulate structures that are different to the standard, uniform torus are approximations in some cases, the models overcome some important restrictions imposed by disk-reflection models. The different schemes, which are not just restricted to Compton-thick AGNs, are summarized and illustrated in Fig. 15. Below we summarize our general conclusions and then summarize the specific conclusions for NGC 4945.

- (i) The current scheme of using a disk-reflection spectrum to model the Compton-scattered continuum assumes an infinite column density so such models cannot access the rich variety of spectral shapes that result from finite column densities. Disk-reflection models may also not be able to access spectral solutions with the full range of intrinsic continuum luminosities that are allowed by the data.
- (ii) In sources that are Compton-thick in the line of sight, that component of the continuum diminished by matter in the line of sight (the zeroth-order continuum) will not leave a prominent signature below  $\sim 10$  keV (in the form of the structure in the Fe K band, and continuum curvature below it). This may give rise to ambiguity in the possible model solutions, even for high signal-to-noise data. Conversely, for Compton-thin sources with column densities in the range  $\sim 10^{23}$  to  $\sim 10^{24}$  cm $^{-2}$ , the spectrum below 10 keV will have specific contributions from the Compton-scattered continuum, zeroth-order continuum, and fluorescent line emission, leading to less ambiguity in allowed spectral solutions. (Sources with column densities less than  $10^{23}$  are of course much simpler to model.)
- (iii) In Compton-thick sources it is possible that the dominant spectral components in the  $\sim 5 - 10$  keV band are due to X-ray reflection and fluorescence from the back side of obscuring matter located on the “far-side” of a clumpy or patchy structure. In other words, spectral components from the near-side of the structure could be so suppressed that even if only a few per cent or less of the far-side reflection is unobscured, it could still dominate the spectrum in the Fe K band.
- (iv) In cases in which significant variability above  $\sim 10$  keV has been established, the spectral solution, or solutions, adopted must be consistent with the variability data. Specifically, either the zeroth-order continuum must dominate over the Compton-scattered continuum in the pertinent energy band, or else the entire reprocessing structure must have a light-crossing time that is sufficiently small to be consistent with the variability. Which continuum component dominates in a given energy band is a complex function of the geometry, global covering factor, and column density (both in and out of the line of sight). Each data set must be assessed on a case-by-case basis.
- (v) If there is no variability information, one must explore all permissible spectral solutions, which might be associated with very different intrinsic continuum luminosities. We have emphasized the need for models to allow the zeroth-order continuum, Compton-scattered continuum, and the Fe K $\alpha$  line flux to be independently varied, in order to accommodate spectral variability and/or light-crossing time delays, which should be considered even if only a single observation is available. Currently, only the MYTORUS model allows separability of the different model components.
- (vi) In general, an X-ray reprocessor model that fits a spectrum and is dominated by the zeroth-order continuum in a given energy band has the largest possible intrinsic luminosity in that energy band because any Compton-scattered continuum from material out of the line of sight can only reduce the required intrinsic luminosity to produce the same flux. On the other hand a fully-covering distribution of matter gives a spectrum above  $\sim 10$  keV that is dominated by the Compton-scattered continuum if the material is Compton-thick. Therefore, spectral fits with only a zeroth-order continuum model and with a spherical model can yield upper and lower limits on the intrinsic continuum luminosity respectively (they will be equal in the Compton-thin limit).
- (vii) We have described an important extension to the MYTORUS model that allows the use of a thermally Comptonized intrinsic

	<p>MYTZ (<math>\theta_{\text{obs}} = 90^\circ</math>).</p> <p>Zeroth-order continuum only. Blob or cloud in the line of sight, global covering factor too small to produce detectable fluorescent line emission. <i>Alternatively</i>, MYTZ is suitable for any geometry if the energy bandpass of the data exclude significant contribution from scattered continuum and fluorescent lines. The component can be included as part of a single MYTZ component (with decoupled column density) in any of the models below.</p>
	<p>MYTZ, <math>A_S</math>MYTS (<math>\theta_{\text{obs}}</math> and <math>N_H</math> coupled).</p> <p>Literal torus, with a global covering factor of 0.5. See decoupled models for emulating different covering factors and variants in the detailed geometry.</p>
	<p>BN11 or MYTZ and <math>A_S</math> MYSS</p> <p>Uniform spherical distribution. BN11 sphere does not allow separation of the zeroth-order continuum. MYSS is an independent scattered continuum for a sphere, which will be a future addition to the MY suite.</p>
	<p><math>A_{S00}</math>MYTS (<math>\theta_{\text{obs}} = 0^\circ</math>): Uniform, face-on ring.</p>
    	<p>MYTZ, <math>A_{S90}</math> MYTS (<math>\theta_{\text{obs}} = 90^\circ</math>): Uniform, edge-on ring (<math>N_H</math> decoupled).</p> <p>Generalized approximation for a uniform or clumpy (patchy) arbitrary distribution of matter, with an arbitrary effective global covering factor:</p> <p>MYTZ, <math>A_{S00}</math>MYTS, <math>A_{S90}</math>MYTS</p> <p><math>\theta_{\text{obs}}</math> decoupled, <math>90^\circ</math> for MYTZ, <math>0^\circ</math> for <math>A_{S00}</math>, and <math>90^\circ</math> for <math>A_{S90}</math>.</p> <p>Decoupling <math>\theta_{\text{obs}}</math> emulates back-reflection from a patchy distribution, or a modified edge structure in a uniform distribution.</p> <p><math>N_H</math> values optionally coupled or decoupled.</p> <p>Decouple <math>N_H</math> if line-of-sight and global average column densities are different. Especially useful for sources with variable column density.</p>

**Figure 15.** A schematic summary for modeling the X-ray absorption and reprocessing in AGNs for different physical configurations of the obscuring matter. The X-ray continuum source is shown as a red, filled circle.

continuum. These spectra have a natural high-energy rollover, characterized by the plasma temperature,  $kT$ . Currently, the MYTORUS suite of models is the only one publicly available that allows an intrinsic continuum that is not a simple power law. We found that despite the poor spectral resolution of the *Swift* BAT spectra, it is possible in some situations for even *Swift* BAT data to be able distinguish between the power-law and thermally Comptonized intrinsic continua.

We now summarize below the specific results and conclusions from applying our methods to *Suzaku*, *BeppoSAX*, and *Swift* BAT data for NGC 4945.

(i) Whereas the noncontemporaneous *Suzaku* and *BeppoSAX* NGC 4945 data cover a period of time of the order of a day, the *Swift* BAT spectrum from the ongoing all-sky survey was time-averaged over 58 months. The data sets were therefore fitted

independently.

(ii) For Comptonized thermal plasma models of the intrinsic continuum, the temperature of the Comptonizing plasma,  $kT$ , is difficult to constrain precisely because it is model-dependent. In general, the *Suzaku* data are consistent with  $kT$  in the range 20–50 keV, whilst the *BeppoSAX* data have a preference for  $kT$  in the range 50–100 keV. The *Swift* BAT constraints on  $kT$  are looser and consistent with those from both *Suzaku* and *BeppoSAX*.

(iii) We found that even for the *Suzaku* data (which cover the most spectral features and have the best spectral resolution in the Fe K band), degenerate spectral solutions exist. Even applied to a single spectrum, these degenerate solutions can yield intrinsic luminosities that differ by an order of magnitude or more. The different models applied to the different data sets for NGC 4945 cover a range in intrinsic luminosity that spans two orders of magnitude and nearly a factor of 3 in column density (from  $\sim 2 \times 10^{24}$  to  $6 \times 10^{24}$  cm $^{-2}$ ). Yet the *observed* luminosities of the *BeppoSAX* and *Suzaku* spectra do not differ by more than a factor of 2.

(iv) The 66-month *Swift* BAT light curve shows large-amplitude variability on a timescale of months, covering a dynamic range of a factor of  $\sim 8$  from minimum to maximum flux. Marinucci et al. (2012) presented independent evidence that the Fe K $\alpha$  line flux is spatially extended over a region of  $\sim 30$  pc, and does not respond to continuum variability. This means that only those spectral solutions that we obtained in which the zeroth-order continuum dominates above 10 keV are permissible for NGC 4945.

(v) The last inference above also means that the Compton-scattered continuum must be sufficiently suppressed so that it never dominates above  $\sim 10$  keV, and our modeling quantifies this constraint. Our results also show that the Fe K $\alpha$  line and the Compton-scattered continuum must be dominated by emission from matter illuminated on the “back side.” Thus, one possibility for the structure of the X-ray reprocessor is a clumpy medium with a global covering factor that is small enough to prevent the Compton-scattered continuum from dominating the high-energy spectrum (the exact value is model-dependent). Two separate structures cannot be ruled out, such as a ring-like (edge-on) compact structure responsible for the line-of-sight extinction, along with a larger, extended clumpy medium. However, our modeling shows that the line-of-sight column density is similar to that out of the line of sight.

(vi) The requirement that the spectrum above 10 keV has to be dominated by the zeroth-order continuum also requires a bolometric luminosity that is of the order of or greater than the Eddington luminosity. However, this is based on isotropic intrinsic X-ray emission. Previous studies have also noted the problematic Eddington ratio, and indeed, NGC 4945 was excluded from the sample in a study of bolometric corrections from X-ray and infrared data by Vasudevan et al. (2010).

(vii) Another possibility arises if the intrinsic X-ray continuum is beamed or collimated along our line of sight. This would alleviate the need for fine-tuning the covering factor of the extended, clumpy medium because the Compton-scattered continuum and fluorescent line emission from matter that is not close to the beaming direction would be relatively weak. If the individual clumps are much larger than the X-ray source, the same distribution could provide the line-of-sight extinction. Beaming also relieves the need for an intrinsic X-ray luminosity that is close to, or exceeds the Eddington luminosity. The actual intrinsic luminosity could easily be an order of magnitude less if the beaming scenario is correct. The beaming scenario appears to be supported by the detection of a jet-like structure in the radio band (Lenc & Tingay 2009), and the detection of NGC 4945 in GeV band by Fermi (Lenain et al. 2011).

Our results also serve to demonstrate that weak, heavily obscured AGNs found in deep X-ray surveys may have column densities and intrinsic luminosities that are different to those inferred from modeling the spectra with disk-reflection spectra. In particular, the X-ray spectrum of a fully-covered Compton-thick source resembles the spectrum from a Compton-thick source with a negligible covering factor more than it resembles a disk-reflection spectrum. Thus, sources that are dominated by a Compton-scattered (reflection) spectrum might be mistakenly classified as showing no evidence for reflection, as testified by a negligible value of  $R$ . Given the expected spectral degeneracies, it may not be possible even in principle to infer the source composition of the cosmic X-ray background without directly resolving it at high energies.

Finally, it should be clear from our results that, aside from the complex dependence of the Fe K $\alpha$  line flux on  $N_{\text{H}}$  and geometry (e.g., Yaqoob et al. 2010), the possible large range in the intrinsic continuum luminosity for those sources that admit degenerate models means that the Fe K $\alpha$  line flux cannot be used as a simple proxy for the intrinsic continuum luminosity. Nor can the Fe abundance be trivially deduced from the depth of the Fe K edge because the edge depth has a complex dependence on the column density and geometry of the X-ray reprocessor.

## 10 APPENDIX: ANALYSIS OF A SUZAKU OBSERVATION OF 3C 273

In this section we utilize data from a *Suzaku* observation of 3C 273 in order to derive cross-normalization factors for the XIS, HXD/PIN, and HXD/GSO instruments. Although the *Suzaku* Guest Observer Facility (GOF) has published XIS:PIN cross-normalization ratios<sup>10</sup>, these ratios depend on the energy bands of the XIS and HXD data that are used for fitting, and

<sup>10</sup> <ftp://legacy.gsfc.nasa.gov/suzaku/doc/xrt/suzakumemo-2008-06.pdf>

the actual spectrum of the source. The given cross-normalizations were derived from *Suzaku* spectra of the Crab nebula. The Crab X-ray spectrum is very steep, with a photon index greater than 2, and the high count rate can induce pile-up problems in the CCDs. In the HXD/PIN and HXD/GSO bands, the detailed Crab spectrum is actually unknown and must be *assumed* (all previous X-ray instruments have been calibrated with the Crab spectrum, based on assumptions about its spectrum). For *Suzaku*, the calibration *assumes* a broken power-law continuum, and *assumes* values for the photon indices of the two continuum components, and the break energy. Therefore, using instrument cross-normalizations derived from a “simple” point source such as 3C 273 is more appropriate for use with the analysis of AGN *Suzaku* spectra, making use of matching energy bands for fitting the 3C 273 data and the target source. For the HXD/GSO, the cross-normalization with the XIS is even more uncertain than it is for HXD/PIN:XIS. Again, the cross-normalization depends on the exact energy bands used for spectral fitting, and the spectrum of the source. The statement by the *Suzaku* GOF does not provide sufficient quantitative information, saying only that, “there is a cross-normalization problem at the 20% level (1.0:0.80, PIN:GSO).”<sup>11</sup> Although energy-dependent “ancillary response files” (ARFs) have been released for use with the GSO to empirically compensate for remaining calibration residuals, these files were derived from fitting Crab data, and from fitting over a much broader energy band than would be typical for AGN *Suzaku* data. Again, the parameters of the Crab spectrum were *assumed*, and the official *Suzaku* GOF description of the GSO ARF files states that the uncertainty in the Crab parameters “is still being studied.”<sup>12</sup> Therefore, we do not employ the empirical GSO ARF files for either 3C 273 or NGC 4945. Instead, we employ only the default response matrices for the HXD/PIN and HXD/GSO, and derive the HXD/PIN:XIS and HXD/GSO:XIS cross-normalization ratios directly from the 3C 273 data, and then adopt those ratios for fitting the *Suzaku* NGC 4945 data.

*Suzaku* observed the bright quasar 3C 273 ( $z = 0.158$ ) in the period 2007, June 30 to 2007, July 1 for a duration of  $\sim 85$  ks (from which net exposure times after data screening and cleaning were  $\sim 54.9$  ks and  $\sim 48.0$  ks for the XIS and HXD respectively). The observation was made in “HXD nominal” mode, which refers to one of the default aimpoints of the telescope and detector system that optimizes the count rate in the HXD, as opposed to the XIS. The data were first reprocessed with version 1.01 of the pipeline reprocessing software, AEPIPELINE, used in conjunction with the *Suzaku* FTOOLS version 16, which were part of the general HEASoft (version 6.9) release<sup>13</sup>. The latest calibration data base (CALDB) versions in effect at the time of data processing and reduction were “XIS CALDB 20100709”, “HXD CALDB 20100812” and “XRT CALDB 20080709.” For the HXD/GSO, the gain calculation and gain history file changed significantly after 2010, August 20<sup>14</sup>, and the new implementation was employed in the current data reprocessing.

Default data screening and cleaning criteria were employed in the pipeline reprocessing.<sup>15</sup> The HXD background files released for the 3C 273 observation were used in conjunction with the *Suzaku* FTOOLS to generate background spectra.<sup>16</sup> For the HXD/PIN, files corresponding to the “tuned” version of the background were used<sup>17</sup>, and for the HXD/GSO, version 2.0 of the background files were employed<sup>18</sup>.

For the XIS, data were available only from XIS0, XIS1, and XIS3 since XIS2 was already no longer available for the 3C 273 observation. On-source data were extracted from the screened and cleaned event fits from a circular region with a radius of  $2.60'$ , from each detector. Background spectra were extracted from several rectangular regions that were sufficiently distant from 3C 273 and the calibration sources. The on-source spectra from the three XIS detectors were combined into a single spectrum, and the combined background spectrum from the three XIS detectors was subtracted in order to obtain the final XIS spectrum of 3C 273. The background-subtracted XIS count rate averaged over the observation and the three detectors is  $4.582 \pm 0.005$  ct/s in the 0.5–10 keV band. The XIS background constitutes only 0.9% and 4.7% of the total on-source count rate in the 0.5–10 keV and 8–10 keV bands respectively (the relative contribution of the background is highest at the high-energy end of the bandpass). Spectral fitting was performed over identical energy ranges to those used for the NGC 4945 analysis in the present paper. These ranges were 0.7–9.82 keV (XIS, excluding the poorly calibrated 1.83–1.93 keV range), 11.6–47.7 keV (HXD/PIN), and 80–165 keV (HXD/GSO). The background-subtracted count rates in these bands are:  $4.260 \pm 0.005$ ,  $0.436 \pm 0.004$ , and  $0.148 \pm 0.018$  for the XIS, HXD/PIN, and HXD/GSO respectively. In these energy bands, 3C 273 contributes 99.4%, 48.7%, and 1.8% of the total on-source count rate. The source contribution in the GSO is very small compared to the background, so systematic errors in the GSO background model (up to 2%<sup>19</sup> of the nominal predicted background count rate) could have a significant effect on the background-subtracted spectrum. However, we did not apply any systematic adjustments or systematic errors for the baseline spectral fitting so that we could examine the true residuals to the default background model.

<sup>11</sup> <http://heasarc.gsfc.nasa.gov/docs/suzaku/analysis/watchout.html>

<sup>12</sup> [http://heasarc.gsfc.nasa.gov/docs/suzaku/analysis/gso\\_newarf.html](http://heasarc.gsfc.nasa.gov/docs/suzaku/analysis/gso_newarf.html)

<sup>13</sup> [http://heasarc.gsfc.nasa.gov/docs/suzaku/analysis/suzaku\\_ftools.html](http://heasarc.gsfc.nasa.gov/docs/suzaku/analysis/suzaku_ftools.html)

<sup>14</sup> [http://heasarc.gsfc.nasa.gov/docs/suzaku/analysis/gso\\_newgain.html](http://heasarc.gsfc.nasa.gov/docs/suzaku/analysis/gso_newgain.html)

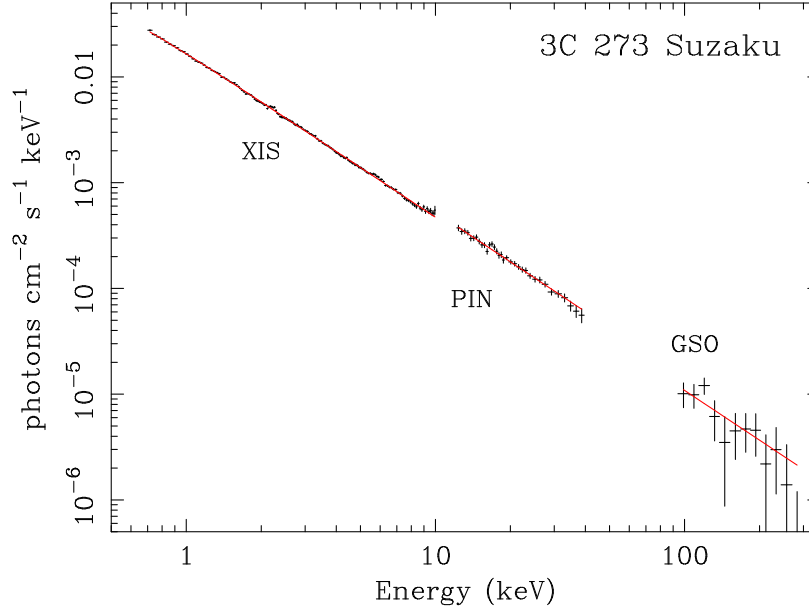
<sup>15</sup> These can be found at <http://heasarc.gsfc.nasa.gov/docs/suzaku/processing/v231225.html>.

<sup>16</sup> For the HXD/PIN: `ae702070010_hxd_pinbgd.evt`; for the HXD/GSO: `ae702070010_hxd_gsobgd.evt`.

<sup>17</sup> <http://heasarc.gsfc.nasa.gov/docs/suzaku/analysis/pinbgd.html>

<sup>18</sup> <http://heasarc.gsfc.nasa.gov/docs/suzaku/analysis/gsobgd.html>

<sup>19</sup> <http://heasarc.gsfc.nasa.gov/docs/suzaku/analysis/gsobgd.html>



**Figure 16.** 3C 273 *Suzaku* unfolded photon spectrum, obtained from fitting the data with a simple power-law continuum model and Galactic absorption, with free HXD/PIN:XIS and HXD/GSO:XIS relative normalization ratios (see text for details). The data from XIS0, 1, and 3 are combined into a single spectrum. Note that the data were fitted over narrower energy ranges than shown, in order to match the NGC 4945 energy ranges that were fitted (see text for details). These energy ranges were 0.7–9.82 keV (XIS, excluding the poorly calibrated 1.83–1.93 keV range), 11.6–47.7 keV (HXD/PIN), and 80–165 keV (HXD/GSO).

For the XIS, one of the default bin sizes,  $\sim 30$  eV (512-channel spectrum), was used, and the default binning for the HXD/PIN (375 eV per bin, 256 channels) was used. For the GSO, the spectrum must be made with energy bin widths that match the predicted model background spectrum, and these have a variable, predetermined width.<sup>20</sup> The GSO spectrum was then further binned by a factor of 2 to improve the signal-to-noise ratio.

Response matrices (“RMF” files), and telescope effective area files (“ARFs”) were made using the *Suzaku* FTOOLS XIS-RMFGEN and XISSIMARFGEN respectively. The three “rmf” and three “arf” files were all combined, using the appropriate weighting (according to the count rates for each XIS), into a single response file for the combined XIS background-subtracted spectrum of 3C 273. The HXD response files used were `ae_hxd_pinhxnome1_20080129.rsp` and `ae_hxd_gsohxnom_20100524.rsp` for the PIN and GSO respectively.

The 3C 273 XIS, HXD/PIN and HXD/GSO data were fitted in the energy ranges mentioned above, with a simple power-law continuum with Galactic absorption. A column density of  $1.79 \times 10^{20} \text{ cm}^{-2}$  was used in the Galactic absorption model (Dickey & Lockman 1990). There were a total of four free parameters: the photon index,  $\Gamma$ , the overall normalization, the normalization of the HXD/PIN model relative to the XIS model ( $C_{\text{PIN:XIS}}$ ), and the normalization of the HXD/GSO model relative to the XIS ( $C_{\text{GSO:XIS}}$ ). The best-fitting model and unfolded photon spectrum are shown in Fig. 16. The data are shown over wider energy bands for each instrument than were actually fitted in order to show as much of the highest quality data as possible.

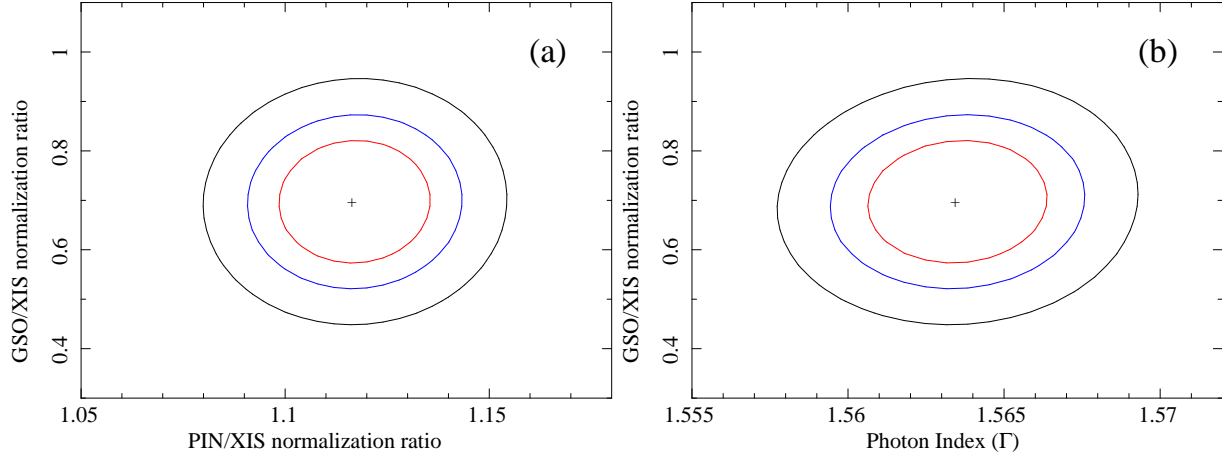
We obtained  $\chi^2 = 508.8$  for 416 degrees of freedom, and best-fitting parameter values of  $C_{\text{PIN:XIS}} = 1.12^{+0.02}_{-0.03}$ ,  $C_{\text{GSO:XIS}} = 0.70^{+0.14}_{-0.14}$ , and  $\Gamma = 1.564^{+0.003}_{-0.004}$  (errors are 90% confidence for one interesting parameter). In Fig. 17(a) we show contours corresponding to 68%, 90%, and 99% confidence for  $C_{\text{GSO:XIS}}$  versus  $C_{\text{PIN:XIS}}$ . In Fig. 17(b) we show contours for the same confidence levels, for  $C_{\text{GSO:XIS}}$  versus  $\Gamma$ .

#### Acknowledgments

The author thanks an anonymous referee for diligent reading of the manuscript and helping to improve the paper. The author also thanks A. Marinucci and G. Risaliti for very helpful discussions. The author is indebted to NASA’s research programs that have made this work possible and is grateful for partial support from NASA grants NNG04GB78A and NNX09AD01G. This research has made use of data and software provided by the High Energy Astrophysics Science Archive Research Center (HEASARC), which is a service of the Astrophysics Science Division at NASA/GSFC and the High Energy Astrophysics Division of the Smithsonian Astrophysical Observatory.

<sup>20</sup> [http://heasarc.gsfc.nasa.gov/docs/suzaku/analysis/gso\\_newgain.html](http://heasarc.gsfc.nasa.gov/docs/suzaku/analysis/gso_newgain.html)





**Figure 17.** Contours corresponding to 68% (red lines), 90% (blue lines), and 99% (black lines) confidence for two interesting parameters, obtained from a simple power-law, three-instrument fit to 3C 273 *Suzaku* data, with Galactic absorption. (a) HXD/GSO:XIS versus HXD/PIN:XIS relative normalizations ( $C_{\text{GSO:XIS}}$  and  $C_{\text{PIN:XIS}}$  respectively). (b) HXD/GSO:XIS normalization ( $C_{\text{GSO:XIS}}$ ) versus the power-law photon index,  $\Gamma$ .

This paper has been produced using the Royal Astronomical Society/Blackwell Science L<sup>A</sup>T<sub>E</sub>X style file.

## REFERENCES

- Anders E., Grevesse N., 1989, *Geochimica et Cosmochimica Acta* 53, 197
- Arnaud K. A., 1996, in *Astronomical Data Analysis Software and Systems V*, ed. Jacoby, G., Barnes, J. (Astronomical Society of the Pacific), Conference Series, Vol. 101, p. 17
- Barthelmy S. D., 2005, *Sp. Sci. Rev.*, 120, 143
- Bearden J. A., 1967, *Rev. Mod. Phys.*, 39, 78
- Boella G., et al., 1997, *A&AS*, 122, 327
- Brightman M., Nandra K., 2011, *MNRAS*, 413, 1206 (BN11)
- Burlon D., Ajello M., Greiner J., Comastri A., Merloni A., Gehrels N., 2011, *ApJ*, 728, 58
- Dadina M., 2007, *A&A*, 461, 1209
- Dickey, J. M., & Lockman, F. J. 1990, *ARA&A*, 28, 215
- Done C., Madejski G. M., Smith D. A., 1996, *ApJ*, 463, 63
- Fabian A. C., 1999, *MNRAS*, 308, L39
- Frontera F., Costa E., Fiume D. D., Feroci M., Nicastro L., Orlandini M., Palazzi E., Zavattini G. 1997, *A&AS*, 122, 357
- Fukazawa Y., et al., 2011, *ApJ*, 727, 19
- Gehrels N., 2004, *ApJ*, 611, 1005
- Ghisellini G., Haardt F., Matt G., 1994, *MNRAS*, 267, 743
- Gilli R., Comastri A., Hasinger G., 2007, *A&A*, 463, 79
- Greenhill L. J., Moran J. M., Herrnstein J. R., 1997, *ApJ*, 481, L23
- Guainazzi M., Matt G., Brandt W. N., Antonelli L. A., Barr P., Basani L. 2000, *A&A*, 356, 463
- Heiles C., Cleary M. N., 1979, *Australian J. Phys. Astrophys. Suppl.*, 47, 1
- Ikeda S., Awaki H., Terashima Y., 2009, *ApJ*, 692, 608
- Isobe N., Kubota A., Makishima M., Ghandi P., Griffiths R. E., Dewangan G. C., Itoh T., Mizuno T., 2008, *PASJ*, 60, 241
- Itoh T., et al., 2008, *PASJ*, 60S, 251
- Koyama K., et al., 2007, *PASJ*, 59, 23
- Lenain J.-P., Ricci C., T'ulser M., Dorner D., Walter R., 2011, *A&A*, 524, 72
- Lenc E., Tingay S. J., 2009, *AJ*, 137, 537
- Manzo G., Giarrusso S., Santangelo A., Ciralli F., Fazio G., Piraino S., Segreto A., 1997, *A&AS*, 122, 341
- Marinucci A., Risaliti G., Wang J., Nardini E., Elvis M., Fabbiano G., Bianchi S., Matt G., 2012, *MNRAS*, in press (arXiv:1202.1279)
- Mitsuda K. et al., 2007, *PASJ*, 59, 1
- Murphy K. D., Yaqoob T., 2009, *MNRAS*, 397, 1549 (MY09)
- Netzer H. 1990, in *Active Galactic Nuclei*, ed. R. D. Blandford, H. Netzer, L. Woltjer (Berlin: Springer), 137
- Parmar A. N., et al., 1997, *A&AS*, 122, 309
- Rivers E., Markowitz A., Rothschild R., 2011, *ApJS*, 193, 3
- Shurch N. J., Roberts T. P., Warwick R. S., 2002, *MNRAS*, 335, 241
- Shu X. W., Yaqoob T., Wang J. X., 2011, *ApJ*, 738, 147
- Serlemitsos P. J. et al., 2007, *PASJ*, 59, 9
- Takahashi T., et al., 2007, *PASJ*, 59, 35
- Titarchuk L., 1994, *ApJ*, 434, 570
- Tueller J., et al., 2010, *ApJS*, 186, 378

- Tueller J., Mushotzky R. F., Barthelmy S., Cannizzo J. K., Gehrels N., Markwardt C. B., Skinner G. K., & Winter L. M. 2008, ApJ, 681, 113
- Turner T. J., George I. M., Nandra K., Mushotzky R. F. 1997, ApJ, 488, 164
- Vasudevan R. V., Fabian A. C., Ghandi P., Winter L., M., Mushotzky R. F., 2010, MNRAS, 402, 181.
- Verner D. A., Ferland G. J., Korista K. T., Yakovlev D. G., 1996, ApJ, 465, 487
- Winter L. M., Mushotzky R. F., Reynolds C. S., Tueller, J. 2009, ApJ, 690, 1322
- Winter L. M., Mushotzky R. F., Tueller J., Markwardt C., 2008, ApJ, 674, 686
- Yaqoob T., et al., 2007, PASJ, 59, 283
- Yaqoob T., Murphy K. D., Miller L., Turner T. J., 2010, 401, 411
- Yaqoob T., Murphy K. D., 2011a, MNRAS, 412, 277
- Yaqoob T., Murphy K. D., 2011b, MNRAS, 412, 1765